

2008

Markov chain models of calcium puffs and sparks

Jeffrey R. Groff

College of William & Mary - Arts & Sciences

Follow this and additional works at: <https://scholarworks.wm.edu/etd>



Part of the [Biophysics Commons](#)

Recommended Citation

Groff, Jeffrey R., "Markov chain models of calcium puffs and sparks" (2008). *Dissertations, Theses, and Masters Projects*. Paper 1539623333.

<https://dx.doi.org/doi:10.21220/s2-yn0e-1d19>

This Dissertation is brought to you for free and open access by the Theses, Dissertations, & Master Projects at W&M ScholarWorks. It has been accepted for inclusion in Dissertations, Theses, and Masters Projects by an authorized administrator of W&M ScholarWorks. For more information, please contact scholarworks@wm.edu.

Markov Chain Models of Calcium Puffs and Sparks

Jeffrey R. Groff

Newport News, Virginia

**Master of Science, The College of William & Mary, 2004
Bachelor of Arts, McDaniel College, 2001**

**A Dissertation presented to the Graduate Faculty
of the College of William and Mary in Candidacy for the Degree of
Doctor of Philosophy**

Department of Applied Science

**The College of William and Mary
January, 2008**

APPROVAL PAGE

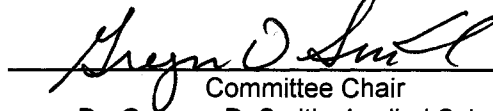
This Dissertation is submitted in partial fulfillment of
the requirements for the degree of

Doctor of Philosophy



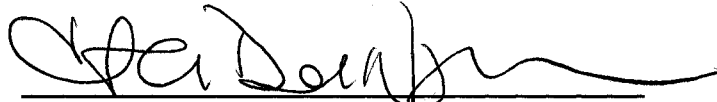
Jeffrey R. Groff

Approved by the Committee, December, 2007

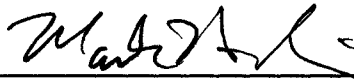


Committee Chair


Dr. Gregory D. Smith, Applied Science
The College of William & Mary



Dr. Christopher A. Del Negro, Applied Science
The College of William & Mary



Dr. Mark K. Hinders, Applied Science
The College of William & Mary



Dr. Eric A. Sobie, Pharmacology and Systems Therapeutics
Mount Sinai School of Medicine

ABSTRACT PAGE

Localized cytosolic Ca^{2+} elevations known as puffs and sparks are important regulators of cellular function that arise due to the cooperative activity of Ca^{2+} -regulated inositol 1,4,5-trisphosphate receptors (IP_3Rs) or ryanodine receptors (RyRs) co-localized at Ca^{2+} release sites on the surface of the endoplasmic reticulum or sarcoplasmic reticulum. Theoretical studies have demonstrated that the cooperative gating of a cluster of Ca^{2+} -regulated Ca^{2+} channels modeled as a continuous-time discrete-state Markov chain may result in dynamics reminiscent of Ca^{2+} puffs and sparks. In such simulations, individual Ca^{2+} -release channels are coupled via a mathematical representation of the local $[\text{Ca}^{2+}]$ and exhibit "stochastic Ca^{2+} excitability" where channels open and close in a concerted fashion. This dissertation uses Markov chain models of Ca^{2+} release sites to advance our understanding of the biophysics connecting the microscopic parameters of IP_3R and RyR gating to the collective phenomenon of puffs and sparks.

The dynamics of puffs and sparks exhibited by release site models that include both Ca^{2+} coupling and nearest-neighbor allosteric coupling are studied. Allosteric interactions are included in a manner that promotes the synchronous gating of channels by stabilizing neighboring closed-closed and/or open-open channel pairs. When the strength of Ca^{2+} -mediated channel coupling is systematically varied, simulations that include allosteric interactions often exhibit more robust Ca^{2+} puffs and sparks. Interestingly, the changes in puff/spark duration, inter-event interval, and frequency observed upon the random removal of allosteric couplings that stabilize closed-closed channel pairs are qualitatively different than the changes observed when open-open channel pairs, or both open-open and closed-closed channel pairs are stabilized. The validity of a computationally efficient mean-field reduction applicable to the dynamics of a cluster of Ca^{2+} -release Ca^{2+} channels coupled via the local $[\text{Ca}^{2+}]$ and allosteric interactions is also investigated.

Markov chain models of Ca^{2+} release sites composed of channels that are both activated and inactivated by Ca^{2+} are used to clarify the role of Ca^{2+} inactivation in the generation and termination of puffs and sparks. It is found that when the average fraction of inactivated channels is significant, puffs and sparks are often less sensitive to variations in the number of channels at release sites and the strength of Ca^{2+} coupling. While excessively fast Ca^{2+} inactivation can preclude puffs and sparks, moderately fast Ca^{2+} inactivation often leads to time-irreversible puff/sparks whose termination is facilitated by the recruitment of inactivated channels throughout the duration of the puff/spark event. On the other hand, Ca^{2+} inactivation may be an important negative feedback mechanism even when its time constant is much greater than the duration of puffs and sparks. In fact, slow Ca^{2+} inactivation can lead to release sites with a substantial fraction of inactivated channels that exhibit nearly time-reversible puffs and sparks that terminate without additional recruitment of inactivated channels.

Markov Chain Models of Calcium Puffs and Sparks

Jeffrey R. Groff

Contents

1	Introduction	1
1.1	Calcium homeostasis	2
1.2	Calcium channels	4
1.3	Calcium release channels	5
1.4	Blips, quarks, puffs, sparks, and waves	7
1.5	Mathematical modeling of intracellular calcium signaling	10
1.5.1	Models of the buffered diffusion of intracellular calcium	10
1.5.2	Markov chain models of calcium channel gating	12
1.6	Markov chain models of calcium puffs and sparks	16
2	Ryanodine Receptor Allosteric Coupling and the Dynamics of Calcium Sparks	18
2.1	Summary	18
2.2	Introduction	19
2.3	Model Formulation	23
2.3.1	Collective gating of RyR clusters	25
2.3.2	Release site ultrastructure and the calcium microdomain	26
2.3.3	Allosteric interactions between physically coupled channels	30
2.4	Results	32
2.4.1	Calcium and allosteric coupling at a three RyR cluster	32
2.4.2	Effects of calcium and allosteric coupling strength on spontaneous sparks	36
2.4.3	The effect of washing out allosteric interactions on spark statistics	42
2.4.4	A mean-field RyR cluster model	46
2.4.5	Representative mean-field simulations	50
2.4.6	Comparison of mean-field approximation and full model	53
2.4.7	Effect of allosteric coupling on calcium spark statistics	55
2.5	Discussion	58
2.5.1	Allosteric coupling and calcium spark formation and collapse	58

2.5.2	Allosteric coupling washout, cardiac dysfunction, and calcium spark statistics	59
2.5.3	The mean-field approximation of allosteric interactions	60
2.5.4	Generalizing the mean-field approximation	62
2.6	Conclusions	63
3	Calcium-Dependent Inactivation and the Dynamics of Calcium Puffs and Sparks	64
3.1	Summary	64
3.2	Introduction	65
3.3	Model formulation	69
3.3.1	A three-state channel model with calcium activation and calcium inactivation	69
3.3.2	Instantaneously coupled three-state channels	72
3.4	Results	75
3.4.1	Calcium release site models with low affinity calcium inactivation exhibit stochastic calcium excitability	75
3.4.2	High affinity calcium inactivation facilitates puff termination	78
3.4.3	Thermodynamically irreversible and nearly reversible puff and spark dynamics	80
3.4.4	Calcium inactivation and the sensitivity of puffs and sparks to variations in the strength of calcium coupling	82
3.4.5	Calcium inactivation and the sensitivity of puffs and sparks to the number of channels at release sites	85
3.4.6	Calcium inactivation and puff/spark duration	89
3.5	Discussion	93
3.5.1	Calcium inactivation and the sensitivity of puff/sparks to variations in the calcium coupling strength and the number of channels at the release	94
3.5.2	The rate of calcium inactivation and puff/spark termination	95
3.5.3	Calcium inactivation and puff/spark duration distributions	98
3.5.4	Limitations of the model	99
3.5.5	Entropy production rate in calcium release site models	100
3.6	Conclusions	102
4	Numerical methods for calcium release site modeling	103
4.1	Summary	103
4.2	Exact numerical simulation	104
4.3	Calculating the stationary probability distribution	106
4.4	Direct calculation of puff/spark statistics	108
4.4.1	Puff/spark duration	108
4.4.2	Inter-puff/spark interval	110

4.5	State space contraction using release site symmetries	112
4.6	A stochastic automata network descriptor for calcium release site models that include allosteric interactions	116
4.7	Example MATLAB [®] subroutines	119
4.7.1	Subroutine to numerically simulate Markov chain models of calcium release sites	119
4.7.2	Subroutine to calculate the stationary distribution of an infinitesimal generator matrix	121
4.7.3	Subroutine to directly calculate puff/spark statistics	122
4.7.4	Subroutine to map release site configurations to symmetry groups	125
4.8	Conclusion	128
5	Epilogue	129
5.1	Summary of results	129
5.2	Direction of future work	131
5.2.1	Markov chain models of calcium channel gating	131
5.2.2	Calcium release via the polycystic 2 ion channel	133
5.3	Local calcium release and studies of global calcium signals	133
	Afterword	136
	Bibliography	139
	Vita	161

Acknowledgments

I would like to acknowledge all of the individuals who have facilitated my endeavors at The College of William & Mary and whose encouragement and advice have been instrumental in the work of this manuscript. I sincerely thank my advisor Gregory D. Smith who I am sure will continue to be a valuable mentor for years to come. I thank the members of my laboratory cohort, Blair Williams and Hilary DeRemigio, as well as the post doctoral fellows Marco A. Huertas and Drew LaMar for their many technical and scientific contributions to my work. I thank Christopher A. Del Negro for the inspirational opportunity he gave me to work in his laboratory. I also wish to acknowledge Barbara Monteith for providing helpful editorial feedback on this and other manuscripts. Last, but certainly not least, I thank my best friend and wife, Amanda, for her unwavering support.

The work upon which this manuscript is based was funded by the National Science Foundation under Grants No. 0133132 and 0443843. I utilized computational facilities at the College of William & Mary funded by grants from the NSF and Sun Microsystems.

Chapter 1

Introduction

Although widely recognized as an important component of skeletal structure, calcium, as a divalent cation (Ca^{2+}), is also an ubiquitous element of intracellular signaling, performing a diverse assortment of functional and regulatory roles in eukaryotic cells. For example, Ca^{2+} waves initiate the enzymatic machinery of gene expression at fertilization, and Ca^{2+} signals participate in the biochemical cascades that result in programmed cell death (apoptosis) [Berridge et al., 1998]. Calcium is also necessary for neural communication and muscle contraction. Synaptotagmin, a protein implicated in the exocytosis of vesicles containing neurotransmitters into synaptic clefts, is activated by Ca^{2+} [Fernández-Chacón et al., 2001]. Muscle contraction is initiated when Ca^{2+} binds to troponin C, a protein associated with myofilaments [Bers, 2002]. In addition to these regulatory roles, Ca^{2+} also conveys electrical charge across the membranes of excitable cells. For instance, thalamic neurons that express the low-voltage activated T-type Ca^{2+} channel may exhibit slow Ca^{2+} depolarizations during certain states of arousal. Fast Na^+ and K^+ action potentials occur on the crests of these depolarizations resulting in bursts of action potentials that are integral to thalamocortical oscillations and sleep rhythms and are implicated in some epileptic

states [McCormick and Bal, 1997].

The temporal and spatial scales of cytoplasmic Ca^{2+} signals vary over several orders of magnitude and cells often employ many overlapping Ca^{2+} signals to regulate cellular function [Marchant and Parker, 2000]. For example, in the medullary neurons responsible for generating breathing rhythms in mammals, Ca^{2+} activates non-specific cation currents that are necessary for inspiration. It also acts on a slower time scale as a second messenger, binding to intracellular receptors and regulating the frequency and amplitude of inspiratory drive [Pace et al., 2007, Del Negro et al., 2005, Crowder et al., 2007]. Variations of the temporal and spatial extent of Ca^{2+} signals in dendritic spines shape neuronal excitability by modulating Ca^{2+} -activated K^+ currents and contributing to both long-term potentiation and depression of synapses [Marchant and Parker, 2000, Bootman et al., 2001b, Berridge, 1998, Yuste et al., 2000]. In cardiac myocytes (muscle cells), long-lived Ca^{2+} signals overlap the transient $[\text{Ca}^{2+}]$ increases necessary to initiate contraction, activating phosphatases and genes that tightly regulate cardiac output. Even minute variations in these Ca^{2+} signals may result in fatal cardiac arrhythmias or cardiac hypertrophy [Bers and Guo, 2005].

1.1 Calcium homeostasis

In order to finely tune the temporal and spatial extent of intracellular Ca^{2+} signals, an elaborate ‘toolbox’ of cellular signaling components (receptors, channels, buffers, pumps, and exchangers) have evolved (for a review see [Berridge et al., 2003, Berridge, 2006, Bers, 2002]). Because prolonged elevated Ca^{2+} concentrations are toxic, many of these components are essential for maintaining the resting cytosolic $[\text{Ca}^{2+}]$ near 100 nM, much lower than the 1-2 mM $[\text{Ca}^{2+}]$ outside the cell and the 100 μM $[\text{Ca}^{2+}]$ within intracellular Ca^{2+} reservoirs, namely the endoplasmic reticulum (ER) and sar-

coplasmic reticulum (SR) [Hille, 2001]. Plasma membrane Ca^{2+} -ATPase (PMCA) pumps utilize the stored metabolic energy of adenosine triphosphate (ATP) to extrude Ca^{2+} from cells against the $[\text{Ca}^{2+}]$ gradient. A similar class of pumps called sarcoplasmic endoplasmic reticulum Ca^{2+} -ATPase (SERCA) pumps transport Ca^{2+} into the ER and SR, ensuring that these intracellular stores are replete.

While the PMCA and SERCA pumps tend to have low transport rates, both have a high affinity for Ca^{2+} . Consequently, both are important for maintaining the homeostatic $[\text{Ca}^{2+}]$ near 100 nM following small perturbations from rest. On the other hand, some Ca^{2+} transport proteins have high transport rates and are most active following large increases in the cytosolic $[\text{Ca}^{2+}]$. One such protein, the plasma membrane $\text{Na}^+/\text{Ca}^{2+}$ exchanger (NCX), utilizes the $[\text{Na}^+]$ gradient across the plasma membrane to extrude one Ca^{2+} ion from the cytosol in exchange for three Na^+ ions. Another is the highly selective mitochondrial Ca^{2+} channel—formally thought to be a uniporter—that utilizes the electrical gradient existing between the mitochondrial matrix and the cytosol to rapidly sequester Ca^{2+} within the mitochondria following large Ca^{2+} perturbations [Kirichok et al., 2004, Saris and Carafoli, 2005]. Cells also have a wide variety of Ca^{2+} binding proteins and chelators that buffer intracellular Ca^{2+} such that at any moment, less than 1% of the Ca^{2+} in the cytosol is in a free ionic form. Some Ca^{2+} buffers, like calbindin, are mobile in that they freely diffuse in the cytosol. Others, such as calsequestrin, may occur in an immobile form as part of a membrane bound complex. Because different buffers may have distinct Ca^{2+} binding kinetics and affinities, they play a diverse role in shaping the spatial extent and temporal dynamics of Ca^{2+} signals [Hille, 2001].

1.2 Calcium channels

While maintaining the $[Ca^{2+}]$ gradients across the plasma and the ER/SR membranes requires cells to expend metabolic energy, Ca^{2+} entry from the extracellular space and release from the ER/SR channels is passive, mediated by Ca^{2+} channels. When Ca^{2+} channels are open, Ca^{2+} simply flows down its electro-chemical gradient into the cytosol.

While many Ca^{2+} channels share a significant degree of homology, they differ in the mechanisms by which they activate (for review see [Bootman et al., 2001a, Hille, 2001]). As their name suggests, voltage-operated Ca^{2+} channels (VOCCs) are activated by changes in the voltage across the plasma membrane. The L-type Ca^{2+} channel (dihydropyridine receptor) is an example of this class of channels and plays an essential role in coupling the electrical depolarization of the plasma membrane to physical contraction of myocytes. In addition to the T-type low-voltage activated Ca^{2+} channel previously discussed, neurons also express N-type and P-type Ca^{2+} channels. These VOCCs are often found in axon terminals and mediate the entry of Ca^{2+} necessary for neurotransmitter release following electrical depolarization of the axon.

A second class of Ca^{2+} channels are the receptor-operated Ca^{2+} channels (ROCCs), which are activated by the binding of ligands. One such channel, the NMDA receptor, is often expressed on postsynaptic dendrites and is activated by the neurotransmitter glutamate. While the NMDA receptor is permeable to other cations such as Na^+ and K^+ , Ca^{2+} ions that enter the cytosol via this channel are important for regulating long-term synaptic potentiation. Interestingly, NMDA receptors also exhibits a degree of voltage dependance [Hille, 2001]. Many ROCCs are activated by the binding of diffusible cytosolic second messengers. For example, store operated Ca^{2+} channels

(SOCC) are activated by the second messenger cyclic AMP, which is released into the cytosol when intracellular Ca^{2+} stores become depleted. When activated SOCCs ensure enough Ca^{2+} enters the cytosol from outside the cell to replenish the depleted intracellular stores. Several members of the transient receptor potential (TRP) channel family are thought to be SOCCs.

While most Ca^{2+} channels can be classified as either VOCCs or ROCCs, some plasma membrane Ca^{2+} channels are neither voltage nor ligand activated, but mechanically activated, responding to the physical deformation of the cell. Interestingly, Ca^{2+} itself can function as a ligand, binding to and activating some Ca^{2+} channels. In fact, the intracellular Ca^{2+} channels primarily responsible for the release of Ca^{2+} from the ER and SR are activated by Ca^{2+} . These channels are reviewed below.

1.3 Calcium release channels

Release of Ca^{2+} from intracellular stores (i.e., the ER and SR) is primarily mediated by two families of ROCCs, inositol 1,4,5-trisphosphate receptors (IP_3Rs) and ryanodine receptors (RyRs) (for review see [Fill and Copello, 2002, Bezprozvanny, 2005, Foskett et al., 2007]). Both IP_3Rs and RyRs are large oligomers with multiple membrane spanning domains, and each channel complex is composed of four IP_3R or RyR proteins. Although the RyR channel protein is slightly larger (560 kDa versus 310 kDa [Lai et al., 1989, Foskett et al., 2007]), the genetic structure of both proteins share a significant amount of homology. Importantly, both IP_3Rs and RyRs are usually associated with various accessory proteins *in vivo*. For example, all isoforms of RyRs associate with FK-binding proteins [Fill and Copello, 2002].

While both families of Ca^{2+} release channels are activated by Ca^{2+} , other agonists and antagonists modulate IP_3Rs and RyRs gating. RyRs are so named because

they bind the plant alkaloid ryanodine, which reduces their likelihood of being in the open state. IP₃R_s are so named because they require the co-agonist inositol 1,4,5-trisphosphate (IP₃) to open [Marchant and Taylor, 1998, Berridge, 1993b]. Inositol 1,4,5-trisphosphate is an intracellular second messenger formed when G-protein coupled membrane receptors activate phospholipase C (PLC), which in turn hydrolyzes membrane bound phosphatidylinositol 4,5-bisphosphate (PIP₂). Before the discovery of IP₃ in the early 1980's [Streb et al., 1983], the mechanism by which activation of surface receptor via ligands such as the serotonin precursor 5-HT coupled to intracellular Ca²⁺ release was a mystery. Since that time, it has become apparent that release of Ca²⁺ from intracellular stores via the IP₃ pathway is a ubiquitous component of intracellular signaling in a myriad of cell types, from insulin-secreting pancreatic β -cells [Biden et al., 1984] to photoreceptors [Payne et al., 1986] [Berridge, 2005].

Both the IP₃R and the RyR families contain three major channel isoforms denoted IP₃R1, IP₃R2, and IP₃R3 and RyR1, RyR2, and RyR3. All of these isoforms are expressed in vertebrates. The most widely studied IP₃R isoform (IP₃R1) is expressed in many cells of the central nervous system. Most cells outside the central nervous system express at least one IP₃R isoform, and many cells express multiple subtypes. The RyR1 isoform is predominantly found in skeletal muscle, although it is also expressed in cerebellar Purkinje neurons [Berridge, 1998]. The RyR2 subtype is expressed in cardiac muscle and is the predominant RyR isoform in the brain [Berridge, 1998]. The remaining RyR isoform (RyR3) is also expressed in the brain and in low levels in some striated muscle cells [Murayama and Ogawa, 1996].

Figure 1.1 is a schematic representation of a cell showing the various Ca²⁺ signaling channels, pumps, and exchangers discussed above (Sections 1.1 through 1.3). *Black arrows* indicate the direction of Ca²⁺ flux across the plasma and ER/SR membranes.

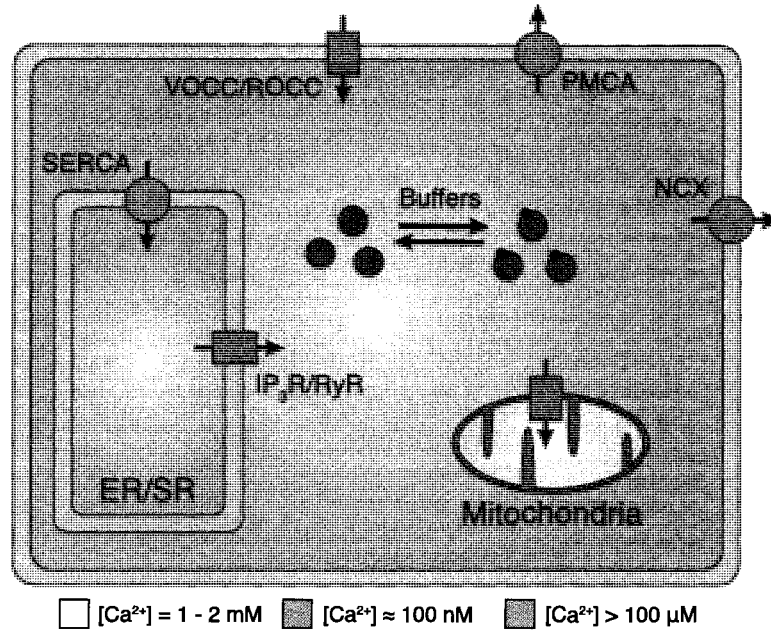


Figure 1.1: Schematic representation of intracellular Ca^{2+} signaling components. Calcium concentration gradients across the plasma membrane, the endoplasmic reticulum (ER), and the sarcoplasmic reticulum (SR) are maintained by plasma membrane Ca^{2+} ATPase (PMCA) and sarcoplasmic endoplasmic reticulum Ca^{2+} ATPase (SERCA) pumps, and other ion transport proteins such as the $\text{Na}^+/\text{Ca}^{2+}$ exchanger (NCX). Uptake of Ca^{2+} into the mitochondrial matrix is mediated by a highly selective Ca^{2+} channel previously thought to be a uniporter [Kirichok et al., 2004]. Free cytosolic Ca^{2+} is buffered by a host of Ca^{2+} binding proteins and chelators. Release of Ca^{2+} from the ER or SR is mediated by two families of ROCCs, inositol 1,4,5-trisphosphate receptors (IP_3Rs) and ryanodine receptors (RyRs). The *black arrows* through transport proteins and channels indicate the direction of Ca^{2+} movement.

1.4 Blips, quarks, puffs, sparks, and waves

Because both IP_3Rs and RyRs are activated by cytosolic Ca^{2+} , a small increase in $[\text{Ca}^{2+}]$ near these channels may promote the further release of intracellular Ca^{2+} , a phenomenon known as Ca^{2+} -induced Ca^{2+} release (CICR) [Bers, 2002]. The dynamics of Ca^{2+} release is complicated by the fact that both IP_3Rs and RyRs are often co-localized on the ER and SR membranes at Ca^{2+} release sites. For example, in the cortical regions (approximately $6 \mu\text{m}$ below the plasma membrane) of imma-

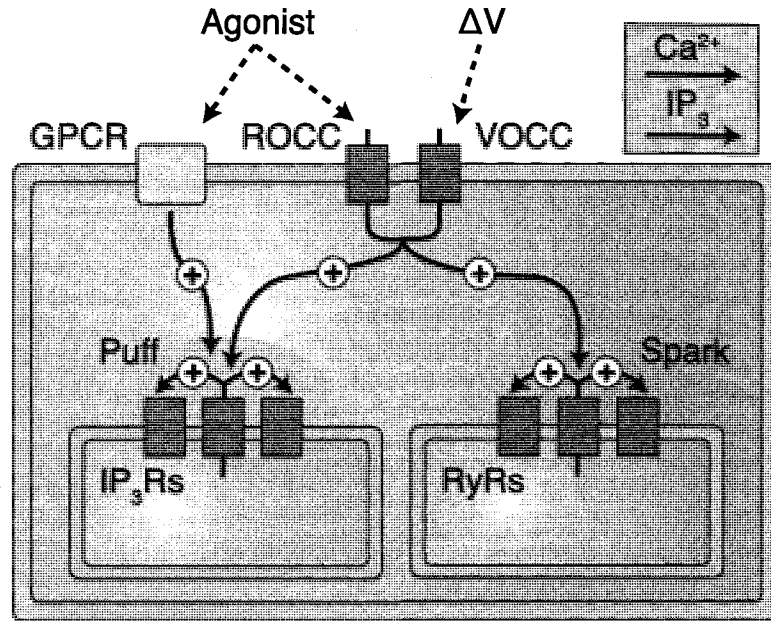


Figure 1.2: Schematic representation of Ca^{2+} -induced Ca^{2+} -release (CICR). Both inositol 1,4,5-trisphosphate receptors (IP_3Rs) and ryanodine receptors (RyRs) are activated by cytosolic Ca^{2+} *black arrows*. IP_3Rs are also activated by the co-agonist IP_3 hydrolyzed from membrane bound precursors via a G-protein coupled receptor (GPCR). Ca^{2+} entry into the cytosol is mediated by voltage operated Ca^{2+} channels (VOCCs) and receptor operated Ca^{2+} channels (ROCCs). A small increase in the $[\text{Ca}^{2+}]$ near clusters of IP_3Rs and RyRs may promote the further release of intracellular Ca^{2+} , resulting in Ca^{2+} puffs and sparks.

ture *Xenopus* oocytes, IP_3Rs occur in clusters of 5–50 with inter-cluster spacing on the order of a few microns [Sun et al., 1998]. IP_3Rs are also clustered on the surface of the outer nuclear membrane of *Xenopus* oocytes [Mak and Foskett, 1997]. Similarly, RyRs are assembled into paracrystalline arrays of up to 100 channels in myocytes [Franzini-Armstrong et al., 1999b, Bers, 2002].

The clustering of IP_3Rs and RyRs and the phenomenon of CICR results in three distinct modes of Ca^{2+} mobilization that have been observed via confocal microfluorimetry in oocytes, cardiomyocytes, and many other cell types: 1) localized Ca^{2+} elevations due to the activation of a single channel that are referred to as Ca^{2+} blips

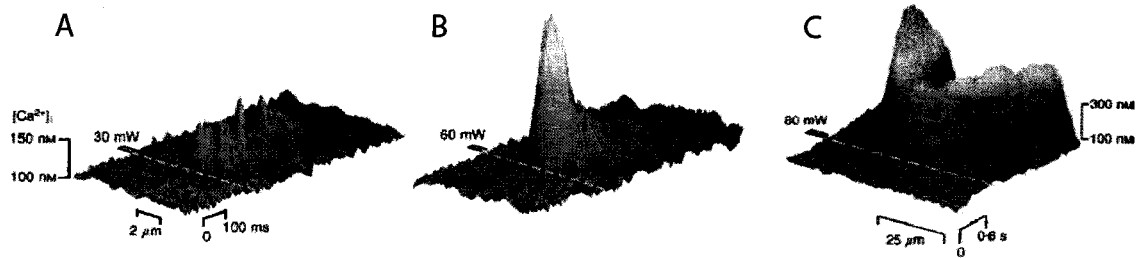


Figure 1.3: Fluo-3 imaging of intracellular Ca^{2+} release in Guinea-pig ventricular myocytes elicited by two-photon excitation photolysis of caged Ca^{2+} . Varying levels of excitation result in fundamental (A, Ca^{2+} quark), elementary (B, Ca^{2+} spark), and global (C, Ca^{2+} wave) modes of Ca^{2+} release. Adapted with permission from [Lipp and Niggli, 1998].

or quarks depending on whether the events are mediated by an IP_3R or RyR [Niggli, 1999, Niggli and Shirokova, 2007], 2) Ca^{2+} elevations due to the activation of multiple IP_3Rs or RyRs associated with a single Ca^{2+} release site known as Ca^{2+} puffs and sparks [Cheng et al., 1993, Cannell et al., 1995, Yao et al., 1995, Parker et al., 1996b, Parker et al., 1996a], and 3) global Ca^{2+} elevations such as oscillations and waves that involve multiple release sites [Cheng et al., 1996]. These three modes of Ca^{2+} release have been dubbed fundamental, elementary, and global responses, respectively [Berridge, 1997, Berridge, 2006].

Figure 1.2 is a schematic representation of CICR and puffs and sparks. *Black arrows* indicate how the influx of Ca^{2+} via plasma membrane Ca^{2+} channels or the release of Ca^{2+} via IP_3Rs and RyRs may promote the further release of Ca^{2+} via IP_3Rs and RyRs . Figure 1.3A shows an experimental image of a Ca^{2+} quark in a ventricular myocyte. For comparison, Fig. 1.3B and Fig. 1.3C show a Ca^{2+} spark and a Ca^{2+} wave, respectively.

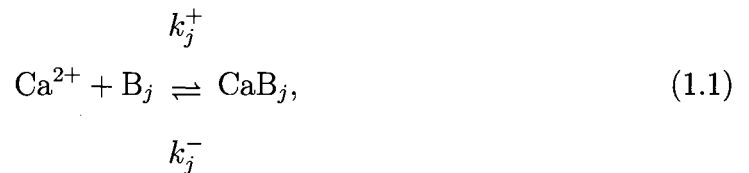
1.5 Mathematical modeling of intracellular calcium signaling

Because Ca^{2+} mobilization is a complex phenomenon, mathematical models have significantly contributed to the study of intracellular Ca^{2+} signaling. Importantly, theoretical models are constructed to reflect experimental observations of Ca^{2+} signaling and are often capable of providing mechanistic insights that are valuable to experimentalists. The following sections briefly review the theoretical studies of intracellular Ca^{2+} diffusion and single channel gating on which this dissertation is founded.

1.5.1 Models of the buffered diffusion of intracellular calcium

Much of our knowledge of intracellular Ca^{2+} concentration changes is derived from experiments that image Ca^{2+} transients using fluorescent indicator dyes such as Arsenazo III, fura-2, fluo-3, and fluorescing derivatives of the common exogenous Ca^{2+} buffers BAPTA and EGTA [Tsien, 1980, Connor and Ahmed, 1984, Williams et al., 1985, Neher and Almers, 1986b, Neher and Almers, 1986a, Neher and Augustine, 1992, Augustine et al., 1985]. On the other hand, theoretical models have advanced our understanding of the association of Ca^{2+} with buffers (including indicator dyes) and the transport of free and buffered Ca^{2+} in the cytosol.

The buffered diffusion of Ca^{2+} may be mathematically represented using a system of reaction-diffusion equations [Smith et al., 2001]. These equations assume bimolecular association reactions between Ca^{2+} and buffer of the form



where B_j and CaB_j are free and bound buffer, respectively, k_j^+ is a bimolecular association rate constant, k_j^- is a unimolecular dissociation constant, and the index j is over all buffer species. Assuming Fickian diffusion, the concentration of free Ca^{2+} , free buffer ($[B_j]$), and bound buffer ($[CaB_j]$) are given by [Wagner and Keizer, 1994, Smith et al., 2001]

$$\frac{\partial[Ca^{2+}]}{\partial t} = D_{Ca} \nabla^2 [Ca^{2+}] + \sum_j R_j, \quad (1.2)$$

$$\frac{\partial[B_j]}{\partial t} = D_{B_j} \nabla^2 [B_j] + R_j, \quad (1.3)$$

and

$$\frac{\partial[CaB_j]}{\partial t} = D_{CaB_j} \nabla^2 [CaB_j] - R_j, \quad (1.4)$$

with reaction terms given by

$$R_j = -k_j^+ [B_j] [Ca^{2+}] + k_j^- [CaB_j]. \quad (1.5)$$

In these equations, D_{Ca} , D_{B_j} , and D_{CaB_j} are diffusion coefficient for free Ca^{2+} , free buffer, and bound buffer, respectively. Using appropriate boundary conditions and assuming a fixed background $[Ca^{2+}]$ (see [Smith et al., 2001]), these equations may be used to model diffusion of Ca^{2+} near a point source (i.e., an open intracellular Ca^{2+} channel).

Theoretical studies using reaction diffusion equations similar to those above have revealed that mobile indicators such as fura-2 may significantly affect the dynamics of Ca^{2+} diffusion [Sala and Hernández-Cruz, 1990]. Further studies by a host of theorists have demonstrated that the kinetics and affinity of Ca^{2+} binding to buffers may significantly affect the concentration of free Ca^{2+} near open Ca^{2+} channels. For

example, Allbritton et al. demonstrated that endogenous buffers reduce the effective range of free Ca^{2+} in the cytosol to approximately $5 \mu\text{m}$ [Allbritton et al., 1992], and Stern showed that the slow binding kinetics of EGTA often make it an ineffective buffer of free Ca^{2+} within a few nanometers of channel pores [Stern, 1992a]. Many of these studies have resulted in approximations to the reaction diffusion equations for the buffered diffusion of Ca^{2+} , applicable in situations when buffer kinetics are rapid, the buffer concentration is high, or when Ca^{2+} buffering near an open Ca^{2+} channel is near steady-state [Neher, 1986, Wagner and Keizer, 1994, Stern, 1992a, Smith, 1996, Naraghi and Neher, 1997, Neher, 1998, Smith et al., 2001].

1.5.2 Markov chain models of calcium channel gating

Most of our understanding of the kinetics of single IP_3R and RyR gating is derived from experiments using the patch clamp technique and recordings of channels reconstituted into planar lipid bilayers [Watras et al., 1991, Bezprozvanny and Ehrlich, 1994, Bezprozvanny et al., 1991, Foskett et al., 2007, Mak and Foskett, 1997, Hagar et al., 1998, Mejía-Alvarez et al., 1999, Xiao et al., 1997]. For example, Fig. 1.4A shows planar lipid bilayer recordings of type I IP_3Rs [Bezprozvanny and Ehrlich, 1994] for several different $[\text{Ca}^{2+}]$ on the *trans* (i.e., luminal) side of the bilayer. While most of the time channels are closed (no current flowing), occasionally channels stochastically open as indicated by 2 pA current deviations. Transitions between the closed and open state are stochastic in time and Fig. 1.4B indicates that the dwell times in these two states are exponentially distributed. Averages over many recordings or, assuming ergodicity, time averages of individual recordings, are often used to determine the steady-state open probability of channels at various Ca^{2+} concentrations. For instance, Fig. 1.5A and B demonstrate that the steady-state open probability of

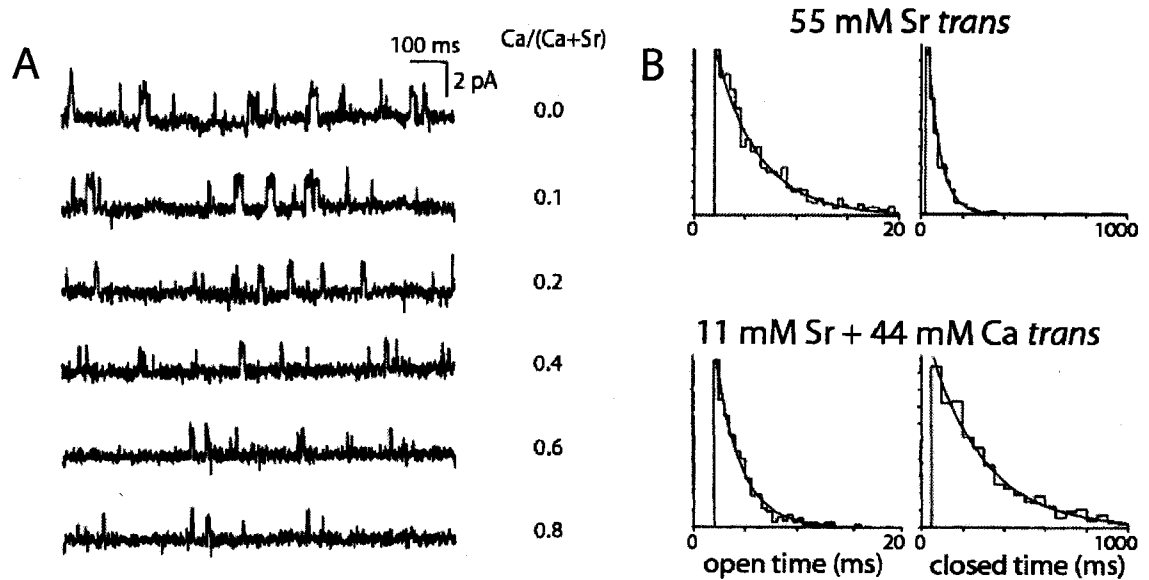


Figure 1.4: (A) Planar lipid bilayer recordings of reconstituted type I IP₃R_s using different mole fractions of Ca²⁺ on the *trans* (luminal) side of channels demonstrate gating between two conductance levels, 0 pA (closed) and 2 pA (open). The [Ca²⁺] and [IP₃] of the *cis* bath is 0.2 μM and 2 μM, respectively. (B) The open and closed dwell times are exponentially distributed and are a function of the *trans* [Ca²⁺]. Adapted with permission from [Bezprozvanny and Ehrlich, 1994].

IP₃R_s and RyR_s as a function of [Ca²⁺] may be bell-shaped, indicating the presence of Ca²⁺-dependent inactivation at elevated Ca²⁺ concentrations in addition to Ca²⁺ activation at lower Ca²⁺ concentrations.

Historically, the stochastic dynamics of IP₃R and RyR gating have been successfully modeled using continuous-time discrete state Markov chains [Norris, 1997, Stewart, 1994]. Such models are described by state-transition diagrams that enumerate all of the possible states a channel may occupy and indicate allowed transitions between these states. An example state-transition diagram corresponding to an IP₃R or RyR

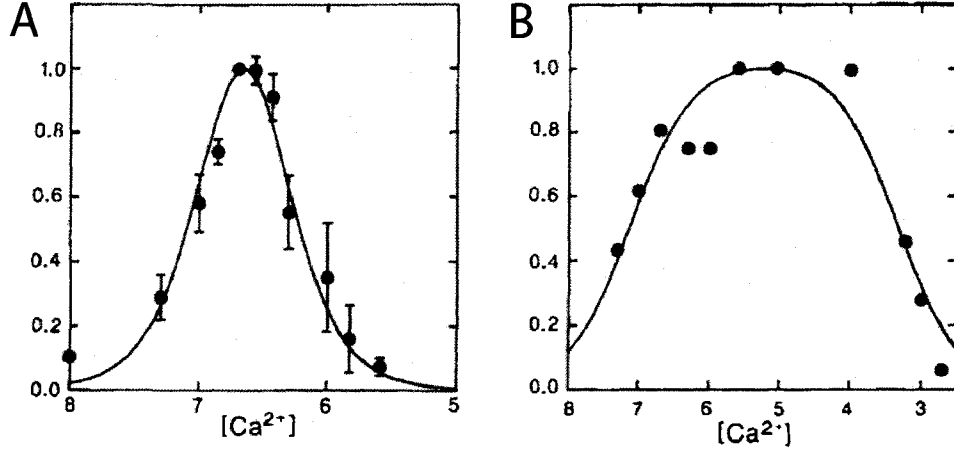
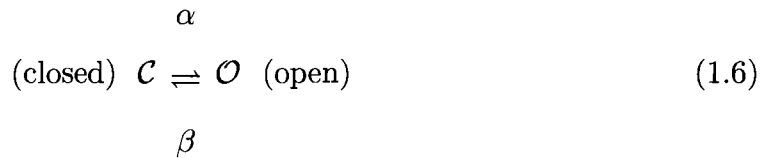


Figure 1.5: (A) *Filled circles* show the experimentally determined steady-state open probability of type I IP₃Rs (\pm SEM, $n = 4$) as a function of $-\log([Ca^{2+}])$. Data is fit assuming Michaelis-Menton-type binding to an activation and an inactivation site and a Hill coefficient (cooperativity) of 1.8. (B) Steady-state open probability of RyRs as a function of $-\log([Ca^{2+}])$. Adapted with permission from [Bezprozvanny et al., 1991].

with two states and two conductance levels (open and closed) is



where α and β are transition rates with units of time^{-1} . Equation 1.6 defines a discrete-state stochastic process, $S(t)$, with state space $S \in \{\mathcal{C}, \mathcal{O}\}$, and the dwell times in the open and closed states are exponentially distributed with expectations β^{-1} and α^{-1} , respectively. Importantly, Markov chain models of channel gating must satisfy the so-called ‘Markovian Property’ requiring that the conditional probability distribution of future states (given the current and previous states) depends only on the present state and not on past states [Norris, 1997]. In other words, the future depends on the present but not on the past. Markov chain models also assume that

channel proteins change conformations instantaneously and thus, do not explicitly model the dynamics of conformational changes.

The $\mathcal{C} \rightarrow \mathcal{O}$ transition rate of Eq. 1.6 (α) may depend on the cytosolic $[\text{Ca}^{2+}]$ representing the experimentally observed phenomenon of Ca^{2+} activation. Often, Markov chain models of IP_3R and RyR gating include additional transitions representing other experimentally observed phenomena. For example, the single channel model of Chap. 3 and many other models of IP_3R and RyR gating include Ca^{2+} -dependent transitions out of the open state, representing Ca^{2+} inactivation [Schiefer et al., 1995, Stern et al., 1997, Stern et al., 1999, Sneyd et al., 2004]. Keizer’s model of RyR gating includes a transition representing the phenomenon of Ca^{2+} -independent or ‘fateful’ inactivation [Keizer and Levine, 1996]. The De Young-Keizer model applicable to the gating of an IP_3R subunit has transitions that are dependent on the cytosolic $[\text{IP}_3]$, and the Fraiman and Dawson IP_3R model includes a representation of luminal Ca^{2+} regulation [De Young and Keizer, 1992, Fraiman and Dawson, 2004]. The parameters of IP_3R and RyR models (e.g., the association and dissociation rate constants for the binding of Ca^{2+} and other ligands) are often selected to agree with the dynamics and steady-state statistics of nuclear patch recordings and planer lipid bilayer recordings such as those shown in Fig. 1.4 and Fig. 1.5 [Bezprozvanny and Ehrlich, 1994, Sitsapesan and Williams, 1994]. For example, the association and dissociation rate constants of the two-state Ca^{2+} -activated RyR channel model used in Chap. 2 are selected so that the dissociation constant of Ca^{2+} binding is $5 \mu\text{M}$, consistent with experimental measurements [Györke and Györke, 1998].

1.6 Markov chain models of calcium puffs and sparks

A cluster of IP₃R_s or RyR_s may also be modeled as a continuous-time discrete-state Markov chain [Hinch, 2004, Mazzag et al., 2005, DeRemigio and Smith, 2005, Nguyen et al., 2005, Huertas and Smith, 2007, Rengifo et al., 2002, Ríos and Stern, 1997, Shuai and Jung, 2002a, Shuai and Jung, 2002b, Stern et al., 1999, Swillens et al., 1998, Swillens et al., 1999]. In such models, individual Ca²⁺-release channels are coupled via a mathematical representation of the local Ca²⁺ landscape, the so-called Ca²⁺ microdomain. The microdomain is often formulated using approximate solutions to the reaction-diffusion equations describing the buffered diffusion of Ca²⁺ discussed in Section 1.5.1. Importantly, these Ca²⁺ release site models may exhibit the phenomenon of “stochastic Ca²⁺ excitability” reminiscent of Ca²⁺ puffs and sparks where channels open and close in a concerted fashion. This dissertation uses Markov chain models of Ca²⁺ release sites to advance our understanding of how the dynamics of Ca²⁺ puffs and sparks depend on the microscopic parameters of IP₃R and RyR gating as well as release-site characteristics such as the number, density, and source amplitude of channels.

The remainder of this dissertation is arranged as follows. Chapter 2 focuses on the collective gating of RyR_s that experience nearest neighbor physical coupling via allosteric interactions in addition to diffuse Ca²⁺ coupling. We investigate how the dynamics of simulated sparks depend simultaneously on the strength of Ca²⁺ coupling and the strength of allosteric interactions that promote the synchronous gating of channels. In Chap. 3 we model Ca²⁺ release sites composed of channels that, in addition to Ca²⁺ activation, exhibit Ca²⁺ inactivation so that the single-channel steady-state open probability as a function of [Ca²⁺] is bell-shaped as in Fig. 1.5.

We study how puffs and sparks depend on the affinity and rate of Ca^{2+} inactivation. Chapter 4 presents numerical methods for simulating and analyzing Markov chain models of puffs and sparks. Several of these methods were necessary for the studies of Chaps. 2 and 3. Chapter 5 summarizes the significant contributions of this dissertation and discusses possible future theoretical studies of Ca^{2+} puffs and sparks.

Chapter 2

Ryanodine Receptor Allosteric Coupling and the Dynamics of Calcium Sparks

2.1 Summary

Puffs and sparks are localized intracellular Ca^{2+} elevations that arise from the cooperative activity of Ca^{2+} -regulated inositol 1,4,5-trisphosphate receptors and ryanodine receptors clustered at Ca^{2+} release sites on the surface of the endoplasmic reticulum or the sarcoplasmic reticulum. While the synchronous gating of Ca^{2+} -regulated Ca^{2+} channels can be mediated entirely through the buffered diffusion of intracellular Ca^{2+} , inter-protein allosteric interactions also contribute to the dynamics of RyR gating and Ca^{2+} sparks. In this chapter, Markov chain models of Ca^{2+} release sites are used to investigate how the statistics of Ca^{2+} spark formation and collapse are related to the coupling of RyRs via local $[\text{Ca}^{2+}]$ changes and allosteric interactions. Allosteric interactions are included in a manner that promotes the synchronous gating

of channels by stabilizing neighboring closed-closed and/or open-open channel pairs. When the strength of Ca^{2+} -mediated channel coupling is systematically varied (e.g., by changing the Ca^{2+} buffer concentration), simulations that include synchronizing allosteric interactions often exhibit more robust Ca^{2+} sparks; however, for some Ca^{2+} coupling strengths the sparks are less robust. We find no evidence that the distribution of spark durations can be used to distinguish between allosteric interactions that stabilize closed channel pairs, open channel pairs, or both in a balanced fashion. On the other hand, we do observe qualitatively different changes in spark statistics (duration, inter-spark interval, and frequency) when allosteric couplings of these three different types are randomly removed, suggesting an experimental methodology for determining the type of synchronizing allosteric interactions exhibited by coupled RyRs. We also investigate the validity of a mean-field reduction applicable to the dynamics of a ryanodine receptor cluster coupled via local $[\text{Ca}^{2+}]$ and allosteric interactions. In addition to facilitating parameter studies of the effect of allosteric coupling on spark statistics, the derivation of the mean-field model establishes the correct functional form for cooperativity factors representing the coupled gating of RyRs. This mean-field formulation is well-suited for use in computationally efficient whole cell simulations of excitation-contraction coupling.

2.2 Introduction

Localized intracellular Ca^{2+} elevations, known as puffs and sparks, are cellular signals of great interest that arise from the cooperative activity of clusters of Ca^{2+} -regulated inositol 1,4,5-trisphosphate receptors (IP_3Rs) and ryanodine receptors (RyRs). Not only are puffs, sparks, and other localized Ca^{2+} elevations highly specific regulators of cellular function, they also contribute to global Ca^{2+} release events in eukaryotic cells

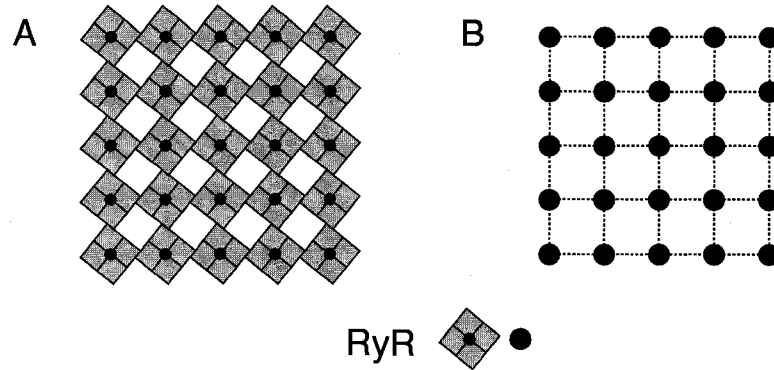


Figure 2.1: (A) Schematic representation of a Ca^{2+} release site following [Yin et al., 2005a]. Each ryanodine receptor Ca^{2+} release channel (RyR) is composed of four identical subunits (*gray squares*) surrounding a central pore (*black circle*). Subunits physically contact neighboring subunits and homotetrameric channels form a right-handed checkerboard-like lattice. (B) In the Ca^{2+} release site model two-state Ca^{2+} -activated RyRs (*black circles*) are globally coupled via the buffered diffusion of intracellular Ca^{2+} (not shown) and locally coupled to 2–4 nearest neighbors via allosteric interactions (*dotted lines*). Consistent with experimentally measured RyR lattice dimensions, the pore-to-pore inter-channel distance is 30 nm.

[Berridge, 1993b, Berridge, 1997, Berridge, 2006, Bers, 2002, Cheng et al., 1996, Cheng et al., 1993]. For example, the process of excitation-contraction (EC) coupling in cardiac myocytes is initiated when electrical depolarization of the sarcolemma allows a small amount of Ca^{2+} to enter the cell via voltage-gated L-type Ca^{2+} channels (dihydropyridine receptors). This trigger Ca^{2+} activates a much larger release of Ca^{2+} from the sarcoplasmic reticulum (SR) via Ca^{2+} -activated RyRs clustered at a Ca^{2+} release site, a process known as Ca^{2+} -induced Ca^{2+} -release (CICR), resulting in a Ca^{2+} spark. Although the increase in $[\text{Ca}^{2+}]$ due to individual sparks is localized to Ca^{2+} release sites, the cell-wide summation of many sparks provides the increase in the cytosolic $[\text{Ca}^{2+}]$ that initiates the mechanical contraction of the myocyte.

Experimental evidence suggests that the dynamics of RyR gating, Ca^{2+} sparks, and EC coupling are affected by inter-protein allosteric interactions between neigh-

boring RyRs at Ca^{2+} release sites. Each RyR channel is an oligomer composed of four identical 565 kDa RyR proteins surrounding a central pore, and groups of 10–100 RyR homotetramers form regular two-dimensional checkerboard-like lattices on the surface of the SR membrane [Franzini-Armstrong et al., 1999b, Franzini-Armstrong et al., 1999a, Yin et al., 2005a, Yin et al., 2005b, Serysheva, 2005, Lai et al., 1989, Bers, 2002] (see Fig. 2.1A). When channels are reconstituted to mimic this *in situ* crystalline lattice, RyRs maintain physical contact with neighboring channels [Yin et al., 2005a]. Moreover, Marx and co-workers observed that physically coupled RyRs incorporated into planar lipid bilayers exhibit “coupled” gating even when Ca^{2+} is not the charge carrier [Marx et al., 1998, Marx et al., 2001]. While such Ca^{2+} independent coupling has not been uniformly observed in other labs [Stern and Cheng, 2004, Fill and Copello, 2002], the functional coupling observed by Marx requires the association of FK-binding proteins (FKBPs) that conjugate with the RyR homotetramer in approximately stoichiometric proportions [Fill and Copello, 2002, Wang et al., 2003, Timerman et al., 1993].

The biophysical theory connecting single-channel kinetics of IP_3Rs and RyRs to the collective phenomena of Ca^{2+} puffs and sparks and global phenomena such as EC coupling is not as well-developed as our understanding of the association of Ca^{2+} with endogenous and exogenous buffers (e.g., Ca^{2+} -binding proteins, chelators, and indicators) [Neher and Almers, 1986b, Sala and Hernández-Cruz, 1990, Allbritton et al., 1992, Wagner and Keizer, 1994, Smith, 1996, Gabso et al., 1997, Naraghi and Neher, 1997, Neher, 1998, Smith et al., 2001]. However, several theoretical studies have demonstrated that dynamics reminiscent of Ca^{2+} puffs and sparks may arise due to the cooperative activity of a cluster of Ca^{2+} -regulated Ca^{2+} -release channels modeled as a continuous-time discrete-state Markov chain [Hinch, 2004, Mazzag et al., 2005, DeRemigio and Smith, 2005, Nguyen et al., 2005, Huertas and Smith,

2007, Rengifo et al., 2002, Ríos and Stern, 1997, Shuai and Jung, 2002a, Shuai and Jung, 2002b, Stern et al., 1999, Swillens et al., 1998, Swillens et al., 1999]. In such simulations, individual Ca^{2+} -release channels are coupled via a time-dependent or time-independent representation of the local $[\text{Ca}^{2+}]$, the so-called Ca^{2+} -microdomain, and exhibit “stochastic Ca^{2+} excitability” where channels open and close in a concerted fashion. The phenomena of Ca^{2+} activation and inactivation, the dynamics of the buffered diffusion of intracellular Ca^{2+} , and the release site density and geometry, all significantly contribute to the statistics of simulated puffs and sparks [Swillens et al., 1999, Nguyen et al., 2005, DeRemigio et al., 2007].

Several theoretical studies to date have investigated the effects of inter-protein allosteric coupling on the dynamics of Ca^{2+} sparks. Stern and co-workers demonstrated that models of single channel gating derived from planar lipid bilayer experiments fail to produce stable EC coupling in release site models [Stern et al., 1999]. However, when release site models include nearest-neighbor allosteric interactions in addition to Ca^{2+} coupling, Ca^{2+} sparks can be recovered [Stern et al., 1999]. Allosteric couplings in Stern et al. [1999] are defined as free energies of interactions between neighboring channels and have the effect of modifying the affinity of release site transitions.

Using a formulation for allosteric coupling that is minimal compared to Stern’s, Sobie and co-workers studied the effects of allosteric interactions on spark statistics such as duration and frequency [Sobie et al., 2002]. This “sticky-cluster” model of CICR includes so-called ‘coupling factors’ that scale the transition rates of the single channel model allowing the gating of each channel to be influenced by the number of open and closed RyRs at the release site. Although these coupling factors are post-hoc additions to the single channel RyR model, and there is no account of release site geometry or nearest-neighbor interactions, the sticky-cluster model demonstrated that allosteric coupling may contribute to spark termination.

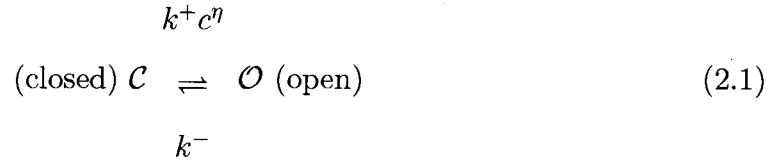
In order to clarify how the microscopic parameters of allosteric interactions and Ca^{2+} coupling simultaneously contribute to the formation and collapse of spontaneous Ca^{2+} sparks, we construct and analyze release site models composed of 16–49 two-state Ca^{2+} -activated RyRs organized on a Cartesian lattice and instantaneously coupled using linearized equations for the buffered diffusion of microdomain Ca^{2+} [Naraghi and Neher, 1997]. Using the methodology introduced by Stern and co-workers [Stern et al., 1999], RyRs also experience nearest-neighbor allosteric interactions that promote synchronous gating of channels (see Fig. 2.1B). Importantly, these synchronizing allosteric interactions may be incorporated to stabilize closed channel pairs, open channel pairs, or both in a balanced fashion. We probe how these different types of synchronizing allosteric interactions affect the presence or absence of Ca^{2+} excitability and the statistics of spontaneous Ca^{2+} sparks. In addition, we derive and validate a mean-field modeling approach that is applicable to the dynamics of RyR clusters coupled via microdomain Ca^{2+} and nearest-neighbor allosteric interactions. Similar to the sticky-cluster model presented by Sobie and co-workers [Sobie et al., 2002], the mean-field approach aggregates states based on the number of open RyRs at a Ca^{2+} release site; however, the ‘coupling factors’ representing allosteric interactions are not post-hoc additions to the model, but rather derived from the microscopic parameters of the Ca^{2+} release site.

2.3 Model Formulation

A two-state calcium-activated RyR model

Stochastic models of single channel gating often take the form of continuous-time discrete-state Markov chains (for review see [Colquhoun and Hawkes, 1995, Smith,

2002]). For example, the state-transition diagram for a two-state Ca^{2+} -activated RyR model is defined as



where $k^+ c^\eta$ and k^- are transition rates with units of time^{-1} , k^+ is an association rate constant with units $\text{conc}^{-\eta} \text{time}^{-1}$, η is the cooperativity of Ca^{2+} binding that for the purposes of this work is fixed at 2, and c is the local $[\text{Ca}^{2+}]$. If $c(t)$ is specified, then Eq. 2.1 defines a discrete-state continuous-time stochastic process, $S(t)$, with the state space $S \in \{\mathcal{C}, \mathcal{O}\}$. When the local $[\text{Ca}^{2+}]$ is not time varying—for example, a fixed background $[\text{Ca}^{2+}]$ that we denote as c_∞ —then Eq. 2.1 corresponds to the well-known telegraph process with infinitesimal generator or Q -matrix [Colquhoun and Hawkes, 1995, Norris, 1997] given by

$$Q = (q_{ij}) = \begin{pmatrix} -k^+ c_\infty^\eta & k^+ c_\infty^\eta \\ k^- & -k^- \end{pmatrix}. \quad (2.2)$$

Each off-diagonal element of Eq. 2.2 is the probability per unit time of a transition from state i to state j ,

$$q_{ij} = \lim_{\Delta t \rightarrow 0} \frac{P\{S(t + \Delta t) = S_j | S(t) = S_i\}}{\Delta t} \quad (i \neq j),$$

and, in order to satisfy conservation of probability, the diagonal elements are selected to ensure that the row sums of Q are zero, that is, $\sum_j q_{ij} = 0$. Note that the generator matrix can be decomposed as

$$Q = K^- + c_\infty^\eta K^+ \quad (2.3)$$

where the matrices

$$K^- = \begin{pmatrix} 0 & 0 \\ k^- & -k^- \end{pmatrix} \quad \text{and} \quad K^+ = \begin{pmatrix} -k^+ & k^+ \\ 0 & 0 \end{pmatrix}$$

collect the dissociation and association rate constants respectively.

The statistical properties of the two-state channel model diagrammed in Eq. 2.1 can be calculated from the Q -matrix. For example, the probability that the channel is in state j at time $t \geq 0$ given that it was in state i at $t = 0$ is given by the elements $p_{ij}(t)$ of the matrix exponential $P = \exp(tQ)$.

2.3.1 Collective gating of RyR clusters

In a natural extension of the single channel modeling approach, a model Ca^{2+} release site composed of N channels is the *vector-valued* Markov chain,

$$\mathbf{S}(t) = \{S_1(t), S_2(t), \dots, S_N(t)\}, \quad (2.4)$$

where $S_n(t)$ is the state of channel n at time t [Ball et al., 2000]. We will denote release site configurations as a vector $\mathbf{i} = (i_1, i_2, \dots, i_N)$ where i_n is the state of channel n . The transition rate from release site configuration \mathbf{i} to \mathbf{j} denoted by q_{ij} ,

$$\begin{matrix} q_{ij} \\ (i_1, i_2, \dots, i_N) \end{matrix} \rightarrow (j_1, j_2, \dots, j_N), \quad (2.5)$$

is nonzero if the origin (\mathbf{i}) and destination (\mathbf{j}) release site configurations are identical with the exception of one channel—that is, $i_n = j_n$ for all $n \neq n'$ where

$1 \leq n'(\mathbf{i}, \mathbf{j}) \leq N$ is the index of the channel changing state—and the $i_{n'} \rightarrow j_{n'}$ transition is included in the single channel model.

More formally, the transition rates q_{ij} for a release site composed of N identical Ca^{2+} -regulated channels (Eq. 2.2) are given by,

$$q_{ij} = \begin{cases} \bar{q}_{ij} & \text{if } \mathbf{i} = (i_1, i_2, \dots, i_{n'-1}, i_{n'}, i_{n'+1}, \dots, i_N) \text{ and} \\ & \mathbf{j} = (i_1, i_2, \dots, i_{n'-1}, j_{n'}, i_{n'+1}, \dots, i_N) \\ 0 & \text{otherwise} \end{cases} \quad (2.6a)$$

$$\bar{q}_{ij} = K^- [i_{n'}, j_{n'}] + K^+ [i_{n'}, j_{n'}] c(\mathbf{i}, \mathbf{j})^\eta, \quad (2.6b)$$

where either $K^- [i_{n'}, j_{n'}]$ or $K^+ [i_{n'}, j_{n'}]$ is the rate constant for the transition being made (only one of which is nonzero) and $c(\mathbf{i}, \mathbf{j})$ is the relevant $[\text{Ca}^{2+}]$, that is, the concentration experienced by channel $n'(\mathbf{i}, \mathbf{j})$ in the origin configuration \mathbf{i} . In the following section, we show how $c(\mathbf{i}, \mathbf{j})$ depends on the mathematical representation of the release site ultrastructure and buffered Ca^{2+} diffusion.

Although it may not be practical to do so for large release sites, the infinitesimal generator matrix, $Q = (q_{ij})$, for a model Ca^{2+} release site can be constructed by enumerating transition rates according to Eq. 2.6 and selecting the diagonal elements q_{ii} to ensure the rows sum to zero.

2.3.2 Release site ultrastructure and the calcium microdomain

Because Ca^{2+} -activated RyRs experience coupling mediated by the buffered diffusion of intracellular Ca^{2+} , the model includes a mathematical representation for the landscape of local $[\text{Ca}^{2+}]$ near the Ca^{2+} release site (the so-called Ca^{2+} microdomain) required to specify $c(\mathbf{i}, \mathbf{j})$ in Eq. 2.6b. For simplicity we assume channels are “in-

stantaneously coupled” via the Ca^{2+} microdomain [Nguyen et al., 2005, DeRemigio and Smith, 2005]—that is, the formation and collapse of the local peaks in the Ca^{2+} profile are fast compared to the dwell times of channels—and we assume the validity of linearly superposing local $[\text{Ca}^{2+}]$ increases due to individual channels at the release site [Naraghi and Neher, 1997, Smith et al., 2001]. We also assume that all channels are localized on a planar section of SR membrane ($z = 0$) so that the position of the pore of channel n can be written as $\mathbf{r}_n = x_n\hat{x} + y_n\hat{y}$.

Assuming a single high concentration Ca^{2+} buffer and using the steady-state solution of the linearized equations for the buffered diffusion of intracellular Ca^{2+} [Naraghi and Neher, 1997, Neher, 1998], the increase in $[\text{Ca}^{2+}]$ above background at position $\mathbf{r} = x\hat{x} + y\hat{y} + z\hat{z}$ is given by,

$$c(\mathbf{r}) = \sum_{n=1}^N \frac{\sigma_n}{2\pi|\mathbf{r}_n - \mathbf{r}|(D_c + \kappa_\infty D_b)} \left[1 + \frac{\kappa_\infty D_b}{D_c} \exp \frac{-|\mathbf{r}_n - \mathbf{r}|}{\lambda} \right] \quad (2.7a)$$

where

$$\frac{1}{\lambda^2} = \frac{1}{\tau} \left(\frac{1}{D_b} + \frac{\kappa_\infty}{D_c} \right), \quad (2.7b)$$

$$\frac{1}{\tau} = k_b^+ c_\infty + k_b^-, \quad (2.7c)$$

and

$$\kappa_\infty = \frac{K_b[B]_T}{(K_b + c_\infty)^2}. \quad (2.7d)$$

In these equations, the sum is over all channels at the release site, σ_n is the source amplitude of channel n (number of Ca^{2+} ions per unit time), D_c and D_b are the diffusion coefficients for free Ca^{2+} and the Ca^{2+} buffer respectively, k_b^+ is the buffer association rate constant, k_b^- is the buffer dissociation rate constant, $K_b = k_b^-/k_b^+$, and $[B]_T$ is the total concentration of the Ca^{2+} buffer. Assuming all RyRs have

identical source amplitudes,

$$\sigma_n(t) = \begin{cases} 0 & \text{if channel } n \text{ is closed} \\ \bar{\sigma} & \text{if channel } n \text{ is open,} \end{cases} \quad (2.8a)$$

and

$$\bar{\sigma} = \frac{i_{\text{Ca}}}{2F} \quad (2.8b)$$

where i_{Ca} is the unitary current of each channel, 2 is the valence of Ca^{2+} , and F is Faraday's constant.

While Eqs. 2.7–2.8 define the $[\text{Ca}^{2+}]$ at any position \mathbf{r} for a given release site ultrastructure, $\{\mathbf{r}_n\}$, it is helpful to summarize channel-to-channel Ca^{2+} interactions using an $N \times N$ ‘coupling matrix’ $C = (c_{nm})$ that provides the increase in $[\text{Ca}^{2+}]$ over the background (c_∞) experienced by channel m when channel n is open. If $\mathbf{a}_m = x_m\hat{x} + y_m\hat{y} + r_d\hat{z}$ specifies the position of the Ca^{2+} regulatory site for channel m located a small distance r_d above the channel pore, then

$$c_{nm} = \frac{\sigma_O}{2\pi|\mathbf{r}_n - \mathbf{a}_m|(D_c + \kappa_\infty D_b)} \left[1 + \frac{\kappa_\infty D_b}{D_c} \exp \frac{-|\mathbf{r}_n - \mathbf{a}_m|}{\lambda} \right]. \quad (2.9)$$

Using this expression we can determine the Ca^{2+} concentrations needed to specify the rates of Ca^{2+} -mediated transitions in Eqs. 2.6a–2.6b, that is,

$$c(\mathbf{i}, \mathbf{j}) = c_\infty + \sum_{n=1}^N \bar{c}_{nn'} \quad (2.10a)$$

where

$$\bar{c}_{nn'} = \begin{cases} c_{nn'} & \text{if } i_n \text{ is open} \\ 0 & \text{otherwise,} \end{cases} \quad (2.10b)$$

$n'(\mathbf{i}, \mathbf{j})$ is the index of the channel changing state and i_n is the state of channel n .

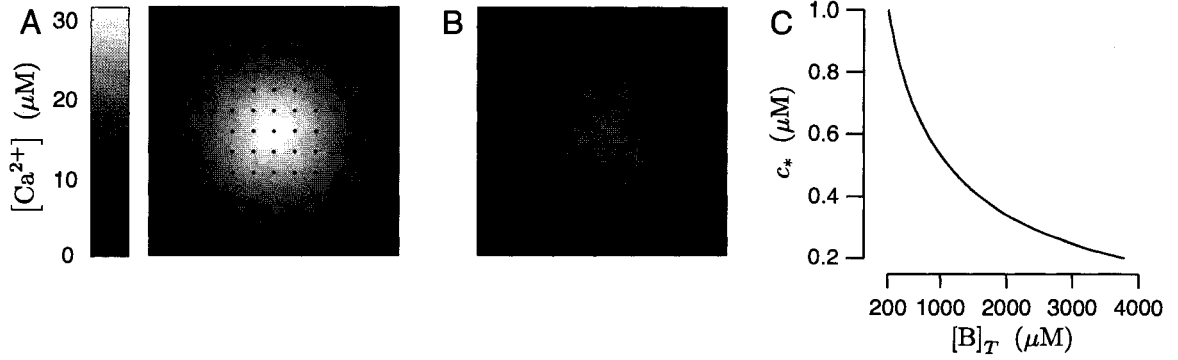


Figure 2.2: (A and B) The linearized equations for the buffered diffusion of Ca^{2+} (Eqs. 2.7a–2.8b) give the steady-state $[Ca^{2+}]$ near ($z = r_d = 30$ nm) a 360×360 nm section of planar SR membrane for a cluster of 25 open RyRs (*black dots*) organized on a Cartesian lattice with inter-channel spacing of 30 nm (see Fig. 2.1B). Individual channels are modeled as $i_{Ca} = 0.04$ pA point sources and the background $[Ca^{2+}]$ is $c_\infty = 0.1 \mu M$ while the total Ca^{2+} buffer concentration is (A) $[B]_T = 300 \mu M$ or (B) $[B]_T = 2000 \mu M$ and buffer parameters are as in Table 2.1. (C) The relationship between $[B]_T$ and the average $[Ca^{2+}]$ coupling strength (c_*) is shown for the 25 channel Ca^{2+} release site shown in A and B.

Figure 2.2A uses Eqs. 2.7–2.8 and calmodulin-like buffer parameters (see Table 2.1) to calculate the Ca^{2+} microdomain near a cluster of $N = 25$ open RyRs organized on a Cartesian lattice (Fig. 2.1B). The strength of Ca^{2+} interactions at the release site can be modified by changing any of the parameters in Eqs. 2.7–2.8, including the channel source amplitude, buffer parameters, or the diffusion constant for free Ca^{2+} . For example, Fig. 2.2B shows that increasing the total buffer concentration ($[B]_T$) decreases the local $[Ca^{2+}]$ experienced by the RyRs. Similarly, Fig. 2.2C shows that the ‘ Ca^{2+} coupling strength’ defined as the average of the off-diagonal elements of the coupling matrix,

$$c_* = \frac{1}{N(N-1)} \sum_{\substack{n,m=1 \\ n \neq m}}^N c_{nm}, \quad (2.11)$$

is a decreasing function of the total buffer concentration $[B]_T$.

2.3.3 Allosteric interactions between physically coupled channels

Following the methodology presented in [Stern et al., 1999], the RyR cluster model presented above is extended to include allosteric interactions between neighboring channels as well as Ca^{2+} -mediated coupling. We begin by defining dimensionless free energies of interaction ε_{ij} (units of $k_B T$) that specify the change in free energy experienced by a channel in state j when allosterically coupled to a channel in state i . For convenience we collect these interaction energies in an $M \times M$ matrix \mathcal{E} where M is the number of states in the single channel model and $\varepsilon_{ij} = \varepsilon_{ji}$ ($i \neq j$) in order to satisfy the requirement of thermodynamic reversibility. For the two-state single channel model considered in this paper,

$$\mathcal{E} = \begin{pmatrix} \varepsilon_{CC} & \varepsilon_{CO} \\ \varepsilon_{OC} & \varepsilon_{OO} \end{pmatrix} \quad (2.12)$$

where $\varepsilon_{CO} = \varepsilon_{OC}$. Because allosteric interactions require physical contact between neighboring RyRs, the model formulation includes a symmetric $N \times N$ adjacency matrix defined as

$$A = (a_{nm}) = \begin{cases} 1 & \text{if channel } n \text{ and } m \text{ are neighbors} \\ 0 & \text{otherwise} \end{cases} \quad (2.13)$$

where $a_{nn} = 0$ because channels do not experience allosteric interactions with themselves. The nonzero elements of A are chosen consistent with release site ultrastructure (e.g., *dotted lines* in Fig. 2.1B).

To include the effect of allosteric coupling in the Ca^{2+} release site model, the total allosteric energy experienced by channel $n'(i, j)$ in the origin and destination

configurations of an $\mathbf{i} \rightarrow \mathbf{j}$ transition are calculated as

$$\gamma_{\mathbf{i}} = \sum_{n=1}^N a_{nn'} \varepsilon_{i_n i_{n'}} \quad \text{and} \quad \gamma_{\mathbf{j}} = \sum_{n=1}^N a_{nn'} \varepsilon_{j_n j_{n'}} \quad (2.14)$$

where the sum is over all N channels, $a_{nn'}$ are elements of A , and $\varepsilon_{i_n i_{n'}}$ and $\varepsilon_{j_n j_{n'}}$ are entries of \mathcal{E} . The difference between these total allosteric energies ($\gamma_{\mathbf{j}} - \gamma_{\mathbf{i}}$) is used to modify the equilibrium constant of the $\mathbf{i} \rightarrow \mathbf{j}$ transition, that is,

$$\frac{q_{\mathbf{i}\mathbf{j}}}{q_{\mathbf{j}\mathbf{i}}} = \frac{\tilde{q}_{\mathbf{i}\mathbf{j}}}{\tilde{q}_{\mathbf{j}\mathbf{i}}} \exp[-(\gamma_{\mathbf{j}} - \gamma_{\mathbf{i}})], \quad (2.15a)$$

$$q_{\mathbf{i}\mathbf{j}} = \tilde{q}_{\mathbf{i}\mathbf{j}} \exp[-\nu_{\mathbf{i}\mathbf{j}}(\gamma_{\mathbf{j}} - \gamma_{\mathbf{i}})], \quad (2.15b)$$

and

$$q_{\mathbf{j}\mathbf{i}} = \tilde{q}_{\mathbf{j}\mathbf{i}} \exp[-\nu_{\mathbf{j}\mathbf{i}}(\gamma_{\mathbf{i}} - \gamma_{\mathbf{j}})] \quad (2.15c)$$

where $\tilde{q}_{\mathbf{i}\mathbf{j}}$ and $\tilde{q}_{\mathbf{j}\mathbf{i}}$ denote unmodified rates calculated using Eq. 2.6 and the parameters $0 \leq \nu_{\mathbf{i}\mathbf{j}} \leq 1$ and $\nu_{\mathbf{j}\mathbf{i}} = 1 - \nu_{\mathbf{i}\mathbf{j}}$ [Stern et al., 1999] partition contributions due to allosteric coupling between the forward ($q_{\mathbf{i}\mathbf{j}}$) and reverse ($q_{\mathbf{j}\mathbf{i}}$) rates. While $\nu_{\mathbf{i}\mathbf{j}}$ and $\nu_{\mathbf{j}\mathbf{i}}$ can potentially have different values for every transition $\mathbf{i} \rightarrow \mathbf{j}$, we assume transition rates involving the association of Ca^{2+} are diffusion limited. Thus, transition rates for release site configuration changes where channels make $\mathcal{C} \rightarrow \mathcal{O}$ transitions are assigned $\nu = 0$. Conversely, $\nu = 1$ for all other configuration changes where channels make $\mathcal{O} \rightarrow \mathcal{C}$ transitions.

Parameter	Value	Unit	Description
Single Channel Parameters			
k^+	0.04	$\mu\text{M}^{-\eta}\text{ms}^{-1}$	association rate constant
k^-	1	ms^{-1}	dissociation rate constant
c_∞	0.1	μM	background $[\text{Ca}^{2+}]$
η	2		cooperativity of Ca^{2+} binding
i_{Ca}	0.04	pA	effective unitary current
r_d	30	nm	pore to regulatory site distance
Buffer Parameters			
k_b^+	100	$\mu\text{M}^{-1}\text{s}^{-1}$	association rate constant
k_b^-	38	s^{-1}	dissociation rate constant
D_c	250	$\mu\text{m}^2\text{s}^{-1}$	Ca^{2+} diffusion coefficient
D_b	32	$\mu\text{m}^2\text{s}^{-1}$	buffer diffusion coefficient

Table 2.1: Default parameters used in Ca^{2+} release site simulations for both the full model and the mean-field reduction (when applicable). Single channel kinetic parameters are selected for a dissociation constant of $K_d = 5 \mu\text{M}$ [Györke and Györke, 1998]. Buffer parameters correspond to calmodulin [Smith et al., 2001, Falke et al., 1994]. Although the exact location of the Ca^{2+} -regulatory site is unknown, the pore to regulatory site distance is consistent with cryo-electron microscopy data that suggests the RyR oligomer has a large $29 \times 29 \times 12$ nm cytoplasmic assembly and a transmembrane assembly that protrudes 7 nm from the center of the cytoplasmic assembly [Radermacher et al., 1994, Fill and Copello, 2002]. The unitary current of RyRs in planar lipid bilayer has been estimated to be 0.4–0.6 pA [Mejía-Alvarez et al., 1999, Kettlun et al., 2003]. However experimental evidence suggests that under physiological concentrations, Mg^{2+} reversibly blocks the channel pore, significantly reducing the open probability of the permissive state (\mathcal{O}) [Györke and Györke, 1998, Mejía-Alvarez et al., 1999, Kettlun et al., 2003]. The unitary current used here reflects the fact that we do not explicitly model the binding and unbinding of Mg^{2+} or other phenomena that reduce the effective source amplitude of the channel, such as localized depletion of luminal Ca^{2+} .

2.4 Results

2.4.1 Calcium and allosteric coupling at a three RyR cluster

To clarify the model formulation, transition rate expressions corresponding to the example configuration changes shown in Fig. 2.3A are written below. These configuration changes involve a triangular cluster of three two-state RyRs experiencing

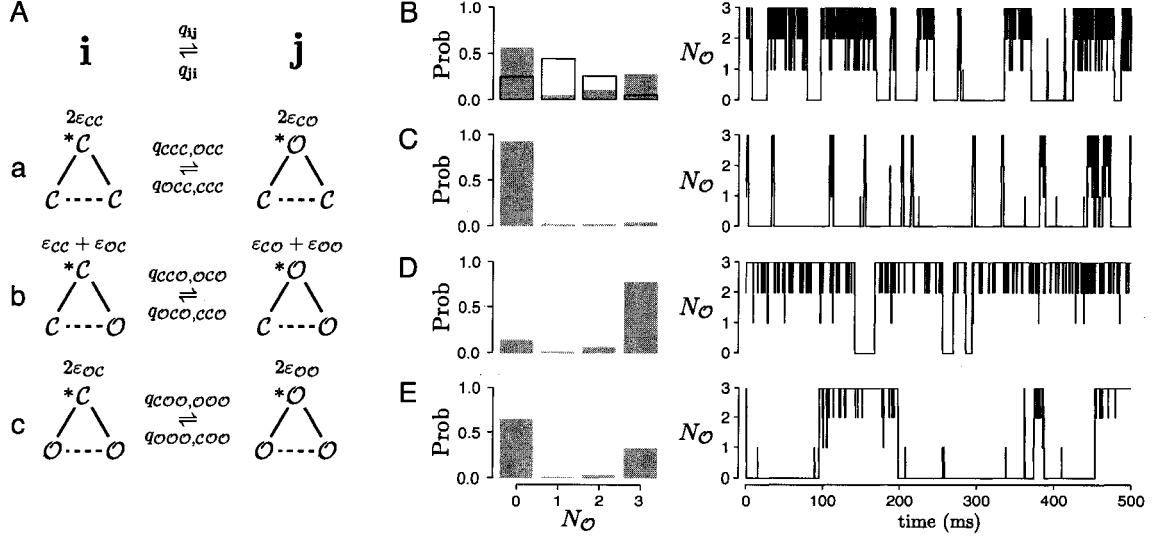


Figure 2.3: (A) Example configuration changes involving three two-state RyRs with pore-to-pore inter-channel spacing of 30 nm. Allosteric interactions are indicated by *solid* and *dashed lines*. Transition rates depend on the allosteric interactions of the channel changing state (*solid lines*) shown above each configuration. (B) RyR collective gating when channels experience coupling via the Ca^{2+} microdomain ($[\text{B}]_T = 3566 \mu\text{M}$, $c_* = 0.75 \mu\text{M}$) but no allosteric interactions ($\epsilon_{CC} = \epsilon_{OO} = 0$). *Gray bars* show the steady-state probability distribution for the number of open channels (N_O) at the release site. *White bars* give the binomial distribution with the same mean as *gray bars*; the difference shows that channels do not gate independently. (C, D, and E) RyR collective gating when in addition to Ca^{2+} coupling ($c_* = 0.75 \mu\text{M}$), channels experience allosteric interactions that stabilize closed channel pairs (C: $\epsilon_{CC} = -0.8$, $\epsilon_{OO} = 0$), open channel pairs (D: $\epsilon_{CC} = 0$, $\epsilon_{OO} = -0.8$), or both in a balanced fashion (E: $\epsilon_{CC} = \epsilon_{OO} = -0.8$). Parameters: $k^+ = 1.5 \mu\text{M}^{-\eta}\text{ms}^{-1}$, $k^- = 0.5 \text{ms}^{-1}$, and as in Table 2.1.

Ca^{2+} coupling and nearest-neighbor allosteric interactions. The corresponding Ca^{2+} coupling matrix and allosteric adjacency matrix are

$$C = \begin{pmatrix} c_{11} & c_{12} & c_{13} \\ c_{21} & c_{22} & c_{23} \\ c_{31} & c_{32} & c_{33} \end{pmatrix} \quad \text{and} \quad A = \begin{pmatrix} 0 & 1 & 1 \\ 1 & 0 & 1 \\ 1 & 1 & 0 \end{pmatrix} \quad (2.16)$$

respectively where the c_{nm} are determined using Eq. 2.9. In each panel, the total allosteric energy (Eq. 2.14) experienced by the RyR changing state (labeled with *asterisks*) is calculated for both the origin (i) and destination (j) configurations.

The $i \rightarrow j$ configuration changes shown in Fig. 2.3A each involve an RyR making a Ca^{2+} -mediated $\mathcal{C} \rightarrow \mathcal{O}$ transition (see Eq. 2.1) at rate q_{ij} that is a function of $c(i, j)$, that is, the $[\text{Ca}^{2+}]$ experienced by the channels changing state (Eq. 2.10). Let us number the RyRs in a counter-clockwise fashion beginning with the channel changing state. For the $CCC \rightarrow OCC$ configuration change shown in Fig. 2.3Aa, $c(i, j) = c_\infty$ because all channels are closed in the origin configuration CCC . For the $CCO \rightarrow OCO$ configuration change $c(i, j) = c_\infty + c_{31}$ because channel 3 is open in configuration CCO (Fig. 2.3Ab). Similarly, for the $COO \rightarrow OOO$ configuration change $c(i, j) = c_\infty + c_{21} + c_{31}$ (Fig. 2.3Ac). Having determined the appropriate $[\text{Ca}^{2+}]$ concentrations, Eq. 2.6b is used to calculate the transition rates

$$q_{ccc,occ} = k^+ c_\infty^\eta, \quad (2.17a)$$

$$q_{cco,oco} = k^+ (c_\infty + c_{31})^\eta, \quad (2.17b)$$

and

$$q_{coo,ooo} = k^+ (c_\infty + c_{21} + c_{31})^\eta. \quad (2.17c)$$

Because it is assumed that configuration changes that involve the binding of Ca^{2+} are diffusion limited, these rates are not modified due to allosteric interactions (i.e., $\nu_{ij} = 0$).

Conversely, $j \rightarrow i$ configuration changes shown in Fig. 2.3A involve channels making unimolecular $\mathcal{O} \rightarrow \mathcal{C}$ transitions at the base rate $q_{ji} = k^-$ that is modified by the change in allosteric interaction energy experienced by the channel

changing state. Using $\nu_{ji} = 1$, the rates for $j \rightarrow i$ configuration changes are given by (Eq. 2.15c)

$$q_{OCC,CCC} = k^- \exp[-2(\varepsilon_{CC} - \varepsilon_{CO})], \quad (2.18a)$$

$$q_{OCO,CCO} = k^- \exp[-((\varepsilon_{CC} - \varepsilon_{CO}) + (\varepsilon_{OC} - \varepsilon_{OO}))], \quad (2.18b)$$

and

$$q_{OOO,COO} = k^- \exp[-2(\varepsilon_{OC} - \varepsilon_{OO})]. \quad (2.18c)$$

Note that in these transition rate expressions, the elements of the allosteric interaction energy matrix occur as the differences $\varepsilon_{CC} - \varepsilon_{CO}$ and $\varepsilon_{OC} - \varepsilon_{OO}$. Because this is true regardless of the number of channels, we may without loss of generality fix $\varepsilon_{CO} = \varepsilon_{OC} = 0$. That is, we will probe the effects of allosteric interactions on Ca^{2+} release site dynamics by varying only the change in free energy due to allosterically interacting closed-closed (ε_{CC}) and open-open (ε_{OO}) channel pairs. Because we are primarily concerned with the effects of allosteric interactions that promote synchronous gating, we assume allosteric interactions stabilize closed-closed and/or open-open channel pairs (i.e., $\varepsilon_{CC} \leq 0$ and $\varepsilon_{OO} \leq 0$). For simplicity, we focus on three allosteric coupling paradigms in which allosteric interactions stabilize 1) closed-closed channel pairs ($\varepsilon_{CC} < 0$, $\varepsilon_{OO} = 0$), 2) open-open channel pairs ($\varepsilon_{CC} = 0$, $\varepsilon_{OO} < 0$), and 3) both closed-closed and open-open channel pairs in a balanced fashion ($\varepsilon_{CC} = \varepsilon_{OO} < 0$).

The simulations shown in Fig. 2.3B-E demonstrate how synchronizing allosteric interactions included in these three ways affect the dynamics of the synchronous gating of the three RyRs. Simulations are carried out using the exact numerical method presented in Section 4.2 and, for simplicity, the configuration of the RyRs is summarized by plotting only the number of open channels (N_O) as a function of time. Interestingly, Fig. 2.3B demonstrates that synchronizing allosteric interac-

tions are not required ($\varepsilon_{CC} = \varepsilon_{OO} = 0$) for channels to exhibit synchronous gating. Rather, channels may exhibit coupled gating that is mediated entirely via the buffered diffusion of local Ca^{2+} as long as the average Ca^{2+} coupling strength is sufficient ($c_* = 0.75 \mu\text{M}$) [Nguyen et al., 2005]. Gray bars in the left panel of Fig. 2.3B show the steady-state probability distribution for the number of open RyRs ($N_{\mathcal{O}}$) directly calculated from the relevant Q -matrix as described in Section 4.3. The disagreement between these results and the *white bars*, showing a binomial distribution with the same mean, is a signature of the cooperative gating of these RyRs.

While Fig. 2.3B demonstrates that the synchronous gating of channels can be mediated entirely via Ca^{2+} , Fig. 2.3C–E show how synchronizing allosteric interactions affect the dynamics of coupled gating. For example, Fig. 2.3C demonstrates that when closed channel pairs are stabilized ($\varepsilon_{CC} = -0.8$, $\varepsilon_{OO} = 0$) the steady-state probability of having zero open channels ($N_{\mathcal{O}} = 0$) increases while the probability of $N_{\mathcal{O}} = 3$ decreases relative to Fig. 2.3B. Conversely, Fig. 2.3D illustrates that when allosteric interactions stabilize open channel pairs ($\varepsilon_{CC} = 0$, $\varepsilon_{OO} = -0.8$), the probability of having a maximumly activated release site ($N_{\mathcal{O}} = 3$) increases. In Fig. 2.3E allosteric interactions stabilize closed-closed and open-open channel pairs in a balanced fashion ($\varepsilon_{CC} = \varepsilon_{OO} = -0.8$) and the probability of both $N_{\mathcal{O}} = 0$ and $N_{\mathcal{O}} = 3$ increases while the probability of $N_{\mathcal{O}} = 1$ and $N_{\mathcal{O}} = 2$ decreases compared to Fig. 2.3B.

2.4.2 Effects of calcium and allosteric coupling strength on spontaneous sparks

The previous section demonstrated how the dynamics of coupled RyR gating may depend on synchronizing allosteric interactions that stabilize closed channel pairs, open channel pairs, or both in a balanced fashion. In this section, we investigate how

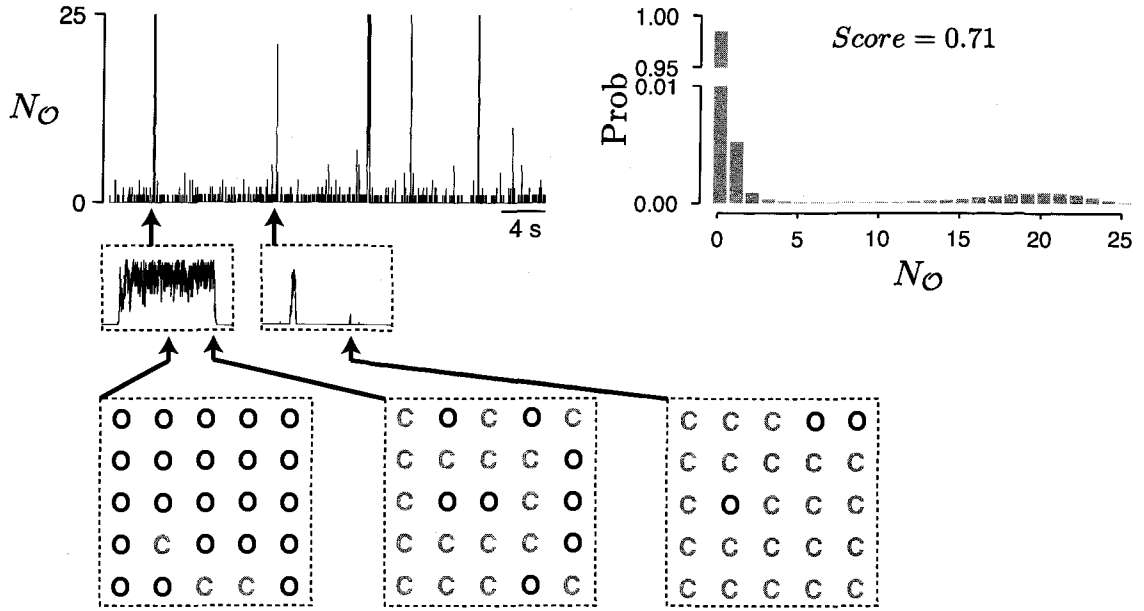


Figure 2.4: A Ca^{2+} release site simulation involving 25 RyRs organized on a Cartesian lattice exhibits stochastic Ca^{2+} excitability reminiscent of spontaneous sparks when channels experience coupling via increases in the local $[\text{Ca}^{2+}]$ ($[\text{B}]_T = 937.5 \mu\text{M}$, $c_* = 0.55 \mu\text{M}$) and nearest-neighbor allosteric interactions that stabilize closed channel pairs ($\varepsilon_{CC} = -0.2$, $\varepsilon_{OO} = 0$). *Insets* expand 50 ms of the simulation beginning at the times indicated by arrows and show ‘snap shots’ giving the states of all 25 RyRs at the release site. The Ca^{2+} spark *Score* corresponding to the simulation is calculated using Eq. 2.19 and the steady-state probability distribution for the number of open channels (N_O) at the release site (*right panel*) estimated from a long (> 20 s) Monte Carlo simulation as described in Section 4.3. Parameters as in Table 2.1.

Ca^{2+} spark formation and collapse depend on both the strength of coupling mediated by the Ca^{2+} microdomain and the strength of synchronizing allosteric interactions introduced in one of these three ways. To mimic the number and arrangement of channels observed experimentally, simulations involve release sites composed of 25 nearest-neighbor coupled RyRs organized on a Cartesian lattice (see Fig. 2.1). Note that nearest-neighbor coupling implies that each channel experiences allosteric interactions with 2–4 other channels, while increases in the Ca^{2+} microdomain due to open RyRs are experienced by all channels.

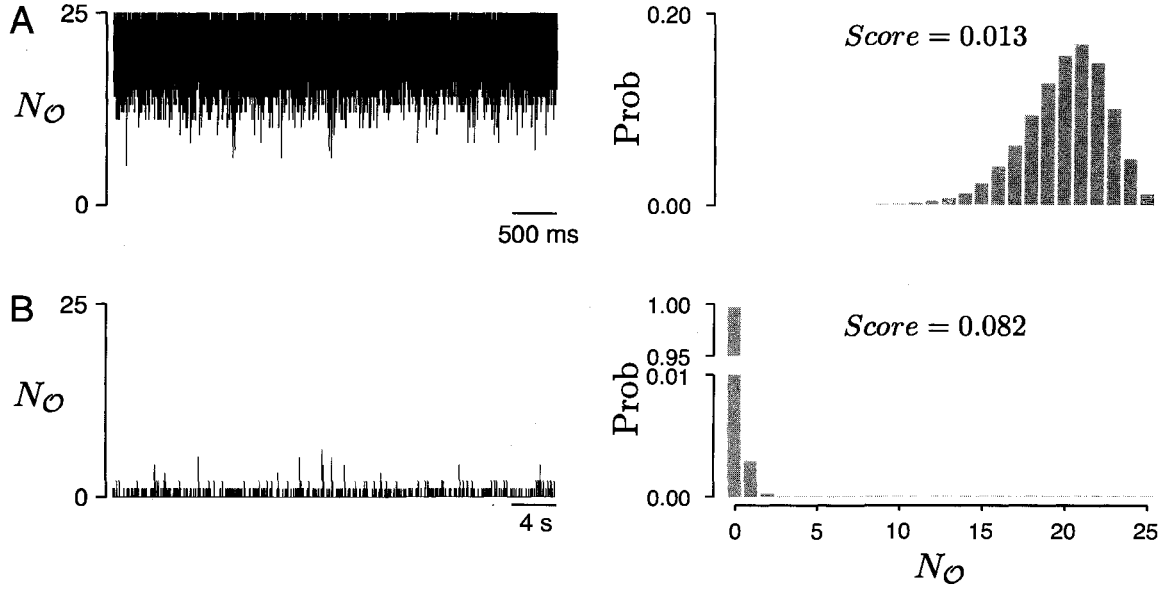


Figure 2.5: Ca^{2+} sparks exhibited in Fig. 2.4 are sensitive to changes in the strength of allosteric interactions that stabilize closed channel pairs only when the strength of Ca^{2+} interactions is fixed ($c_* = 0.55 \mu\text{M}$). (A) Sparks fail to terminate when allosteric interactions are not included ($\varepsilon_{CC} = -0.2$, $\varepsilon_{OO} = 0$). (B) Sparks fail to initiate when the strength of allosteric interactions that stabilize closed channel pairs is increased ($\varepsilon_{CC} = -0.4$, $\varepsilon_{OO} = 0$). Histograms for the number of open channels shown in *right panels* (see Fig. 2.4) are used to calculate the *Score* of each simulation. Parameters as in Table 2.1.

Figure 2.4 shows a simulation in which the strength of allosteric interactions ($\varepsilon_{CC} = -0.2$, $\varepsilon_{OO} = 0$) and Ca^{2+} coupling ($c_* = 0.55 \mu\text{M}$) are selected to illustrate the phenomenon of ‘stochastic Ca^{2+} excitability’ reminiscent of spontaneous Ca^{2+} sparks. While the channels at the release site are closed most of the time ($N_O < 5$), on occasion the RyRs simultaneously open ($N_O \approx 25$). Figure 2.5 shows that the sparks observed in Fig. 2.4 are sensitive to changes in the strength of allosteric interactions that stabilize closed channel pairs. For example, the release site is tonically active when allosteric interactions are not included in simulations ($\varepsilon_{CC} = \varepsilon_{OO} = 0$, Fig. 2.5A). On the other hand, sparks fail to initiate when the strength of allosteric interactions that stabilize closed channel pairs is greater than in Fig. 2.4 ($\varepsilon_{CC} = -0.4$, $\varepsilon_{OO} = 0$,

Fig. 2.5B).

A response measure that is strongly correlated with the presence of sparks in Monte Carlo simulations is the so-called Ca^{2+} spark *Score* introduced in [Nguyen et al., 2005]. The *Score* is defined as the index of dispersion of the fraction of open channels ($f_{\text{O}} = N_{\text{O}}/N$) and is given by

$$\text{Score} = \frac{\text{Var}[f_{\text{O}}]}{\text{E}[f_{\text{O}}]} = \frac{1}{N} \frac{\text{Var}[N_{\text{O}}]}{\text{E}[N_{\text{O}}]}. \quad (2.19)$$

Score values greater than 0.3 are indicative of spark-like excitability in stochastic Ca^{2+} release site simulations [Nguyen et al., 2005, DeRemigio and Smith, 2005]. For example, using the observed probability distribution for the number of open channels at the release site estimated from a long Monte Carlo simulation as described in Section 4.3 (Fig. 2.4 *right*), the *Score* corresponding to the simulation shown in Fig. 2.4 is a high value of 0.71. Conversely, the tonically active release site shown in Fig. 2.5A has a low *Score* of 0.013 because $\text{E}[N_{\text{O}}]$ is large. The quiescent release site shown in Fig. 2.5B also has a low *Score* of 0.082.

While Fig. 2.4 and 2.5 demonstrated that Ca^{2+} sparks are sensitive to changes in the strength of allosteric interactions that stabilize closed channel pairs, Fig. 2.6A shows that sparks observed in simulations of a 25 RyR release site are also sensitive to the Ca^{2+} coupling strength. For example, *triangles* show the *Score* (reported as the mean \pm SD of ten Monte Carlo simulations) as a function of c_* when the strength of allosteric interactions that stabilize closed channel pairs is $\varepsilon_{\text{CC}} = -0.2$ as in Fig. 2.4. The Ca^{2+} coupling strength (c_*) is systematically varied by increasing or decreasing the total buffer concentration ($[\text{B}]_T$). Note that sparks are observed in simulations (*Score* $>$ 0.3) over a range of Ca^{2+} coupling strengths but are not observed (*Score* $<$ 0.3) in simulations that use $c_* < 0.45 \mu\text{M}$ because the Ca^{2+} coupling

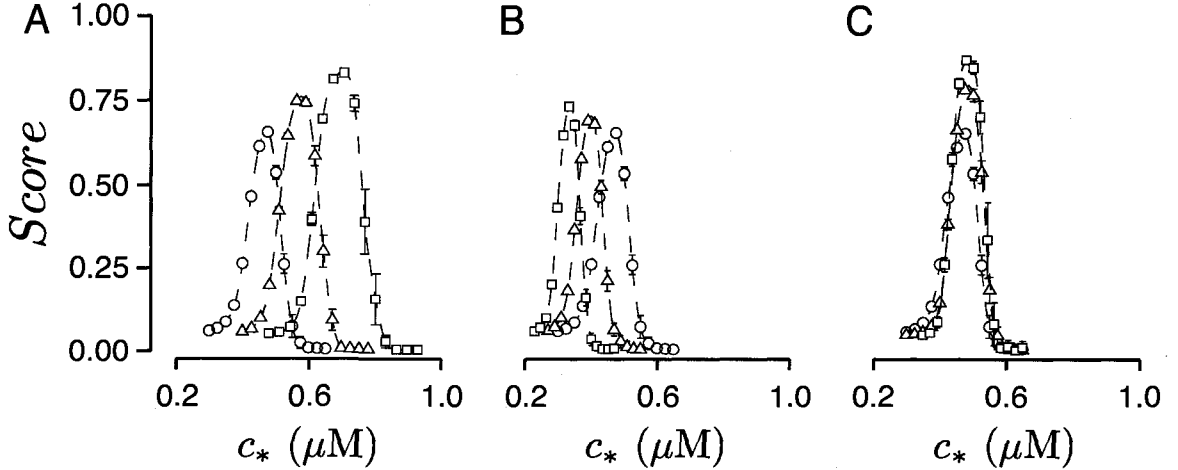


Figure 2.6: (A, B, and C) The Ca^{2+} spark *Score* (mean \pm SD of 10 long (> 20 s) Monte Carlo simulations involving 25 RyRs organized on a Cartesian lattice with random initial conditions) as a function of the Ca^{2+} coupling strength (c_*) and the strength of nearest-neighbor allosteric interactions that stabilize closed channel pairs (A: $\varepsilon_{OO} = 0$ and $\varepsilon_{CC} = 0$ (circles), $\varepsilon_{CC} = -0.2$ (triangles), or $\varepsilon_{CC} = -0.4$ (squares)), open channel pairs (B: $\varepsilon_{CC} = 0$ and $\varepsilon_{OO} = 0$ (circles), $\varepsilon_{OO} = -0.2$ (triangles), or $\varepsilon_{OO} = -0.4$ (squares)), or both in a balanced fashion (C: $\varepsilon_{CC} = \varepsilon_{OO} = 0$ (circles), $\varepsilon_{CC} = \varepsilon_{OO} = -0.2$ (triangles), or $\varepsilon_{CC} = \varepsilon_{OO} = -0.4$ (squares)). Data are interpolated with cubic splines (dashed lines) for clarity. Parameters as in Table 2.1.

strength is insufficient to initiate sparks. Similarly, $\text{Score} < 0.3$ when $c_* > 0.7 \mu\text{M}$ because the Ca^{2+} coupling strength is too large to allow spark termination. Fig. 2.6A also shows that the optimal optimal Ca^{2+} coupling strength—that is, the c_* resulting in the highest *Score*—is sensitive to the strength of allosteric interactions that stabilize closed channels. Indeed, comparing *circles* ($\varepsilon_{CC} = 0$) and *squares* ($\varepsilon_{CC} = -0.4$) to *triangles* ($\varepsilon_{CC} = -0.2$) we notice that the optimal c_* is an increasing function of the magnitude of ε_{CC} . In comparison, Fig. 2.6B demonstrates that as the strength of allosteric interactions that stabilize open channel pairs increases, the optimal c_* decreases. On the other hand, Fig. 2.6C shows that increasing the strength of allosteric interactions that stabilize both closed-closed and open-open channel pairs in a balanced fashion has little effect on the optimal value of c_* .

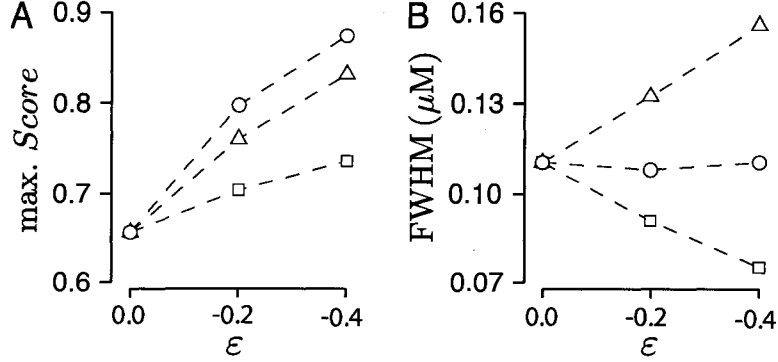


Figure 2.7: (A) The *Score* at the optimal c_* (max. *Score*) and (B) the full-width at half-maximum (FWHM) of the cubic spline fits of data in Fig. 2.6 are plotted as a function of the strength of stabilizing allosteric interactions (ϵ) when allosteric interactions stabilize closed channel pairs (*triangles*, $\epsilon_{CC} = \epsilon$, $\epsilon_{OO} = 0$), open channel pairs (*squares*, $\epsilon_{CC} = 0$, $\epsilon_{OO} = \epsilon$), or both in a balanced fashion (*circles*, $\epsilon_{CC} = \epsilon_{OO} = \epsilon$).

Fig. 2.6 demonstrates that sparks depend on c_* , ϵ_{OO} , and ϵ_{CC} in a complicated manner. For example, sparks that are eliminated as c_* increases may be recovered by increasing the strength of allosteric interactions that stabilize closed channel pairs (ϵ_{CC}) or by decreasing the strength of allosteric interactions that stabilize open channel pairs (ϵ_{OO}). On the other hand, sparks that are eliminated as c_* decreases may be recovered by decreasing the magnitude of ϵ_{CC} or increasing the magnitude of ϵ_{OO} . Note that for all three types of allosteric interactions there are Ca^{2+} coupling strengths (c_*) for which stronger interactions lead to more robust sparks. Indeed, summary plots in Fig. 2.7A show that the *Score* at these optimal c_* values is a monotonically increasing function of the strength of allosteric interactions. Interestingly, the *Score* is enhanced the most when both closed-closed and open-open channel pairs are increasingly stabilized in a balanced fashion (*circles*).

In Fig. 2.7B the sensitivity of sparks to the Ca^{2+} coupling strength is quantified using the full width at half-maximum (FWHM) of cubic spline fits to the results

of Fig. 2.6 (*dashed lines*); a larger FWHM implies less sensitivity to changes in c_* . The *triangles* of Fig. 2.7B show that sparks are less sensitive to variations in c_* as the strength of allosteric interactions that stabilize closed channel pairs increases. Conversely, the *squares* show that sparks are more sensitive to c_* as the strength of allosteric interactions that stabilize open channel pairs increases. The *circles* show that increasing the strength of allosteric interactions that stabilize both closed-closed and open-open channel pairs in a balanced fashion has little effect on the FWHM.

2.4.3 The effect of washing out allosteric interactions on spark statistics

In the previous section we showed how the presence or absence of Ca^{2+} sparks depends on both the strength of Ca^{2+} coupling (c_*) and the strength of stabilizing allosteric interactions (ε_{CC} and ε_{OO}). Next, we investigate how spark statistics (duration, inter-spark interval, and frequency) are affected by ‘washing out’ stabilizing allosteric interactions, that is, we study how these spark statistics change as an increasing fraction of nearest-neighbor allosteric couplings are randomly removed. Many experimental studies show that genetic deficiencies in, and the pharmacological washout of, the FK-binding proteins that mediate allosteric interactions lead to cardiac arrhythmias and changes in spark dynamics [Ji et al., 2004, Yoshihara et al., 2005, Gómez et al., 2004]. The following simulations aim to clarify how these experimental results can be interpreted as evidence for allosteric interactions that stabilize closed channel pairs, open channel pairs, or both (see Discussion).

The *gray bars* in Fig. 2.8A are probability distributions of spark duration and inter-spark interval estimated from multiple spark simulations (the mean is indicated by *gray triangles*). As in Fig. 2.4, 25 RyRs experience nearest-neighbor allosteric

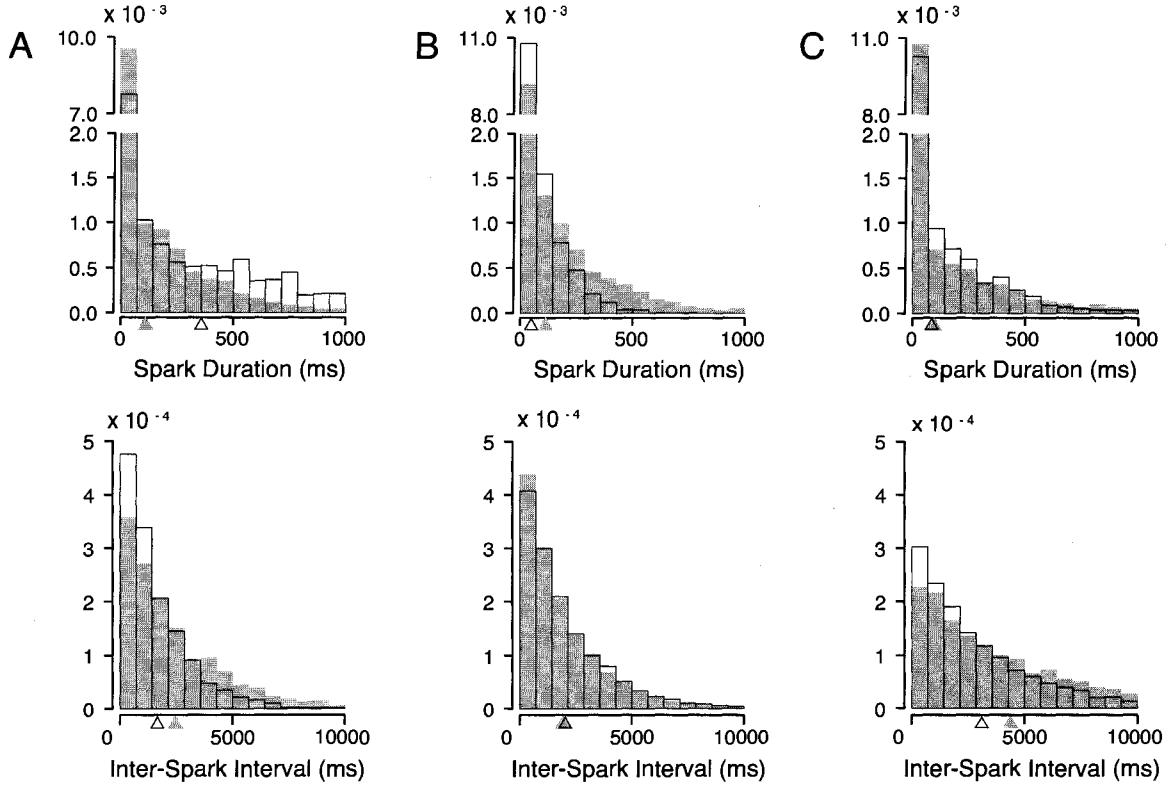


Figure 2.8: *Gray bars* are probability distributions of Ca^{2+} spark duration and inter-spark interval estimated from simulations involving 25 RyRs organized on a Cartesian lattice (means indicated by *gray triangles*). RyRs experience coupling via the Ca^{2+} microdomain (*A*: $c_* = 0.58$, *B*: $c_* = 0.40$, *C*: $c_* = 0.48 \mu\text{M}$) and nearest-neighbor allosteric interactions that stabilize closed channel pairs (*A*: $\varepsilon_{CC} = -0.2$, $\varepsilon_{OO} = 0$), open channel pairs (*B*: $\varepsilon_{CC} = 0$, $\varepsilon_{OO} = -0.2$), or both in a balanced fashion (*C*: $\varepsilon_{CC} = \varepsilon_{OO} = -0.2$). *White bars* (and *triangles*) are spark statistic distributions (and means) calculated when one-fifth of the nearest-neighbor allosteric couplings are selected at random and removed from simulations. Each histogram is calculated using 1200–6333 simulated sparks. Parameters as in Table 2.1.

interactions that stabilize closed channel pairs ($\varepsilon_{CC} = -0.2$, $\varepsilon_{OO} = 0$), and the Ca^{2+} coupling strength is selected to ensure a high *Score* ($c_* = 0.58 \mu\text{M}$). Spark duration is defined as the period beginning when one-fifth of the channels at the release site open ($N_{\mathcal{O}} = 4 \rightarrow 5$) and ending when all channels close ($N_{\mathcal{O}} = 0$), thus excluding small sparks from the calculation. Inter-spark interval is the time between the end of

a spark and the beginning of the subsequent spark.

For comparison, *white bars* in Fig. 2.8A are the spark duration and inter-spark interval distributions after one-fifth of the nearest-neighbor allosteric couplings are selected at random and eliminated from the simulations. Notice that this washout of allosteric interactions that stabilize closed channel pairs has the effect of increasing the expected spark duration and decreasing the expected inter-spark interval (compare *white* and *gray triangles*). On the other hand, Fig. 2.8B shows that when allosteric interactions stabilize open channel pairs ($\varepsilon_{CC} = 0$, $\varepsilon_{OO} = -0.2$, and $c_* = 0.40 \mu\text{M}$), removing one-fifth of these couplings decreases the expected spark duration with little change to the inter-spark interval. When both closed-closed and open-open channel pairs are stabilized in a balanced fashion ($\varepsilon_{CC} = \varepsilon_{OO} = -0.2$, $c_* = 0.48 \mu\text{M}$), washout of allosteric couplings decreases inter-spark interval but has little effect on spark duration (Fig. 2.8C).

To further probe the effects of washing out allosteric interactions, Fig. 2.9A and B show the mean and standard deviation of spark duration and inter-spark interval plotted against the fraction of allosteric couplings removed from simulations (denoted as ϕ). Similar to Fig. 2.8, allosteric interactions are included to stabilize closed channel pairs (*triangles*), open channel pairs (*squares*), or both in a balanced fashion (*circles*). In each case, the Ca^{2+} coupling strength (c_*) is selected to maximize the Ca^{2+} spark *Score* before the washout of synchronizing allosteric interactions ($\phi = 0$); thus, the *Score* is always a decreasing function of ϕ (not shown).

The results shown in Fig. 2.9A and B are consistent with those shown in Fig. 2.8. When allosteric interactions that stabilize closed channel pairs are washed out (increasing ϕ), spark duration increases and inter-spark interval decreases (*triangles*). When allosteric interactions that stabilize open channel pairs are washed out, spark duration decreases but inter-spark interval is largely unchanged (*squares*). When

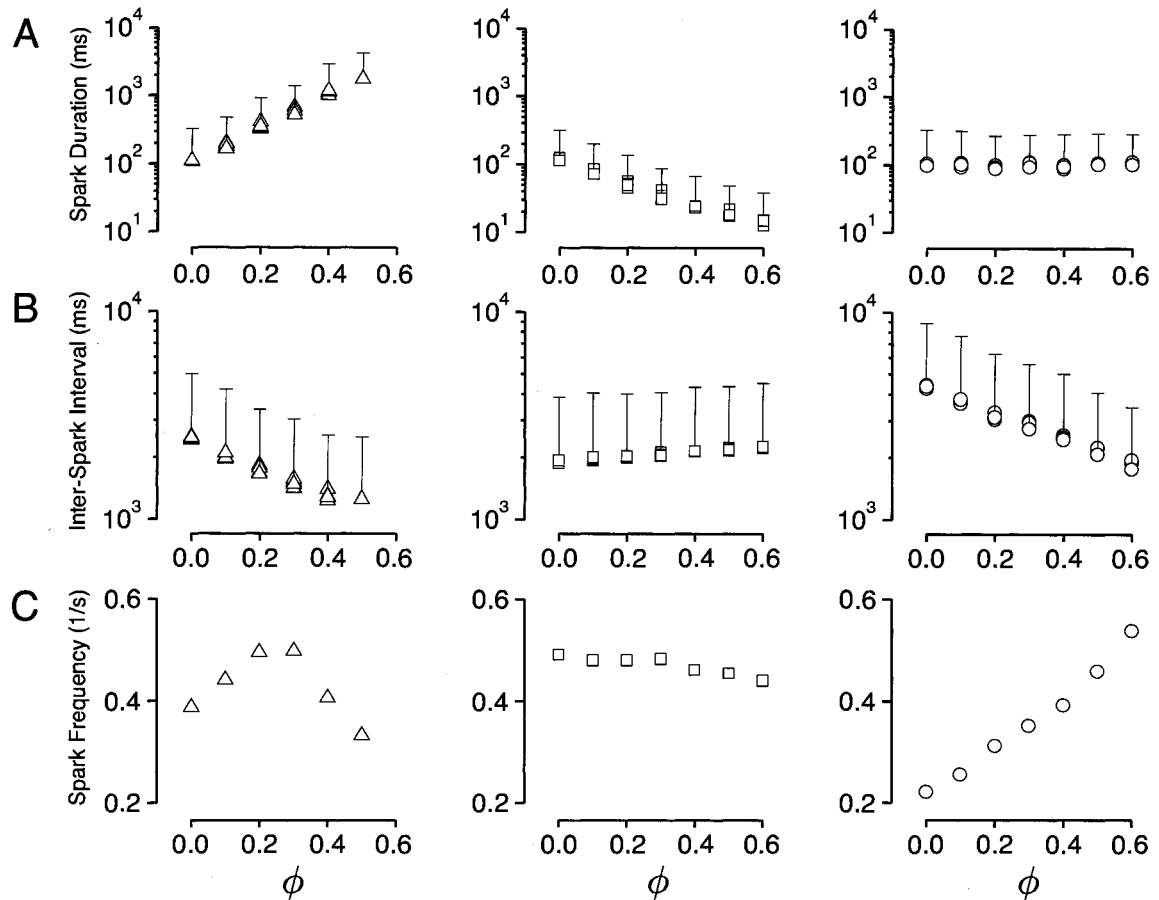


Figure 2.9: (A and B) The (A) Ca^{2+} spark duration and (B) inter-spark interval (mean + SD of distributions such as those in Fig. 2.8 calculated using 334–14,290 simulated sparks) are plotted against the fraction of allosteric couplings randomly removed from simulations (ϕ). Using parameters identical to Fig. 2.8 the 25 RyRs experience Ca^{2+} coupling and allosteric interactions that stabilize closed channel pairs (*triangles*), open channel pairs (*squares*) or both in a balanced fashion (*circles*). Multiple symbols at each ϕ show results from simulations that use different realizations of the allosteric adjacency matrix A (see text). (C) The spark frequency plotted against ϕ is calculated using the data from A and B that include *bars*. Spark statistics are reported at a given value of ϕ only if the Ca^{2+} spark *Score* > 0.3 .

both closed-closed and open-open channel pairs are stabilized in a balanced fashion, washout causes inter-spark interval to decrease but spark duration is unchanged (*circles*). Notice that the standard deviations (*bars*) of spark statistics are approximately

proportional to the means regardless of the degree of washout.

Because the allosteric couplings washed out in the simulations of Fig. 2.9A and B are randomly selected, there are many realizations of the allosteric adjacency matrix A consistent with any nonzero ϕ . To show the effects of variations in allosteric connectivity on spark dynamics, multiple symbols plotted at each value of ϕ show the mean spark duration and inter-spark interval using different realizations of A . The proximity of these symbols to each other at any given value of ϕ indicates that the dynamics of Ca^{2+} sparks—as measured by duration and inter-spark interval—are largely insensitive to these variations in allosteric connectivity.

Figure 2.9C shows the spark frequency—defined as the reciprocal of the sum of the mean spark duration and inter-spark interval—plotted against ϕ for the three allosteric coupling paradigms. When allosteric interactions that stabilize closed channel pairs are washed out, spark frequency increases but ultimately decreases (*triangles*). When allosteric interactions stabilize open channel pairs (*squares*), spark frequency is a nearly constant function of ϕ . When both closed-closed and open-open channel pairs are stabilized in a balanced fashion, spark frequency increases during washout (*circles*).

2.4.4 A mean-field RyR cluster model

In previous sections, we used Monte Carlo simulations to study how both the strength of Ca^{2+} coupling and stabilizing allosteric interactions contribute to the dynamics of sparks. Much of the complexity of these simulations is due to the spatially explicit account of channel-to-channel coupling represented by the Ca^{2+} coupling matrix C and the allosteric adjacency matrix A . In order to facilitate parameter studies of the effects of allosteric coupling on spark statistics, this section presents a mean-field

approximation applicable to a cluster of two-state RyRs coupled via the buffered diffusion of Ca^{2+} and nearest-neighbor allosteric interactions.

The mean-field approximation is perhaps best introduced by considering a simplified Ca^{2+} coupling matrix that takes the following form [Nguyen et al., 2005],

$$\bar{C} = \begin{pmatrix} c_d & c_* & \cdots & c_* \\ c_* & c_d & \ddots & \vdots \\ \vdots & \ddots & \ddots & c_* \\ c_* & \cdots & c_* & c_d \end{pmatrix}, \quad (2.20)$$

where the identical off-diagonal elements (c_*) are the average of the $N(N - 1)$ off-diagonal elements of the original Ca^{2+} coupling matrix C (Eq. 2.11). (The diagonal elements c_d that represent domain Ca^{2+} are inconsequential to simulations involving clusters of RyRs with no Ca^{2+} -mediated transition out of an open state.) Consider also an allosteric adjacency matrix that takes a similar simplified form,

$$\bar{A} = \begin{pmatrix} 0 & a_* & \cdots & a_* \\ a_* & 0 & \ddots & \vdots \\ \vdots & \ddots & \ddots & a_* \\ a_* & \cdots & a_* & 0 \end{pmatrix}, \quad (2.21)$$

where $0 \leq a_* \leq 1$ is the average allosteric connectivity calculated from the off-diagonal elements of the original allosteric adjacency matrix $A = (a_{nm})$,

$$a_* = \frac{1}{N(N - 1)} \sum_{n \neq m} a_{nm}. \quad (2.22)$$

Note that it is not possible to choose a release site ultrastructure so that \bar{C} is equal

to C with $N > 3$ channels on a planer membrane. Likewise, \bar{A} will not be equal to A unless allosteric coupling is all-to-all, a situation not consistent with RyR clusters in which the extent of inter-channel physical coupling is limited to nearest neighbors. Nevertheless, in simulations performed using \bar{C} and \bar{A} , the RyRs are indistinguishable and the $[\text{Ca}^{2+}]$ and allosteric interaction energy experienced by channels depends only on the number of open and closed RyRs at the release site. Importantly, simulations using \bar{C} and \bar{A} satisfy a lumpability condition that allows all release site configurations with the same number of channels in each state to be agglomerated without further approximation [Nguyen et al., 2005, Nicola, 1998]. This yields a contracted Markov chain with state-transition diagram

$$\begin{array}{ccccccccc}
 & q_{01} & q_{12} & q_{23} & & q_{N-2,N-1} & & q_{N-1,N} & \\
 0 & \rightleftharpoons & 1 & \rightleftharpoons & 2 & \rightleftharpoons & \cdots & \rightleftharpoons & N-1 & \rightleftharpoons & N \\
 & q_{10} & q_{21} & q_{32} & & q_{N-1,N-2} & & q_{N,N-1} &
 \end{array} \tag{2.23}$$

where the state of the system $S(t) \in \{0, 1, \dots, N\}$ is the number of open channels $N_{\mathcal{O}}$ at the release site and q_{ij} is the rate of the $N_{\mathcal{O}} = i \rightarrow j$ transition (see below). The number of closed channels is given by $N_{\mathcal{C}} = N - N_{\mathcal{O}}$.

Equation 2.23 describes a birth-death process with boundaries with skip-free transitions that increase ($N_{\mathcal{O}} = n \rightarrow n + 1$) or decrease ($N_{\mathcal{O}} = n \rightarrow n - 1$) the number of open channels at the release site. The $N + 1$ by $N + 1$ generator matrix corresponding

simplifies to

$$q_{n,n-1} = nk^- \exp \{-a_* [(N - n) \varepsilon_{CC} - (n - 1) \varepsilon_{OO}]\} \quad (1 \leq n \leq N). \quad (2.27)$$

Note that the mean-field RyR cluster model has only nine parameters: N , k^+ , k^- , η , c_∞ , c_* , ε_{CC} , ε_{OO} , and a_* .

2.4.5 Representative mean-field simulations

Fig. 2.10A shows representative simulations of 25 mean-field coupled RyRs arranged according to the strength of Ca^{2+} coupling (c_*) and allosteric interactions (ε_{CC}) used. These allosteric interactions stabilize closed channel pairs ($\varepsilon_{OO} = 0$) and the average allosteric connectivity is $a_* = 0.13$, as calculated using the adjacency matrix for 25 nearest-neighbor coupled RyRs organized on a Cartesian lattice (see Fig. 2.1). Notice that sparks are only observed on the diagonal panels of Fig. 2.10A, indicating that increased c_* can be compensated for by more negative ε_{CC} . Release sites are tonically active when c_* is large and ε_{CC} represents weak allosteric interactions (*upper right panels*), while release sites are quiescent when c_* is small and ε_{CC} represents strong allosteric interactions (*lower left panels*). These mean-field results are consistent with simulations that use the full model when allosteric interactions stabilize closed channel pairs (Fig. 2.4-2.5 and Fig. 2.6A). Mean-field simulations that include allosteric interactions that stabilize open channel pairs or both closed-closed and open-open channel pairs in a balanced fashion (not shown) are also consistent with the full model (Fig. 2.6B and C).

The panels of Fig. 2.10B show the birth rates ($q_{n,n+1}$) used in each column of Fig. 2.10A plotted as a function of the number of open channels at the release site ($n = N_O$). Note that while the $q_{n,n+1}$ are small when n is either small or large,

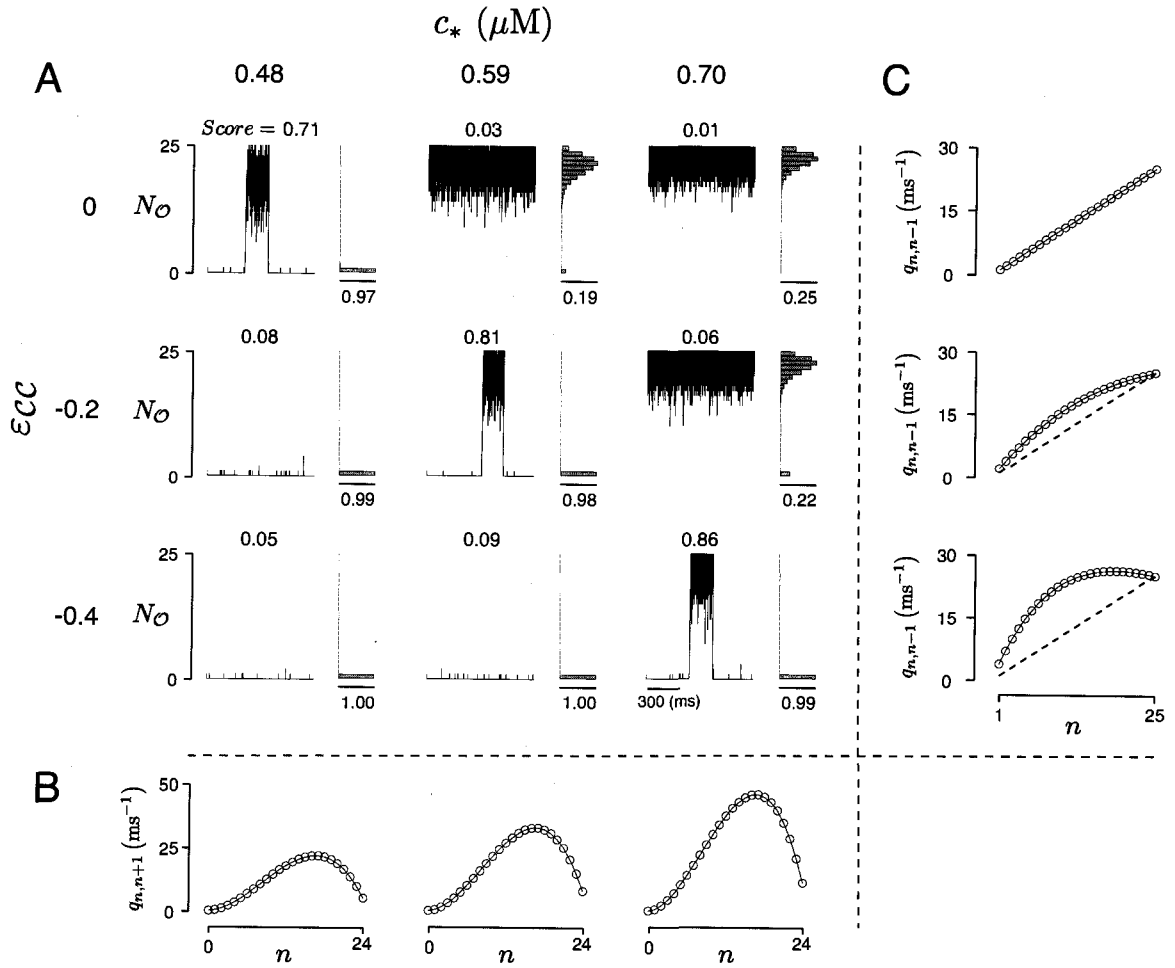


Figure 2.10: The mean-field approximation for a cluster of two-state RyRs is a birth-death process where transitions increase ($N_{\mathcal{O}} = n \rightarrow n + 1$) or decrease ($N_{\mathcal{O}} = n \rightarrow n - 1$) the number of open channels ($N_{\mathcal{O}}$) at the release site. (A) 3-by-3 grid showing example simulations involving 25 mean-field coupled RyRs as a function of c_* and ϵ_{CC} ($\epsilon_{\mathcal{O}\mathcal{O}} = 0$). The average allosteric connectivity is $a_* = 0.13$. The *Score* and steady-state probability distribution of $N_{\mathcal{O}}$ are also shown as calculated from Q (Appendix B). (B) Birth rates ($q_{n,n+1}$) used in columns of A as a function of the number of open channels ($n = N_{\mathcal{O}}$). (C) Death rates ($q_{n,n-1}$) used in rows of A. *Dashed lines* show the $q_{n,n-1}$ when allosteric interactions are not included ($\epsilon_{CC} = \epsilon_{\mathcal{O}\mathcal{O}} = 0$). Parameters as in Table 2.1.

the birth rates are accelerated for intermediate n , and this acceleration is enhanced as c_* increases. The panels of Fig. 2.10C show the death rates ($q_{n,n-1}$) used in the simulations of each row of Fig. 2.10A plotted as a function of n . Notice that when

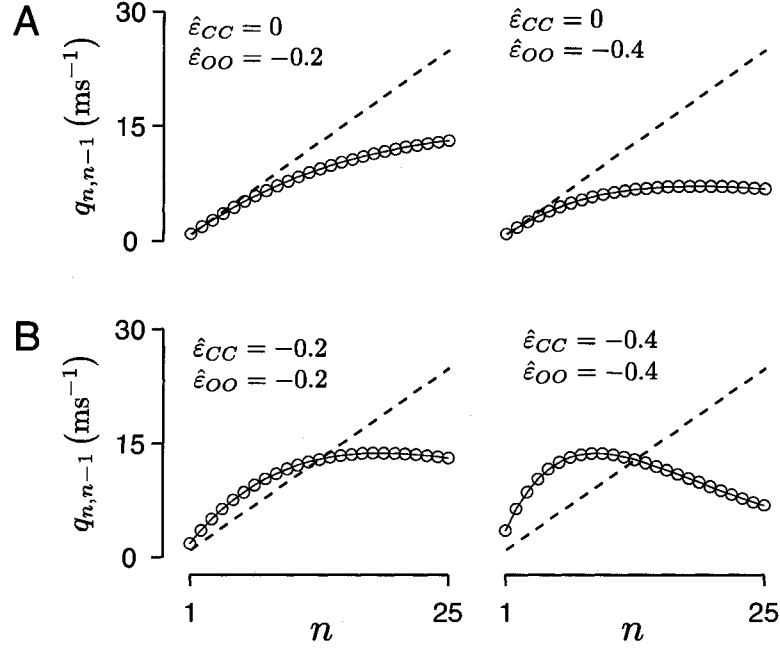


Figure 2.11: Death rates ($q_{n,n-1}$) of the mean-field approximation are plotted as a function of the number of open channels at the release site (n) with increasing strength of allosteric interactions that (A) stabilize open channel pairs or (B) both closed-closed and open-open channel pairs in a balanced fashion. *Dashed lines* show the linear relation between $q_{n,n-1}$ and n when allosteric interactions are not included ($\epsilon_{CC} = \epsilon_{OO} = 0$). Parameters as in Fig. 2.10.

allosteric interactions are not included in simulations (*top panel*, $\epsilon_{CC} = \epsilon_{OO} = 0$), $q_{n,n-1}$ is a linear increasing function of n . However, as the magnitude of ϵ_{CC} increases, $q_{n,n-1}$ is accelerated for all values of $n < N$ with the most significant acceleration at intermediate n .

While Fig. 2.10C shows how the death rates change with the strength of allosteric interactions that stabilize closed channel pairs, Fig. 2.11 shows qualitatively different changes in the death rates for allosteric interactions that stabilize open channel pairs, or both closed-closed and open-open channel pairs in a balanced fashion. When $\epsilon_{CC} = 0$, $q_{n,n-1}$ decreases for all $n > 1$ as ϵ_{OO} becomes more negative (Fig. 2.11A). On the other hand, Fig. 2.11B shows that $q_{n,n-1}$ increases for small n but decreases

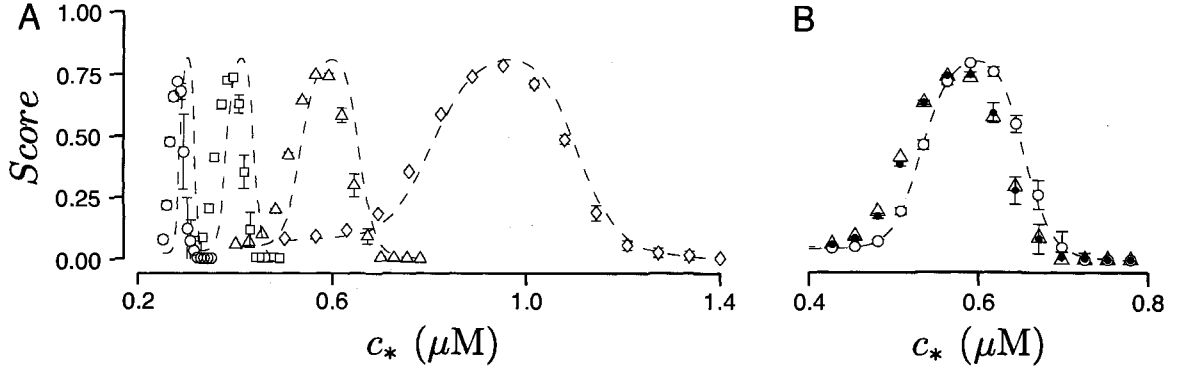


Figure 2.12: (A) The Ca²⁺ spark *Score* (mean \pm SD of 10 trials) plotted as a function of the average Ca²⁺ coupling strength (c_*) and release site size for $N = 16$ (diamonds), $N = 25$ (triangles), $N = 36$ (squares), and $N = 49$ (circles) when allosteric coupling stabilizes closed channel pairs ($\varepsilon_{CC} = -0.2$, $\varepsilon_{OO} = 0$). Dashed lines show the *Score* calculated using the mean-field approximation. The average allosteric connectivity (Eq. 2.22) is $a_* = 0.20$ (diamonds), 0.13 (triangles), 0.095 (squares), and 0.071 (circles). Other parameters as in Table 2.1. (B) Data from simulations with $N = 25$ in A are expanded (white triangles and dashed line). White circles show results from Monte Carlo simulations of the full model with nearest-neighbor allosteric coupling (A) but mean-field Ca²⁺ coupling (\bar{C}). Black circles show results from simulations with mean-field allosteric coupling (\bar{A}) but using the full Ca²⁺ coupling matrix (C).

for large n when both ε_{CC} and ε_{OO} become more negative.

2.4.6 Comparison of mean-field approximation and full model

In the previous section we demonstrated mean-field simulations may exhibit stochastic Ca²⁺ excitability reminiscent of Ca²⁺ sparks. Similar to full model simulations, these sparks are sensitive to variations of the Ca²⁺ coupling strength (c_*) and the allosteric coupling strengths (ε_{CC} , ε_{OO}) used. In this section we further validate the mean-field approximation by comparing the Ca²⁺ spark *Score* estimated from Monte Carlo simulations of the full model to the *Score* calculated directly from the Q -matrix of the corresponding mean-field model. In this comparison the c_* and a_* of the mean-field model are calculated from the C and A of the full model, and the parameters of the

single channel models used are equal.

The *symbols* in Fig. 2.12A plot the *Score* (mean \pm SD of ten trials) of Monte Carlo simulations using the full model as a function of the Ca^{2+} coupling strength (c_*) for release sites of different sizes (N) when allosteric interactions stabilize closed channel pairs ($\varepsilon_{CC} = 0$, $\varepsilon_{OO} = -0.2$). The *dashed lines* show the *Score* calculated using Q of the corresponding mean-field approximations. Both full and reduced models demonstrate that the optimal Ca^{2+} coupling strength, that is, the c_* that yields the highest *Score*, decreases as a function of N . Moreover, the range of c_* values that result in sparks ($\text{Score} > 0.3$) decreases as N increases. This inverse relationship between the optimal c_* and the release site size N , and the increase in the sensitivity of sparks to variations in c_* as N increases, are also observed when allosteric interactions stabilize open channel pairs ($\varepsilon_{CC} = 0$, $\varepsilon_{OO} = -0.2$) or both closed and open channel pairs in a balanced fashion ($\varepsilon_{CC} = \varepsilon_{OO} = -0.2$) (not shown).

Although the *Score* obtained using the full model and the mean-field approximation agree qualitatively (Fig. 2.12A), the optimal c_* and the maximum *Score* for any given value of N show quantitative differences that becomes more evident with large N . Fig. 2.12B shows that the *Score* (*white circles*) of simulations that use mean-field Ca^{2+} coupling (\bar{C}) and nearest-neighbor allosteric coupling (A) show improved agreement with mean-field model results (*dashed line*). Similarly, the *Score* (*black circles*) of simulations that use the full Ca^{2+} coupling matrix (C) and mean-field allosteric interactions (\bar{A}) show improved agreement with full model results (*white triangles*). These results suggest that the disagreement between the full model and the mean-field approximation is a consequence of the assumption of mean-field Ca^{2+} coupling and not the assumption of mean-field allosteric coupling.

2.4.7 Effect of allosteric coupling on calcium spark statistics

The reduced state space of the mean-field approximation ($N+1$) as opposed to the full model (2^N) greatly facilitates the calculation of spark statistics. For release site size of $N = 25$, the 2^N -by- 2^N Q -matrices of the full model exceed the memory limitations of modern workstations; consequently, the probability distribution for $N_{\mathcal{O}}$ and the *Score* must be estimated from Monte Carlo simulation. Because the $N+1$ -by- $N+1$ Q -matrices of the mean-field approximation are comparatively small, direct matrix analytic methods can be used to calculate these response measures (Section 4.3) as well as spark statistics such as duration, inter-spark interval, and frequency (Section 4.4).

In this matrix analytic approach it is convenient to reduce the number of parameters of the mean-field model via non-dimensionalization. Accordingly, we express Ca^{2+} concentrations in units of the dissociation constant of Ca^{2+} binding (K where $K^\eta = k^-/k^+$) and denote the non-dimensional Ca^{2+} coupling strength and background $[\text{Ca}^{2+}]$ as $\hat{c}_* = c_*/K$ and $\hat{c}_\infty = c_\infty/K$ respectively. Substituting \hat{c}_* and \hat{c}_∞ into Eq. 2.24 and expressing time in units of the reciprocal of the dissociation rate constant ($1/k^-$), we arrive at the dimensionless generator matrix $\hat{Q} = Q/k^-$. After non-dimensionalizing, the nine parameters of the mean-field model ($N, \eta, \varepsilon_{CC}, \varepsilon_{\mathcal{O}\mathcal{O}}, k^+, k^-, c_\infty, c_*$, and a_*) are reduced to seven dimensionless parameters ($N, \eta, \varepsilon_{CC}, \varepsilon_{\mathcal{O}\mathcal{O}}, \hat{c}_\infty, \hat{c}_*$, and a_*).

Using the \hat{Q} for 25 mean-field coupled RyRs, Fig. 2.13 shows spark duration, inter-spark interval, and spark frequency (in pseudocolor) as a function of the strength of dimensionless Ca^{2+} coupling (\hat{c}_*) and allosteric interactions that stabilize closed (ε_{CC}) and open ($\varepsilon_{\mathcal{O}\mathcal{O}}$) channel pairs. Each panel explores a ‘slice’ of this three dimensional parameter space indicated by the shaded region of the cubes shown at the left. These

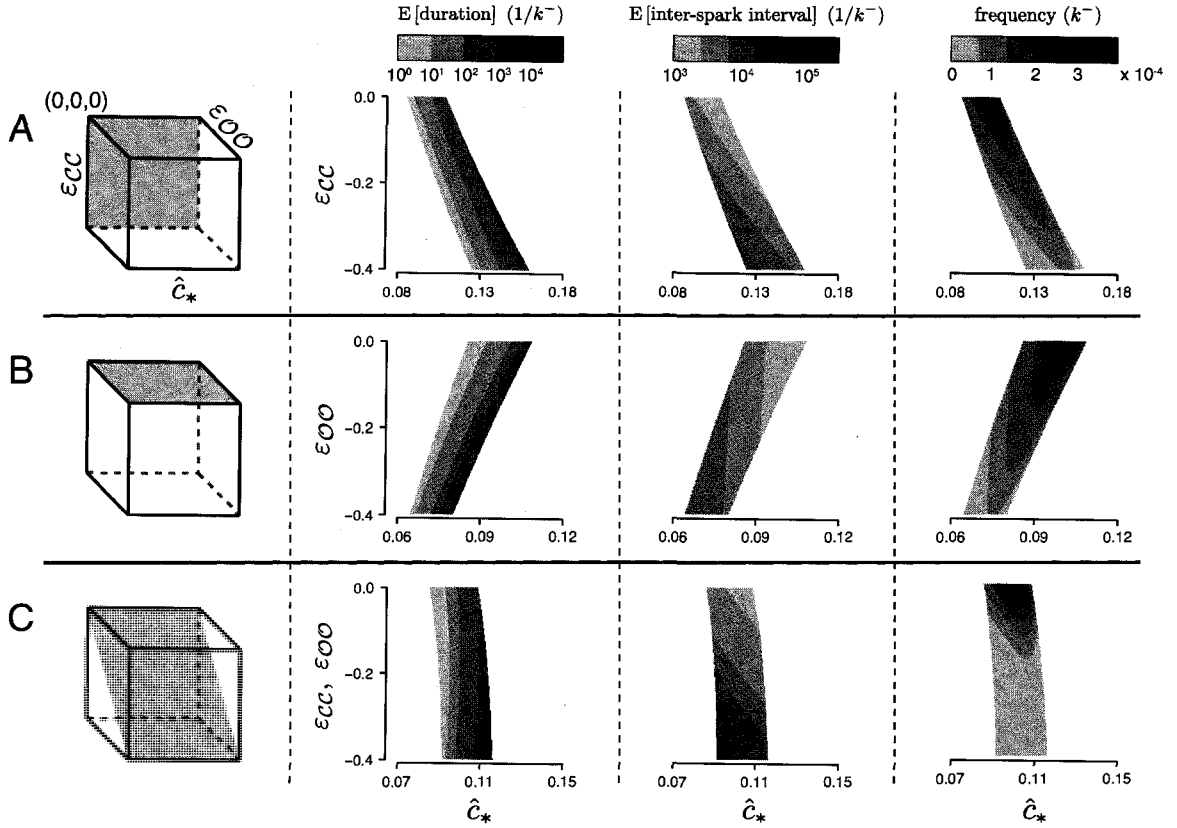


Figure 2.13: Spark duration, inter-spark interval, and spark frequency (in dimensionless units) of simulations involving 25 RyRs plotted as a function of the dimensionless strength of Ca^{2+} coupling (\hat{c}_*) and allosteric interactions when they stabilize closed channel pairs (A: $\varepsilon_{OO} = 0$), open channel pairs (B: $\varepsilon_{CC} = 0$), or both in a balanced fashion (C: $\varepsilon_{CC} = \varepsilon_{OO}$). Results are only shown when parameters result in robust sparks ($Score > 0.3$). The average allosteric connectivity is $a_* = 0.13$ and the dimensionless Ca^{2+} coupling strength is $\hat{c}_* = 0.01$. Other parameters as in Table 2.1.

correspond to allosteric interactions that stabilize closed channel pairs (Fig. 2.13A, $\varepsilon_{CC} < 0$, $\varepsilon_{OO} = 0$), open channel pairs (Fig. 2.13B, $\varepsilon_{CC} = 0$, $\varepsilon_{OO} < 0$), and both in a balance fashion (Fig. 2.13C, $\varepsilon_{CC} = \varepsilon_{OO} < 0$). Spark statistics are only shown when sparks are present ($Score > 0.3$).

Note that similar to simulations using the full model (Fig. 2.6 and 2.7), the magnitude and range of \hat{c}_* values that result in sparks increase as the strength of allosteric interactions that stabilize closed channel pairs increases (Fig. 2.13A) and decreases

as the strength of allosteric interactions that stabilize open channel pairs increases (Fig. 2.13B). The magnitude and range of \hat{c}_* values that result in sparks does not vary significantly as the magnitude of ε_{CC} and ε_{OO} increases in a balanced fashion (Fig. 2.13C). Regardless of how stabilizing allosteric interactions are introduced, spark duration and inter-spark interval are increasing and decreasing functions of \hat{c}_* , respectively. In Fig. 2.13A–C, spark duration increases and inter-spark interval decreases in such a manner that spark frequency at first increases but ultimately decreases as a function of \hat{c}_* .

While similar changes of spark statistics are seen as \hat{c}_* increases regardless of how stabilizing allosteric interactions are included, qualitatively different changes are observed in Fig. 2.13A–C as the strength of allosteric interactions increases. Fig. 2.13A shows that increasing the strength of allosteric interactions that stabilize closed channel pairs decreases spark duration and increases inter-spark interval. Figure 2.13B shows that increasing the strength of allosteric interactions that stabilize open channel pairs increases spark duration but has little effect on inter-spark interval. Fig. 2.13C shows that increasing the strength of allosteric interactions that stabilize both closed-closed and open-open channel pairs in a balanced fashion decreases inter-spark interval, while spark duration is largely unaffected. While in Fig. 2.13C spark frequency is a decreasing function of the strength of allosteric interactions, in Fig. 2.13A and B spark frequency may increase, decrease, or both depending on the coupling strength \hat{c}_* . Fig. 2.13A–C is qualitatively unchanged when the dimensionless background $[\text{Ca}^{2+}]$ (\hat{c}_∞) is doubled or halved (not shown).

2.5 Discussion

Although the biophysical mechanism of FK-binding protein-mediated coupling between RyRs is not well-understood [Marx et al., 1998, Marx et al., 2001], several studies have presented Ca^{2+} release site models that represent physical coupling using single channel transition rates that are functions of the state of other channels at the release site [Stern et al., 1999, Hinch, 2004, Sobie et al., 2002]. In the present study, physical coupling between channels is implemented using a previously introduced methodology [Stern et al., 1999, Duke and Bray, 1999, Duke et al., 2001] where transition rates are modified by state-dependent allosteric interaction energies. In this formalism the physical coupling of N M -state channels is specified by an $M \times M$ matrix of interaction energies, a $N \times N$ adjacency matrix specifying the geometry of allosteric couplings, and a partitioning coefficient for each transition that determines how the allosteric interaction energies are divided between forward and reverse rate constants. Although this formalism does not explicitly model the binding and unbinding of RyRs or FK-binding proteins to allosteric sites on neighboring channels, Fig. 2.3B-E show trajectories reminiscent of experimentally observed coupled channel gating [Marx et al., 1998, Marx et al., 2001] when this methodology is used to represent stabilizing allosteric interactions.

2.5.1 Allosteric coupling and calcium spark formation and collapse

A significant result of this study is the observation that synchronizing allosteric interactions always promote Ca^{2+} sparks (i.e., result in a higher *Score*) for some value of the strength of Ca^{2+} coupling (c_*), regardless of whether synchronizing allosteric interactions stabilize closed channel pairs, open channel pairs, or both (see Fig. 2.6

and Fig. 2.7). When the strength of Ca^{2+} coupling is sufficiently large to preclude termination of simulated sparks, allosteric interactions that stabilize closed channel pairs can promote spark termination. Similarly, allosteric interactions that stabilize open channel pairs facilitate spark initiation when Ca^{2+} coupling is too weak to mediate stochastic Ca^{2+} excitability. Sparks are less sensitive to variations in c_* when the strength of allosteric interactions that stabilize closed channel pairs is increased, and more sensitive to c_* when the strength of allosteric interactions that stabilize open channel pairs is increased.

2.5.2 Allosteric coupling washout, cardiac dysfunction, and calcium spark statistics

A substantial body of experimental evidence demonstrates that normal cardiac function requires the association of the 12.6 kDa FK506 binding protein FKBP12.6 to the RyR channel complex [Lehnart et al., 2004a, Lehnart et al., 2004b, Wehrens et al., 2003, Wehrens et al., 2004]. For example, pharmacological or exercise-induced PKA hyperphosphorylation of RyRs has been shown to substantially dissociate FKBP12.6 from RyRs and has been linked to increased frequency of ventricular arrhythmias and sudden cardiac death [Wehrens et al., 2004, Marx et al., 2000]. In addition, the absence of FKBP12.6 in knockout mice has been associated with increased systolic $[\text{Ca}^{2+}]$ and cardiac hypertrophy [Xin et al., 2002].

While the connection between FKBP12.6 depletion and cardiac dysfunction is not clearly established, evidence that FK-binding proteins are responsible for coupled gating of RyRs suggests that organ-level failure may be inherited from defects in the collective gating of channels leading to irregularities in the dynamics of Ca^{2+} sparks. In striated (skeletal and cardiac) and smooth muscle, both the frequency and duration

of spontaneous sparks increase upon knockout of genes encoding relevant FK-binding proteins or treatment with FK506 or rapamycin, two drugs that physically and/or functionally dissociate FK-binding proteins from RyRs [Xiao et al., 1997, Xin et al., 2002, Ji et al., 2004, McCall et al., 1996, Lukyanenko et al., 1998, Van Acker et al., 2004, Wang et al., 2003, Yoshihara et al., 2005]. Conversely, overexpression of FKBP12.6 has been shown to decrease spark frequency [Gómez et al., 2004]. Interestingly, these experimentally observed changes in spark duration and frequency are consistent with simulated washout of allosteric interactions that stabilize closed-closed channel pairs or both closed-closed and open-open channel pairs, but inconsistent with simulations involving the washout of allosteric interactions that stabilize only open-open channel pairs. While in principle these different types of allosteric coupling could leave a signature in the distribution of spark durations, this does not appear to be the case for the minimal two-state RyR model used here (Fig. 2.8). We also find that spark statistics are insensitive to variations in allosteric connectivity so long as average allosteric connectivity is unchanged (Fig. 2.9).

2.5.3 The mean-field approximation of allosteric interactions

The mean-field approximation formulated in this study is applicable to a cluster of RyRs coupled via both Ca^{2+} and allosteric interactions. Although this reduced model has a drastically contracted state space compared to full model simulations, the mean-field coupled RyRs exhibit Ca^{2+} sparks that are qualitatively similar to sparks of the full model (Fig. 2.12). The comparatively small state space of the mean-field approximation makes it a good starting point for models of global Ca^{2+} release events (i.e., oscillations and waves) and excitation-contraction coupling.

The mean-field reduction formulated here is analogous to the ‘sticky cluster’ model

of Sobie et al. [Sobie et al., 2002] where the coupled gating of RyRs is represented by multiplying the $\mathcal{C} \rightarrow \mathcal{O}$ and $\mathcal{O} \rightarrow \mathcal{C}$ transition rates by ‘cooperativity factors’ ($\chi_{\mathcal{O}}$ and $\chi_{\mathcal{C}}$) that depend on the number of open and closed channels in the cluster. For example, in Sobie et al. [2002] the death rates are given by $q_{n,n-1} = nk^- \chi_{\mathcal{C}}$ where

$$\chi_{\mathcal{C}} = k_{\text{coop}} \left[1 + \frac{N_{\mathcal{C}} + 1}{N} \right] \quad (2.28)$$

and the scaling factor k_{coop} sets the strength of RyR coupling. By inspecting the death rates presented in this chapter (Eq. 2.27), one finds that the ‘cooperativity factor’ in the mean-field model is

$$\chi'_{\mathcal{C}} = \exp \{ -a_* [(N - N_{\mathcal{O}}) \varepsilon_{\mathcal{C}\mathcal{C}} - (N_{\mathcal{O}} - 1) \varepsilon_{\mathcal{O}\mathcal{O}}] \}, \quad (2.29)$$

which when expressed in terms of $N_{\mathcal{C}}$ is

$$\chi'_{\mathcal{C}} = \exp \{ a_* [(N - 1) \varepsilon_{\mathcal{O}\mathcal{O}} - N_{\mathcal{C}} (\varepsilon_{\mathcal{O}\mathcal{O}} + \varepsilon_{\mathcal{C}\mathcal{C}})] \}. \quad (2.30)$$

Note that Eq. 2.28 is an increasing function of $N_{\mathcal{C}}$, consistent with Eq. 2.30 when $\varepsilon_{\mathcal{O}\mathcal{O}} + \varepsilon_{\mathcal{C}\mathcal{C}} < 0$ as in most of the simulations presented here. However, Eq. 2.30 is a nonlinear function of $N_{\mathcal{C}}$ (Eq. 2.28 is linear), and the scaling factor for the strength of allosteric coupling (a_*) enters Eq. 2.30 differently than k_{coop} in Eq. 2.28. Furthermore, $\chi'_{\mathcal{C}} = 1$ when $N_{\mathcal{C}} = 0$ and $\varepsilon_{\mathcal{O}\mathcal{O}} = 0$ (and when $N_{\mathcal{O}} = 1$ and $\varepsilon_{\mathcal{C}\mathcal{C}} = 0$) regardless of the strength of allosteric coupling (not so for $\chi_{\mathcal{C}}$ in Eq. 2.28). While Eq. 2.28 has only one free parameter (k_{coop}), we would recommend using Eq. 2.30 because the three parameters (a_* , $\varepsilon_{\mathcal{O}\mathcal{O}}$, $\varepsilon_{\mathcal{C}\mathcal{C}}$) are not post-hoc additions to an $N + 1$ state model, but rather derived from the microscopic parameters of the 2^N state Ca^{2+} release site that is reduced to $N + 1$ states using the mean-field approximation. Equation 2.30 has the

additional advantage of being able to incorporate synchronizing (or desynchronizing) allosteric interactions that stabilize (or destabilize) closed channel pairs, open channel pairs, or both.

2.5.4 Generalizing the mean-field approximation

Although the single channel model used in this paper includes only two states (closed and open), the mean-field approximation can be applied to clusters of channels with more complicated single channel dynamics that include mechanisms suspected to contribute to Ca^{2+} spark dynamics *in situ* such as luminal regulation, Ca^{2+} -dependent inactivation, or adaptation [Stern and Cheng, 2004, Györke, 1999, Györke and Györke, 1998]. For N M -state channels there are n -choose- $k\{N + M - 1, N\}$ states in the mean-field approximation, each of which can be expressed as a vector of the form (N_1, N_2, \dots, N_M) where N_m is the number of channels in state m , $1 \leq m \leq M$, and $\sum_{m=1}^M N_m = N$. If the current state of the release site is (N_1, N_2, \dots, N_M) and a channel makes an $i \rightarrow j$ transition, the transition rate is $N_i k_{ij} \chi_{ij}$ and the appropriate cooperativity factor is

$$\chi_{ij} = \exp \left[-a_* \nu_{ij} \sum_{k=1}^M (N_k - \delta_{ki}) (\varepsilon_{kj} - \varepsilon_{ki}) \right] \quad (2.31)$$

where ν_{ij} is the previously encountered coefficient that partitions allosteric coupling between the forward and reverse transitions ($0 \leq \nu_{ij} \leq 1$ and $\nu_{ji} = 1 - \nu_{ij}$), and δ_{ki} is the Kronecker delta function defined by

$$\delta_{ki} = \begin{cases} 1 & \text{if } k = i \\ 0 & \text{if } k \neq i \end{cases} \quad (2.32)$$

2.6 Conclusions

This chapter clarifies how nearest-neighbor allosteric coupling and Ca^{2+} coupling simultaneously contribute to puff and spark dynamics. The model formulated in Section 2.3 includes an accurate account of channel positions but the chapter concludes with the derivation of a mean-field approximation that assumes indistinguishable channels. While the computational advantages of the mean-field approximation are obvious, the use of the mean-field modeling approach is further justified by results showing that puff/spark statistics of mean-field simulations are often in reasonable agreement with results obtained using the full model. All of the Markov chain models of Ca^{2+} release sites in the following chapter (Chap. 3) assume mean-field Ca^{2+} coupling between three-state channels that experience both Ca^{2+} activation and Ca^{2+} inactivation. The mean-field formulation facilitates parameter studies of the effects of the kinetics and affinity of Ca^{2+} inactivation on the dynamics of puff and spark generation and termination.

Chapter 3

Calcium-Dependent Inactivation and the Dynamics of Calcium Puffs and Sparks

3.1 Summary

Localized intracellular Ca^{2+} elevations known as puffs and sparks arise from the cooperative activity of inositol 1,4,5-trisphosphate receptors (IP_3Rs) and ryanodine receptors (RyRs) clustered at Ca^{2+} release sites on the surface of the endoplasmic reticulum or sarcoplasmic reticulum. When Markov chain models of these intracellular Ca^{2+} -regulated Ca^{2+} channels are coupled via a mathematical representation of a Ca^{2+} microdomain, simulated Ca^{2+} release sites may exhibit the phenomenon of “stochastic Ca^{2+} excitability” reminiscent of Ca^{2+} puffs and sparks where channels open and close in a concerted fashion. To clarify the role of Ca^{2+} inactivation of IP_3Rs and RyRs in the dynamics of puffs and sparks, we formulate and analyze Markov chain models of Ca^{2+} release sites composed of 10–40 three-state intracellu-

lar Ca^{2+} channels that are inactivated as well as activated by Ca^{2+} . We study how the statistics of simulated puffs and sparks depend on the kinetics and dissociation constant of Ca^{2+} inactivation, and find that puffs and sparks are often less sensitive to variations in the number of channels at release sites and strength of coupling via local $[\text{Ca}^{2+}]$ when the average fraction of inactivated channels is significant. Interestingly, we observe that the single channel kinetics of Ca^{2+} inactivation influences the thermodynamic entropy production rate of Markov chain models of puffs and sparks. While excessively fast Ca^{2+} inactivation can preclude puffs and sparks, moderately fast Ca^{2+} inactivation often leads to time-irreversible puffs and sparks whose termination is facilitated by the recruitment of inactivated channels throughout the duration of the puff/spark event. On the other hand, Ca^{2+} inactivation may be an important negative feedback mechanism even when its time constant is much greater than the duration of puffs and sparks. In fact, slow Ca^{2+} inactivation can lead to release sites with a substantial fraction of inactivated channels that exhibit puffs and sparks that are nearly time-reversible and terminate without additional recruitment of inactivated channels.

3.2 Introduction

In eukaryotes, release of Ca^{2+} from intracellular stores is often mediated by inositol 1,4,5-trisphosphate receptors (IP_3Rs) or ryanodine receptors (RyRs) located on the endoplasmic (ER) or sarcoplasmic reticulum (SR) membranes. Because both IP_3Rs and RyRs are activated by cytosolic Ca^{2+} , a small increase in the $[\text{Ca}^{2+}]$ near these channels may promote the further release of intracellular Ca^{2+} , a phenomenon known as Ca^{2+} -induced Ca^{2+} release [Bers, 2002]. The dynamics of Ca^{2+} release is complicated by the fact that both RyRs and IP_3Rs are often co-localized at Ca^{2+}

release sites. For example, in the cortical regions (approximately 6 μm below the plasma membrane) of immature *Xenopus* oocytes, IP₃Rs occur in clusters of 5–50 with inter-cluster spacing on the order of a few microns [Sun et al., 1998]. IP₃Rs are also clustered on the surface of the outer nuclear membrane of *Xenopus* oocytes [Mak and Foskett, 1997]. Similarly, RyRs are assembled into paracrystalline arrays of up to 100 channels in skeletal and cardiac myocytes [Franzini-Armstrong et al., 1999b].

The clustering of IP₃Rs and RyRs results in three distinct modes of Ca²⁺ mobilization that have been observed via confocal microfluorimetry in oocytes, cardiomyocytes, and many other cell types: 1) localized Ca²⁺ elevations due to the activation of a single channel that are referred to as Ca²⁺ blips or quarks depending on whether the events are mediated by an IP₃R or RyR [Niggli, 1999, Niggli and Shirokova, 2007], 2) Ca²⁺ elevations due to the activation of multiple IP₃Rs or RyRs at a single Ca²⁺ release site known as Ca²⁺ puffs and sparks [Cheng et al., 1993, Cannell et al., 1995, Yao et al., 1995, Parker et al., 1996b], and 3) global Ca²⁺ elevations such as oscillations and waves that involve multiple release sites [Cheng et al., 1996]. These three modes of Ca²⁺ release have been dubbed fundamental, elementary, and global responses, respectively [Berridge, 1997, Berridge, 2006].

Although there is agreement that puffs and sparks arise due to the cooperative gating of Ca²⁺-regulated Ca²⁺ channels coupled via the ‘landscape’ of local [Ca²⁺] (i.e., the so-called Ca²⁺ microdomain) [Augustine et al., 2003], the mechanism by which puffs and sparks terminate is not well-understood. Experimentally observed puffs and sparks endure 10–200 ms [Cheng et al., 1993, Niggli and Shirokova, 2007]. Given the autocatalytic and regenerative nature of Ca²⁺-induced Ca²⁺ release, these short event durations suggest that puff/spark termination is facilitated by a robust negative feedback mechanism. Because puffs and sparks involve a finite number of channels, there is always a chance that termination is due to the simultaneous de-

activation of all channels at a release site, a phenomenon referred to as stochastic attrition in the cardiac myocyte literature [Stern and Cheng, 2004, DeRemigio and Smith, 2005]. Other possible negative feedback mechanisms that may contribute to puff and spark termination include: 1) direct allosteric coupling between neighboring intracellular channels, 2) depletion of luminal Ca^{2+} resulting in a diminished driving force for Ca^{2+} release [Huertas and Smith, 2007], and 3) Ca^{2+} -dependent or activity-dependent inactivation of channels (for review see [Stern and Cheng, 2004, Fill, 2002]). Although Ca^{2+} -dependent inactivation has been repeatedly observed in single-channel recordings of IP_3Rs and RyRs , the affinity and rate of Ca^{2+} inactivation depends on receptor subtype [Fabiato, 1985, Bezprozvanny et al., 1991, Bezprozvanny and Ehrlich, 1994, Györke and Fill, 1993, Lukyanenko et al., 1998, Hagar et al., 1998, Moraru et al., 1999, Fill, 2002, Stern and Cheng, 2004], and it remains unclear whether Ca^{2+} inactivation provides sufficient negative feedback to facilitate puff/spark termination *in vivo*.

When Markov chain models of these intracellular Ca^{2+} -regulated Ca^{2+} channels are coupled via a mathematical representation of a Ca^{2+} microdomain, simulated Ca^{2+} release sites may exhibit the phenomenon of “stochastic Ca^{2+} excitability” where channels open and close in a concerted fashion reminiscent of Ca^{2+} puffs and sparks [Hinch, 2004, Mazzag et al., 2005, DeRemigio and Smith, 2005, Nguyen et al., 2005, Rengifo et al., 2002, Ríos and Stern, 1997, Shuai and Jung, 2002a, Shuai and Jung, 2002b, Stern et al., 1999, Swillens et al., 1998, Swillens et al., 1999, Diambra and Guisoni, 2005, Groff and Smith, 2007a, Groff and Smith, 2007b]. Such theoretical studies have helped clarify the factors that contribute to the generation and termination of Ca^{2+} puffs and sparks. For example, puff/spark initiation requires significant inter-channel communication, that is, low density Ca^{2+} release sites exhibit a low ratio of elementary to fundamental events [Swillens et al., 1999, Nguyen et al., 2005]. Other

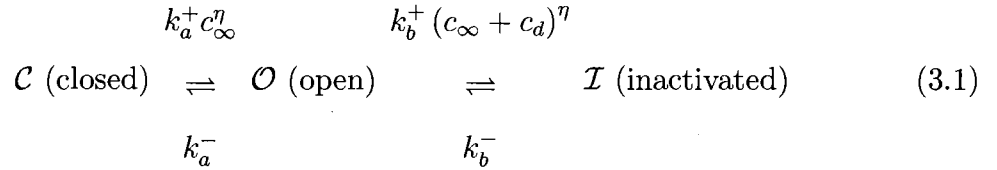
studies have demonstrated that depletion of luminal Ca^{2+} promotes the termination of puffs and sparks so long as the luminal refilling rate is sufficiently slow compared to channel kinetics [Huertas and Smith, 2007]. The presence of puffs and sparks can also be promoted by synchronizing nearest-neighbor allosteric interactions [Stern et al., 1999, Groff and Smith, 2007a, Groff and Smith, 2007b]. Some single channel models that include Ca^{2+} inactivation as well as Ca^{2+} activation are not particularly sensitive to the density or position of channels at simulated Ca^{2+} release sites, so long as the requirement for inter-channel communication is satisfied, while others are unable to generate robust puff/sparks regardless of channel density [Nguyen et al., 2005, DeRemigio et al., 2007, DeRemigio and Smith, 2007]. Puffs and sparks exhibited by coupled Ca^{2+} channels that include Ca^{2+} inactivation can often be eliminated by modifying the corresponding association and dissociation rate constants [Nguyen et al., 2005].

To clarify the role of Ca^{2+} inactivation of IP_3Rs and RyRs in the dynamics of puffs and sparks, we here formulate and analyze Markov chain models of Ca^{2+} release sites composed of 10–40 three-state intracellular Ca^{2+} channels that are inactivated as well as activated by Ca^{2+} (Section 3.3). We study how the statistics of simulated puffs and sparks (e.g., the distribution of event durations) depend on the kinetics and dissociation constant of Ca^{2+} inactivation, the number of channels, and the degree of inter-channel communication mediated by local $[\text{Ca}^{2+}]$ (Sections 3.4.1–3.4.5). We also explore how Ca^{2+} inactivation can play multiple functional roles in the generation and termination of puffs and sparks that have distinct signatures in the distribution of event durations (Section 3.4.6).

3.3 Model formulation

3.3.1 A three-state channel model with calcium activation and calcium inactivation

The stochastic gating of intracellular channels is often modeled using continuous-time Markov chains (for review see [Colquhoun and Hawkes, 1995, Smith, 2002]). The three-state single channel model that is the focus of this chapter is both activated and inactivated by Ca^{2+} ,



where $k_a^+ c_\infty^\eta$, k_a^- , $k_b^+ (c_\infty + c_d)^\eta$, and k_b^- are transition rates with units of time^{-1} , k_a^+ and k_b^+ are association rate constants with units of $\text{conc}^{-\eta} \text{time}^{-1}$, and c_∞ is a fixed background $[\text{Ca}^{2+}]$. For simplicity we assume that the cooperativity of Ca^{2+} binding, η , is the same for the activation and inactivation process. Because the $\mathcal{O} \rightarrow \mathcal{I}$ transition occurs when the channel is open and conducting Ca^{2+} , we write the $[\text{Ca}^{2+}]$ determining the rate of this transition as $c_\infty + c_d$ where c_d is the ‘domain $[\text{Ca}^{2+}]$,’ the self-induced increase in local $[\text{Ca}^{2+}]$ experienced by the channel when open. When c_∞ and c_d are specified, Eq. 3.1 defines a discrete-state continuous-time stochastic process $S(t) \in \{\mathcal{C}, \mathcal{O}, \mathcal{I}\}$ with infinitesimal generator or Q -matrix given by [Colquhoun and

Hawkes, 1995, Norris, 1997]

$$Q = (q_{ij}) = \begin{pmatrix} -k_a^+ c_\infty^\eta & k_a^+ c_\infty^\eta & 0 \\ k_a^- & -k_a^- - k_b^+ (c_\infty + c_d)^\eta & k_b^+ (c_\infty + c_d)^\eta \\ 0 & k_b^- & -k_b^- \end{pmatrix} \quad (3.2)$$

where the off-diagonal elements are transition rates

$$q_{ij} = \lim_{\Delta t \rightarrow 0} \frac{P\{S(t + \Delta t) = j | S(t) = i\}}{\Delta t} \quad (i \neq j)$$

and the diagonal elements ensure that the rows sum to zero, $\sum_j q_{ij} = 0$.

We denote the stationary or time-independent probability of being in state i as π_i and the stationary probability distribution as a vector $\boldsymbol{\pi} = (\pi_C, \pi_O, \pi_I)$. The stationary distribution satisfies both conservation of probability and global balance. That is, $\sum_i \pi_i = 1$ and the probability fluxes into and out of each state are equal,

$$\sum_{i \neq j} \pi_i q_{ij} = \pi_j \sum_{i \neq j} q_{ji}. \quad (3.3)$$

These conditions can be written compactly as

$$\boldsymbol{\pi} Q = 0 \quad \text{subject to} \quad \boldsymbol{\pi} \mathbf{e} = 1 \quad (3.4)$$

where \mathbf{e} is a commensurate column vector of ones. Thus, for the three-state single channel model (Eq. 3.1), $\pi_C + \pi_O + \pi_I = 1$ and

$$\pi_O = z_O/D, \quad \pi_C = z_C/D, \quad \pi_I = z_I/D \quad (3.5)$$

where $z_O = k_a^+ c_\infty^\eta k_b^-$, $z_C = k_a^- k_b^-$, $z_I = k_a^+ c_\infty^\eta k_b^+ (c_\infty + c_d)^\eta$, and $D = z_O + z_C + z_I$.

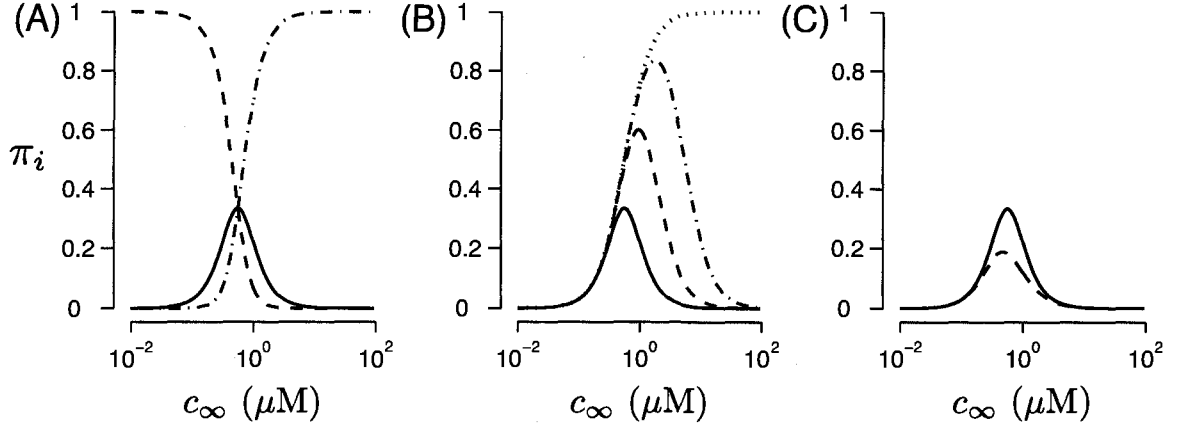


Figure 3.1: (A) The steady-state open ($\pi_{\mathcal{O}}$, *solid line*), closed ($\pi_{\mathcal{C}}$, *dashed line*), and inactivated ($\pi_{\mathcal{I}}$, *dashed-dotted line*) probabilities of the three-state single channel model as a function of the background $[\text{Ca}^{2+}]$ (c_{∞}) in the absence of elevated domain $[\text{Ca}^{2+}]$ ($c_d = 0 \mu\text{M}$, $\eta = 2$, $k_a^+ = 1.5 \mu\text{M}^{-\eta} \text{ms}^{-1}$, $k_b^+ = 0.015 \mu\text{M}^{-\eta} \text{ms}^{-1}$, $k_a^- = 0.5 \text{ms}^{-1}$, and $k_b^- = 0.005 \text{ms}^{-1}$). (B) $\pi_{\mathcal{O}}$ as a function of c_{∞} when the dissociation constant of Ca^{2+} inactivation is $K_b = 0.58$ (*solid line*), 1.73 (*dashed line*), 5.8 (*dashed-dotted line*) μM , and as $K_b \rightarrow \infty$ (*dotted line*). (C) $\pi_{\mathcal{O}}$ when the domain $[\text{Ca}^{2+}]$ is $c_d = 0$ (*solid line*) versus $c_d = 0.5 \mu\text{M}$ (*dashed line*).

If we assume that the channel is not conducting Ca^{2+} ($c_d = 0$), these expressions simplify to $z_{\mathcal{O}} = K_b^{\eta} c_{\infty}^{\eta}$, $z_{\mathcal{C}} = K_a^{\eta} K_b^{\eta}$, and $z_{\mathcal{I}} = c_{\infty}^{2\eta}$ where K_a and K_b are dissociation constants of Ca^{2+} activation and Ca^{2+} inactivation respectively given by $K_i^{\eta} = k_i^- / k_i^+$ where $i \in \{a, b\}$.

Figure 3.1A shows the steady-state closed ($\pi_{\mathcal{C}}$), open ($\pi_{\mathcal{O}}$), and inactivated ($\pi_{\mathcal{I}}$) probabilities as a function of the background $[\text{Ca}^{2+}]$ (c_{∞}) when $c_d = 0$. Notice that while $\pi_{\mathcal{C}}$ and $\pi_{\mathcal{I}}$ are monotonically decreasing and increasing functions of c_{∞} , respectively, the open probability $\pi_{\mathcal{O}}$ is ‘bell-shaped.’ That is, over a range of c_{∞} , $\pi_{\mathcal{O}}$ is elevated, but because the three-state channel model includes Ca^{2+} inactivation in addition to Ca^{2+} activation, $\pi_{\mathcal{O}} \rightarrow 0$ as $c_{\infty} \rightarrow \infty$. Figure 3.1B shows that the maximum $\pi_{\mathcal{O}}$ (and the range of c_{∞} leading to elevated $\pi_{\mathcal{O}}$) increases as the dissociation constant of Ca^{2+} inactivation (K_b) increases. As $K_b \rightarrow \infty$, Ca^{2+} inactivation no longer

occurs at physiological Ca^{2+} concentrations, and $\pi_{\mathcal{O}}$ is a monotonically increasing function of c_{∞} (*dotted line*). Figure 3.1C shows that when the domain $[\text{Ca}^{2+}]$ is increased from $c_d = 0$ to $0.5 \mu\text{M}$, the steady state open probability $\pi_{\mathcal{O}}$ decreases for all values of c_{∞} (compare *dashed* and *solid lines*).

3.3.2 Instantaneously coupled three-state channels

The Ca^{2+} release site model that is the focus of this chapter simulates N identical three-state channels defined by Eqs. 3.1 and 3.2 interacting via changes in local $[\text{Ca}^{2+}]$ under the assumption of “instantaneous mean-field coupling” [Nguyen et al., 2005, DeRemigio and Smith, 2005]. For example, when two identical three-state channels are coupled in this fashion, we write c_* to indicate the increase in $[\text{Ca}^{2+}]$ experienced by the Ca^{2+} regulatory site of channel 1 when channel 2 is open and vice versa. Because this parameter can be calculated from the source amplitude of open channels and the inter-channel distance using well-known equations for the buffered diffusion of Ca^{2+} [Nguyen et al., 2005, Smith et al., 2001, Naraghi and Neher, 1997], we refer to c_* as the ‘strength of Ca^{2+} coupling’ or the ‘coupling strength.’

Assuming the dwell times of the single channel model are long compared to the time scale of local $[\text{Ca}^{2+}]$ changes (i.e., effectively instantaneous interactions), the

state-transition diagram for two coupled three-state channels is given by

$$\begin{array}{ccccccc}
(2, 0, 0) & & & & & & \\
k_a^- & \Downarrow & 2k_a^+ c_\infty^\eta & & & & \\
& & & k_b^+ (c_\infty + c_d)^\eta & & & \\
(1, 1, 0) & & & = & & (1, 0, 1) & \\
& & & k_b^- & & & \\
2k_a^- & \Downarrow & k_a^+ (c_\infty + c_*)^\eta & & k_a^- & \Downarrow & k_a^+ c_\infty^\eta \\
& & & 2k_b^+ (c_\infty + c_* + c_d)^\eta & & & k_b^+ (c_\infty + c_d)^\eta \\
(0, 2, 0) & & & = & & (0, 1, 1) & = & (0, 0, 2) \\
& & & k_b^- & & & 2k_b^- & \\
& & & & & & & (3.6)
\end{array}$$

where the six distinguishable configurations—(2, 0, 0), (1, 1, 0), (1, 0, 1), (0, 2, 0), (0, 1, 1), and (0, 0, 2)—are denoted by three digit numbers indicating the number of channels in the closed, open, and inactivated states (N_C, N_O, N_I). The generator matrix Q corresponding to Eq. 3.6 is

$$Q = \begin{pmatrix} \diamond & 2k_a^+ c_\infty^\eta & 0 & 0 & 0 & 0 \\ k_a^- & \diamond & k_b^+ (c_\infty + c_d)^\eta & k_a^+ (c_\infty + c_*)^\eta & 0 & 0 \\ 0 & k_b^- & \diamond & 0 & k_a^+ c_\infty^\eta & 0 \\ 0 & 2k_a^- & 0 & \diamond & 2k_b^+ (c_\infty + c_* + c_d)^\eta & 0 \\ 0 & 0 & k_a^- & k_b^- & \diamond & k_b^+ (c_\infty + c_d)^\eta \\ 0 & 0 & 0 & 0 & 2k_b^- & \diamond \end{pmatrix} \quad (3.7)$$

where the diagonal elements (\diamond) are selected to ensure the rows sum to zero. Note that when a channel makes a $\mathcal{C} \rightarrow \mathcal{O}$ transition while the other channel is open, the Ca^{2+} coupling strength (c_*) is added to the background [Ca^{2+}] (c_∞) and this sum is used in a transition rate. Similarly, when a channel makes $\mathcal{O} \rightarrow \mathcal{I}$ transitions, the domain [Ca^{2+}] (c_d) is used, and c_* may or may not be added depending on the state of the other channel. The factors of 2 in Eq. 3.6 and 3.7 are combinatorial coefficients; for example, $Q[(2, 0, 0), (1, 1, 0)] = 2k_a^+ c_\infty^\eta$ because the $(2, 0, 0) \rightarrow (1, 1, 0)$ transition occurs when either one of the two channels makes a $\mathcal{C} \rightarrow \mathcal{O}$ state change.

Equations similar to 3.6 and 3.7 can be written to construct a Ca^{2+} release site model that includes an arbitrary number N of stochastically gating three-state channels. Such a model has $(N + 2)(N + 1)/2$ configurations that may be enumerated anti-lexicographically as

$$(N, 0, 0), (N - 1, 1, 0), \dots, (0, 1, N - 1), (0, 0, N) \quad (3.8)$$

where each configuration takes the form (N_C, N_O, N_I) where $0 \leq N_C \leq N$, $0 \leq N_O \leq N$, $0 \leq N_I \leq N$, and $N_C + N_O + N_I = N$. Consistent with prior work investigating the validity of different formulations of mean-field coupling, we assume the local $[\text{Ca}^{2+}]$ experienced by each channel is given by $c_\infty + N_O c_*$ when closed (state \mathcal{C} or \mathcal{I}) and $c_\infty + c_d + (N_O - 1)c_*$ when open (state \mathcal{O}) That is, we couple the channels in a manner that maintains a distinction between each channel's substantial influence on its own stochastic gating (c_d) and the collective contribution of elevated $[\text{Ca}^{2+}]$ from neighboring channels (which is proportional to c_*) [Nguyen et al., 2005, DeRemigio and Smith, 2005]. For a release site composed of N channels, the nonnegative elements of a generator matrix analogous to Eq. 3.7 are thus given by

$$Q[(N_C, N_O, N_I), (N_C - 1, N_O + 1, N_I)] = N_C k_a^+ (c_\infty + N_O c_*)^\eta \quad (3.9a)$$

$$Q[(N_C, N_O, N_I), (N_C + 1, N_O - 1, N_I)] = N_O k_a^- \quad (3.9b)$$

$$Q[(N_C, N_O, N_I), (N_C, N_O - 1, N_I + 1)] = N_O k_b^+ (c_\infty + c_d + (N_O - 1)c_*)^\eta \quad (3.9c)$$

$$Q[(N_C, N_O, N_I), (N_C, N_O + 1, N_I - 1)] = N_I k_b^- \quad (3.9d)$$

where it is understood that the origin and destination configurations of the release site must both be valid, i.e., they must both occur in Eq. 3.8. For example, Eq. 3.9a corresponds to a valid release site configuration change when $1 \leq N_C \leq N$, $0 \leq$

$N_{\mathcal{O}} \leq N - 1$, and $N_{\mathcal{I}} = N - N_{\mathcal{C}} - N_{\mathcal{O}}$. When Eqs. 3.9b–3.9d are interpreted in an analogous manner, Eq. 3.9 defines a square matrix of size $(N + 2)(N + 1)/2$ that is the Q matrix for a Ca^{2+} release site model within the scope of this study. Note that model includes 9 parameters: the single channel kinetic parameters (k_a^+ , k_a^- , k_b^+ , k_b^-), the cooperativity of Ca^{2+} binding (η), the background $[\text{Ca}^{2+}]$ (c_∞), the domain $[\text{Ca}^{2+}]$ (c_d), the coupling strength (c_*), and the number of channels at the release site (N). Simulations are performed using Gillespie’s algorithm (see Section 4.2), a numerical method with no intrinsic time step [Gillespie, 1976, Smith, 2002, Nguyen et al., 2005].

3.4 Results

3.4.1 Calcium release site models with low affinity calcium inactivation exhibit stochastic calcium excitability

Using the model formalism described in Section 3.3, Fig. 3.2A shows a Ca^{2+} release site simulation with 20 three-state channels. The number of open ($N_{\mathcal{O}}$, *black line*) and inactivated ($N_{\mathcal{I}}$, *red line*) channels at the release site are shown as functions of time, and the number of closed channels is given by $N_{\mathcal{C}} = N - N_{\mathcal{O}} - N_{\mathcal{I}}$. For significant periods of time few channels are open ($N_{\mathcal{O}} < 5$), but occasionally a large number of channels open simultaneously ($N_{\mathcal{O}}$ approaches 20). This dynamical behavior is referred to here as “stochastic Ca^{2+} excitability” and is reminiscent of Ca^{2+} puffs and sparks.

While the *red line* in Fig. 3.2A shows that some channels make $\mathcal{O} \rightarrow \mathcal{I}$ transitions during these puff/spark events, the dissociation constant Ca^{2+} inactivation ($K_b = k_b^-/k_b^+ = 5.8 \mu\text{M}$) is sufficiently high—i.e., the affinity Ca^{2+} inactivation is sufficiently low—to preclude the accumulation of channels in the inactivated state

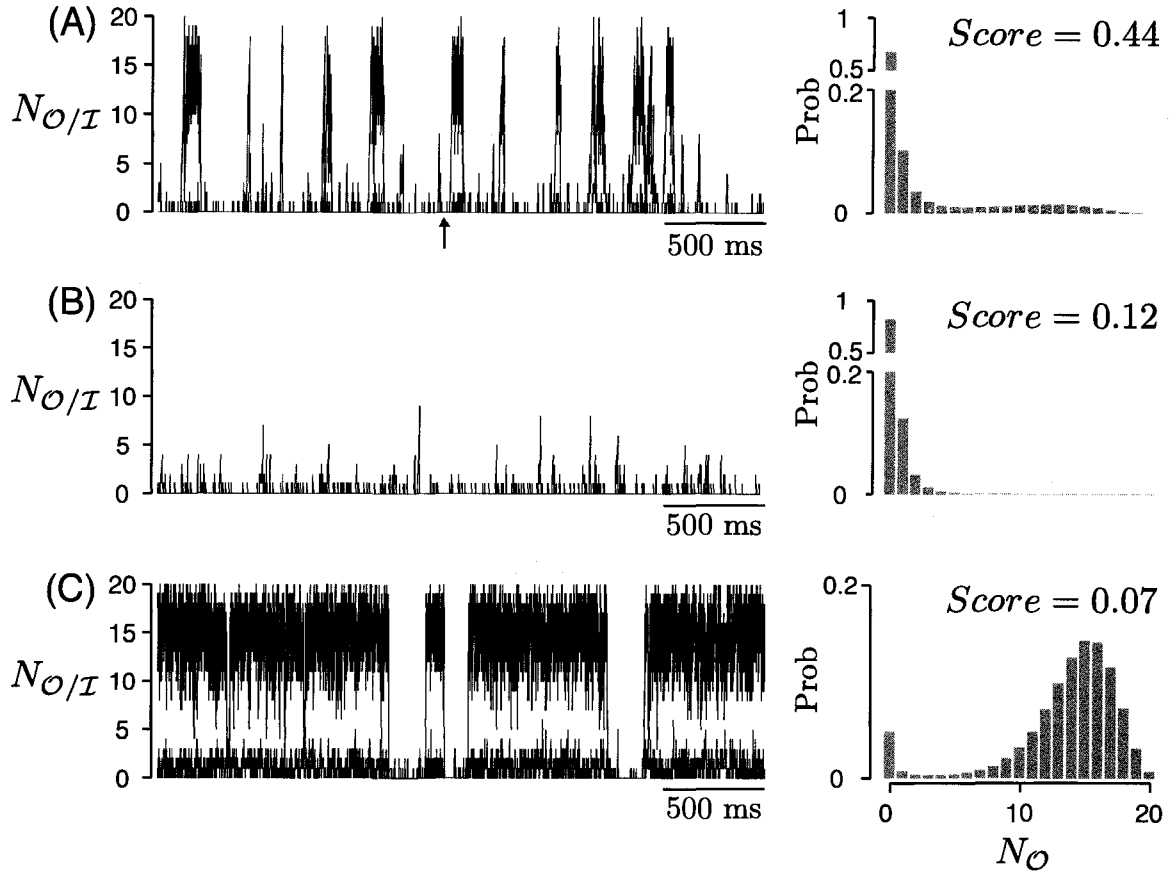


Figure 3.2: (A) Ca^{2+} release site simulation with 20 three-state channels exhibits stochastic Ca^{2+} excitability reminiscent of puffs and sparks. The number of open ($N_{\mathcal{O}}$, black line) and inactivated ($N_{\mathcal{I}}$, red line) channels are plotted as a function of time. The dissociation constant Ca^{2+} inactivation is sufficiently high to preclude the accumulation of channels in the inactivated state ($N_{\mathcal{I}} < 5$, see text). The right panel shows the probability distribution of the number of open channels ($N_{\mathcal{O}}$) at the release site and the puff/spark *Score* defined in Eq. 2.19. Parameters: $k_a^+ = 1.5 \mu\text{M}^{-\eta} \text{ms}^{-1}$, $k_b^+ = 0.015 \mu\text{M}^{-\eta} \text{ms}^{-1}$, $k_a^- = 0.5 \text{ms}^{-1}$, $k_b^- = 0.5 \text{ms}^{-1}$, $c_\infty = 0.05 \mu\text{M}$, $c_d = 0.5 \mu\text{M}$, $c_* = 0.06 \mu\text{M}$, and $\eta = 2$. (B,C) Puff/sparks are eliminated when the Ca^{2+} coupling strength is decreased to $c_* = 0.045 \mu\text{M}$ (B) or increased to $c_* = 0.075 \mu\text{M}$ (C).

($N_{\mathcal{I}} < 5$). Because direct allosteric coupling between neighboring intracellular channels and depletion of luminal Ca^{2+} are not included in the Ca^{2+} release site model, and there is no significant negative feedback due to Ca^{2+} -dependent inactivation of channels, we conclude that puff/spark termination in Fig. 3.2A is primarily due to

stochastic attrition, that is, the coincident de-activation of all channels at the release site [Stern, 1992b, Stern and Cheng, 2004, DeRemigio and Smith, 2005].

Figure 3.2B and C show that the stochastic Ca^{2+} excitability observed in Fig. 3.2A is sensitive to the strength of Ca^{2+} coupling at the simulated release site. When the coupling strength is reduced from $c_* = 0.06 \mu\text{M}$ in Fig. 3.2A to $c_* = 0.045 \mu\text{M}$ in Fig. 3.2B, Ca^{2+} puff/sparks fail to initiate. When the coupling strength is increased to $c_* = 0.075 \mu\text{M}$ in Fig. 3.2C, puff/sparks are less likely to terminate via stochastic attrition and the majority of channels at the release site are open ($N_{\mathcal{O}} > 10$) for unrealistically long periods.

The *gray histograms* in Fig. 3.2 show the probability distribution of the number of open channels ($N_{\mathcal{O}}$) for these three Ca^{2+} release site simulations (the distributions are directly calculated from the Q matrix as described Section 4.3). Note that the release site simulation exhibiting robust stochastic Ca^{2+} excitability (Fig. 3.2A) leads to a distribution in which the number of open channels has low expectation ($\text{E}[N_{\mathcal{O}}]$) but high variance ($\text{Var}[N_{\mathcal{O}}]$). This suggests the index of dispersion of the fraction of open channels ($f_{\mathcal{O}} = N_{\mathcal{O}}/N$) defined by

$$\text{Score} = \frac{\text{Var}[f_{\mathcal{O}}]}{\text{E}[f_{\mathcal{O}}]} = \frac{1}{N} \frac{\text{Var}[N_{\mathcal{O}}]}{\text{E}[N_{\mathcal{O}}]} \quad (3.10)$$

as a response measure to indicate the presence or absence of stochastic Ca^{2+} excitability in Monte Carlo simulations [Nguyen et al., 2005]. The *Score* takes values between 0 and 1 with values greater than approximately 0.25 indicating puff/sparks. For example, the simulation shown in Fig. 3.2A has a high *Score* of 0.44, while the simulations shown in Fig. 3.2B and C have low *Scores* of 0.12 and 0.07, respectively, because $\text{Var}[f_{\mathcal{O}}]$ is too low in B and $\text{E}[f_{\mathcal{O}}]$ is too high in C.

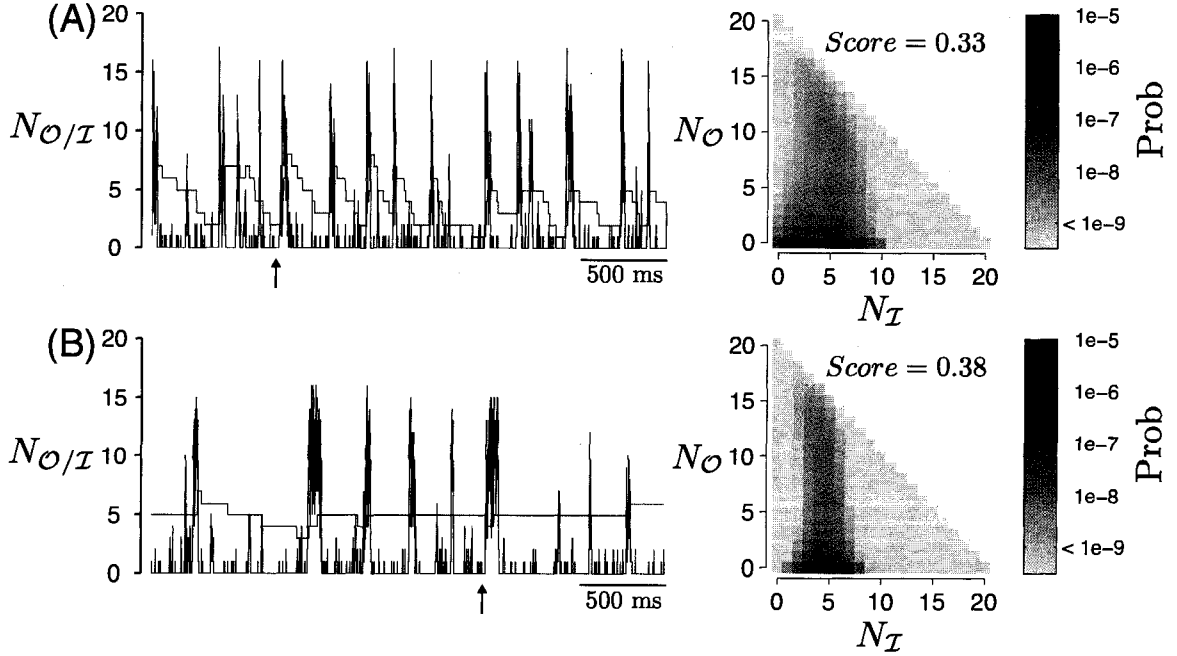


Figure 3.3: High affinity Ca^{2+} inactivation can facilitate puff/spark termination in two distinct ways. (A) Ca^{2+} release site simulation with 20 three-state channels showing puff/spark termination facilitated by the recruitment of inactivated channels during puff/spark events ($k_b^+ = 0.015 \mu\text{M}^{-\eta} \text{ms}^{-1}$, $k_b^- = 0.0087 \text{ms}^{-1}$, $K_b = 0.58 \mu\text{M}$). Other parameters as in Fig. 3.2C. The left panel shows the number of open (N_O , *black line*) and inactivated (N_I , *red line*) channels. The right panel shows the steady-state probability of the 231 release site configurations (N_C, N_O, N_I), where it is understood that $N_C = 20 - N_O - N_I$. (B) When the kinetics of Ca^{2+} inactivation is reduced ten fold ($k_b^+ = 0.0015 \mu\text{M}^{-\eta} \text{ms}^{-1}$ and $k_b^- = 0.00087 \text{ms}^{-1}$) without changing the affinity of Ca^{2+} inactivation or the coupling strength, the number of inactivated channels (N_I) is nearly constant and puff/sparks terminate without additional recruitment if inactivated channels.

3.4.2 High affinity calcium inactivation facilitates puff termination

While Fig. 3.2 demonstrated that Ca^{2+} release site simulations with low affinity Ca^{2+} inactivation may exhibit puff/sparks that terminate primarily due to stochastic attrition, Fig. 3.3 shows that high affinity Ca^{2+} inactivation facilitates puff/spark termination when stochastic attrition alone is insufficient to allow robust termination.

Recall that in Fig. 3.2C the coupling strength was sufficiently strong that puff/sparks did not often terminate via stochastic attrition and this resulted in a low *Score* of 0.07. When this simulation is repeated in Fig. 3.3A using channels with high affinity Ca^{2+} inactivation—that is, K_b is reduced from 5.8 to 0.58 μM —robust puff/sparks are now observed (*Score* = 0.35). In this case, the number inactivated channels (N_I) increases during each puff/spark event, and between puff/spark events the number of inactivated channels decreases. This accumulation of inactivated channels throughout the duration of each puff/spark event appears to contribute to puff/spark termination, because the number of inactivated channels is usually greater than average ($N_I > E[N_I] = 4.3$) at the end of puff/spark events. The range of the fluctuations in the number of inactivated channels ($2 \leq N_I \leq 8$) can be observed in the stochastic trajectories as well as the joint probability distribution for (N_I, N_O) shown in the right panel of Fig. 3.3A.

Fig. 3.3B demonstrates that high affinity Ca^{2+} inactivation ($K_b = 0.58 \mu\text{M}$) may facilitate puff/spark termination even when the kinetics of inactivation are ten-fold slower than that used in Fig. 3.3A (both k_b^+ and k_b^- are reduced so that K_b is unchanged). Interestingly, puff/spark termination in Fig. 3.3B does not appear to be due to the recruitment of inactivated channels throughout the duration of puff/spark events, because the fraction of inactivated channels is relatively constant (*red line*). Although the number of inactivated channels does not increase during puff/spark events, the ‘sequestering’ of approximately 5 channels into the inactivated state results in a reduced number of de-inactivated channels (states \mathcal{O} and \mathcal{C}) that participate in each puff/spark event, thereby facilitating termination via stochastic attrition (i.e., nearly simultaneous $\mathcal{O} \rightarrow \mathcal{C}$ transitions).

Comparison of Fig. 3.3A and B suggests that high affinity Ca^{2+} inactivation may facilitate puff/spark termination in two distinct ways depending on the rate of Ca^{2+}

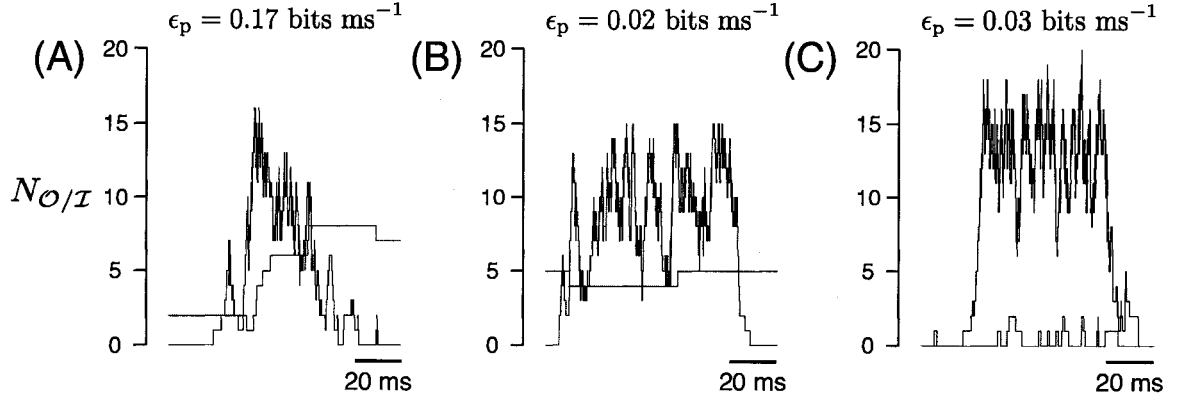


Figure 3.4: The entropy production rate (ϵ_p) and representative puff/sparks from Ca^{2+} release site simulations shown in Fig. 3.3A (A), Fig. 3.3B (B), and Fig. 3.2A (C). (A) An elevated *Score* and ϵ_p indicates that puff/spark termination is facilitated by the accumulation of channels in the inactivated state during puff/spark events. (B and C) An elevated *Score* and a low ϵ_p indicates that puff termination occurs due to stochastic attrition although a fraction of channels may be sequestered in the inactivated state (B) facilitating stochastic attrition. Each panel expands 100 ms of the corresponding simulation showing detail of the puff/sparks beginning at *arrows*.

inactivation. While the expected number of inactivated channels is similar in both simulations ($E[N_I] = 4.3$ and 4.7 , respectively), the variance of the number of inactivated channels is smaller when high affinity Ca^{2+} inactivation is slow ($\text{Var}[N_I] = 3.7$ in A and 1.2 in B). The robust puff/sparks observed in Fig. 3.3B suggest that Ca^{2+} inactivation may be an important negative feedback mechanism even when its time constant is much greater than the duration of puffs and sparks.

3.4.3 Thermodynamically irreversible and nearly reversible puff and spark dynamics

Fig. 3.3 showed that Ca^{2+} inactivation may facilitate puff/spark termination in two distinct manners depending on the kinetics of Ca^{2+} inactivation. To clarify the difference between these two types of stochastic Ca^{2+} excitability, Fig. 3.4A expands a

puff/spark event from Fig. 3.3A where puff/spark termination is facilitated by the recruitment of inactivated channels. During this puff/spark, the number of open channels ($N_{\mathcal{O}}$) first increases rapidly and then slowly declines as the number of inactivated channels increases from $N_{\mathcal{I}} = 2$ to 8. This asymmetry in the trajectories for $N_{\mathcal{O}}$ and $N_{\mathcal{I}}$ suggests that the dynamics of this Ca^{2+} release site model is time-irreversible, that is, the stationary probability distribution $\boldsymbol{\pi}$ of the Markov chain model $Q = (q_{ij})$ satisfies global balance (Eqs. 3.3–3.4) but does not satisfy detailed balance,

$$\pi_i q_{ij} = \pi_j q_{ji} \quad \text{for all } i \neq j. \quad (3.11)$$

This can be confirmed by calculating the thermodynamic entropy production rate [Jiang et al., 2004],

$$\epsilon_p = \frac{1}{2} \sum_{i \neq j} (\pi_i q_{ij} - \pi_j q_{ji}) \log_2 \left(\frac{\pi_i q_{ij}}{\pi_j q_{ji}} \right), \quad (3.12)$$

a response measure that quantifies the extent to which detailed balance is not satisfied. Note that the entropy production rate is a non-negative quantity and $\epsilon_p = 0$ indicates time-reversibility. For the puff/sparks of Figs. 3.3A and 3.4A, the entropy production rate is $\epsilon_p = 0.17$ bits ms^{-1} .

Fig. 3.4B expands a puff/spark of Fig. 3.3B for which a relatively constant number of inactivated channels potentiates puff/spark termination via stochastic attrition. In contrast to Fig. 3.4A, the shape of the trajectories for $N_{\mathcal{O}}$ and $N_{\mathcal{I}}$ do not clearly indicate the Markov chain is time-irreversible. Indeed, the entropy production rate for Figs. 3.3B and 3.4B is $\epsilon_p = 0.02$ bits ms^{-1} , over 8-fold smaller than Figs. 3.3A and 3.4A.

Figure 3.4A and B suggest that the entropy production rate ϵ_p can be used in

combination with the *Score* to determine if Markov chain models of Ca^{2+} release sites exhibit puff/sparks that terminate due to the recruitment of inactivated channels (resulting in relatively high ϵ_p) or via stochastic attrition (resulting in relatively low ϵ_p). To give another example, Fig. 3.4C expands a puff/spark of Fig. 3.2A where Ca^{2+} inactivation was low affinity and the number of inactivated channels was consistently small ($N_I < 3$). In this case, the low entropy production rate of $\epsilon_p = 0.03$ bits ms^{-1} for Figs. 3.2A and 3.4C indicates nearly time-reversible dynamics, consistent with puff/sparks that terminate via stochastic attrition without the recruitment of inactivated channels.

3.4.4 Calcium inactivation and the sensitivity of puffs and sparks to variations in the strength of calcium coupling

While Fig. 3.3 showed that high affinity Ca^{2+} inactivation can contribute to the dynamics of puff/spark termination in two distinct manners, Fig. 3.4 showed how the entropy production rate (ϵ_p) can be used to distinguish between these two types of stochastic Ca^{2+} excitability. To further clarify the role of Ca^{2+} inactivation in puff/spark dynamics, Fig. 3.5 shows the *Score* and entropy production rate ϵ_p for a release site composed of 20 three-state channels as a function of the strength of Ca^{2+} coupling (c_*) and the dissociation constant of Ca^{2+} inactivation (K_b) for three different rates of Ca^{2+} inactivation (k_b^+). For clarity, the results are plotted as a function of the relative dissociation constant for Ca^{2+} inactivation compared to Ca^{2+} activation ($K_{\text{rel}} = K_b/K_a$) and the corresponding relative inactivation rate ($k_{\text{rel}}^+ = k_b^+/k_a^+$). Note that the *Score* is shown only when robust puff/sparks are observed ($\text{Score} > 0.25$). The *dashed lines* are isoclines corresponding to an entropy production rate of $\epsilon_p = 0.1$ bits ms^{-1} (a value that discriminates between the low and high values observed in

Fig. 3.4), while the *arrows* indicate the direction of increasing ϵ_p .

When the rate of Ca^{2+} inactivation is ten-fold slower than Ca^{2+} activation ($k_{\text{rel}}^+ = 0.1$ in Fig. 3.5A), puff/sparks are observed when the affinity of Ca^{2+} inactivation is sufficiently low ($K_{\text{rel}} > 2$) and the Ca^{2+} coupling strength (c_*) is in a narrow range. Conversely, when the rate of inactivation is 100-fold slower than activation ($k_{\text{rel}}^+ = 0.01$ in Fig. 3.5B), puff/sparks are seen over a broad range of K_{rel} and c_* , and for some values of the relative dissociation constant for Ca^{2+} inactivation (K_{rel}) puff/sparks become significantly less sensitive to the Ca^{2+} coupling strength (c_*). Interestingly, in Fig. 3.5B most of the region of elevated *Score* has an elevated entropy production rate ($\epsilon_p > 0.1$ bits ms^{-1}), indicating that these puff/sparks are time-irreversible. For example, the *cross* in Fig. 3.5B corresponds to parameters used in Fig. 3.3A where puff/spark termination is facilitated by an increase in the number of inactivated channels during puff/spark events.

When the rate of Ca^{2+} inactivation is 1000-fold slower than Ca^{2+} activation ($k_{\text{rel}}^+ = 0.001$ in Fig. 3.5C), puff/sparks are also observed over a large region of the (c_* , K_{rel})-plane. However, most of the region of elevated *Score* has a low entropy production rate ($\epsilon_p < 0.1$ bits ms^{-1}), indicating that these puff/sparks are nearly time-reversible. For example, the *cross* in Fig. 3.5C corresponds to parameters used in Fig. 3.3C where puff/sparks occur on a constant background of inactivated channels.

All three panels of Fig. 3.5 show that when the affinity of Ca^{2+} inactivation is sufficiently low, puff/spark dynamics are nearly identical to corresponding calculations using a two-state model that lacks the inactivated state ($K_{\text{rel}} = \infty$). For example, the *asterisks* in Fig. 3.3B at $K_{\text{rel}} = 10$ correspond to the three simulations in Fig. 3.2 where low affinity Ca^{2+} inactivation is largely inconsequential to the dynamics of Ca^{2+} puff/sparks.

Taken as a whole, Fig. 3.5 demonstrates that high affinity Ca^{2+} inactivation can

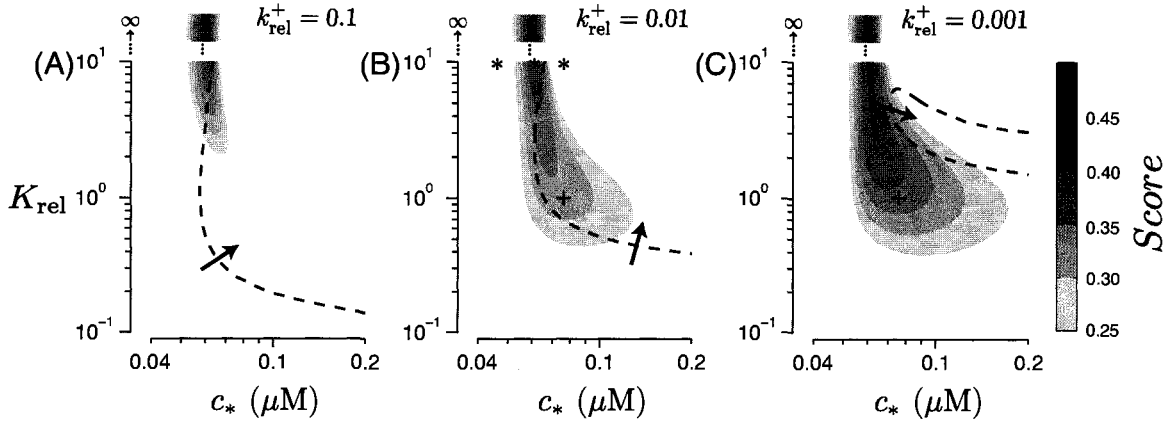


Figure 3.5: The Ca^{2+} puff/spark *Score* of Ca^{2+} release site simulations with 20 three-state channels as a function of the Ca^{2+} coupling strength (c_*) and the relative dissociation constant of Ca^{2+} inactivation ($K_{\text{rel}} = K_b/K_a$) for three values of the relative Ca^{2+} inactivation rate (A, $k_{\text{rel}}^+ = k_b^+/k_a^+ = 0.1$; B, $k_{\text{rel}}^+ = 0.01$; C, $k_{\text{rel}}^+ = 0.001$). Other parameters as in Fig. 3.2. For clarity, the *Score* is shown only when robust puff/sparks are observed ($\text{Score} > 0.25$). *Dashed lines* are isoclines where $\epsilon_p = 0.1$ bits ms^{-1} and *arrows* indicate the direction of increasing ϵ_p . The three *asterisks* in (B) show parameters used in Fig. 3.2A–C. Crosses in (B) and (C) show parameters used in Fig. 3.3A and B, respectively.

reduce the sensitivity of puff/sparks to variation in the Ca^{2+} coupling strength (c_*) as long as the rate of inactivation is sufficiently slow (panels B and C). While excessively fast Ca^{2+} inactivation can preclude puffs and sparks (Fig. 3.5A), moderately fast Ca^{2+} inactivation often leads to time-irreversible puff/sparks whose termination is facilitated by the recruitment of inactivated channels throughout the duration of the puff/spark event (Fig. 3.5B). However, even slow Ca^{2+} inactivation can be an important negative feedback mechanism leading to nearly time-reversible puff/sparks that terminate without pulsatile recruitment of inactivated channels during each puff/spark (Fig. 3.5B). In both cases, the presence of high affinity Ca^{2+} inactivation greatly extends the range of Ca^{2+} coupling strengths that leads to robust puff/sparks and elevated *Score* (Fig. 3.5B and C).

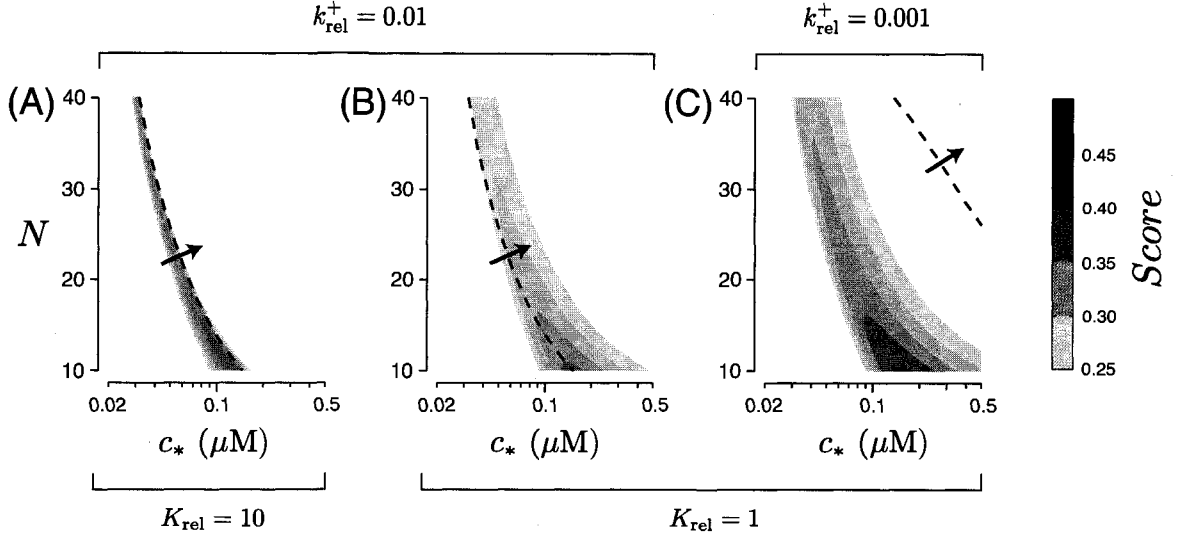


Figure 3.6: The Ca^{2+} puff/spark *Score* of Ca^{2+} release site simulations as a function of the Ca^{2+} coupling strength (c_*) and the number of three-state channels at the release site (N) for several values of the relative dissociation constant of Ca^{2+} inactivation (A, $K_{\text{rel}} = K_b/K_a = 10$; B and C, $K_{\text{rel}} = 1$) and the relative Ca^{2+} inactivation rate (A and B, $k_{\text{rel}}^+ = k_b^+/k_a^+ = 0.01$; C, $k_{\text{rel}}^+ = 0.001$). Other parameters as in Fig. 3.2. As in Fig. 3.5, the *Score* is shown only when robust puff/sparks are observed (*Score* > 0.25), *dashed lines* are isoclines where $\epsilon_p = 0.1$ bits ms^{-1} , and *arrows* indicate the direction of increasing ϵ_p .

3.4.5 Calcium inactivation and the sensitivity of puffs and sparks to the number of channels at release sites

Figure 3.6 shows the puff/spark *Score* and entropy production rate ϵ_p as a function of the strength of Ca^{2+} coupling (c_*) and the number of channels at a release site (N). As in Fig. 3.5, the *Score* is shown only when robust puff/sparks are observed (*Score* > 0.25), *dashed lines* indicate $\epsilon_p = 0.1$ bits ms^{-1} , and *arrows* point in the direction of increasing ϵ_p .

Figure 3.6A shows that when the dissociation constant for Ca^{2+} inactivation is ten times larger than that of Ca^{2+} activation ($K_{\text{rel}} = 10$) and the relative rate of inactivation is moderate ($k_{\text{rel}}^+ = 0.01$), puff/sparks are observed over a range of coupling

strengths (c_*) for any fixed number of channels (N). Because Ca^{2+} inactivation is low affinity (high K_{rel}), most of the region of elevated *Score* has a low entropy production rate ($\epsilon_p < 0.1$ bits ms^{-1}) indicating nearly time-reversible puff/sparks that terminate via stochastic attrition. As N increases, puff/sparks are observed for an increasingly narrow range of c_* . The optimal coupling strength—the value of c_* that results in the highest *Score*—is a decreasing function of N .

When the affinity of Ca^{2+} inactivation is equal to that of Ca^{2+} activation ($K_{\text{rel}} = 1$ in Fig. 3.6B), puff/sparks are observed over a broader range of c_* for all N (cf. Fig. 3.6A). Because Ca^{2+} inactivation is high affinity (low K_{rel}), puff/sparks exhibit an elevated entropy production rate ($\epsilon_p > 0.1$ bits ms^{-1}) indicating time-irreversible puff/sparks that terminate via recruitment of inactivated channels.

Figure 3.6C repeats the parameter study of Fig. 3.6B using same affinity for Ca^{2+} inactivation but slower kinetics ($K_{\text{rel}} = 1$ and $k_{\text{rel}}^+ = 0.001$). This high affinity (but slow) Ca^{2+} inactivation dramatically increases the range of coupling strengths (c_*) that lead to puff/sparks regardless of the number of channels at the release site (N). However, in this case the region of elevated *Score* has a low entropy production rate ($\epsilon_p < 0.1$ bits ms^{-1}) indicating nearly time-reversible puff/sparks that terminate without pulsatile recruitment of inactivated channels.

Because it may be counter-intuitive that slow Ca^{2+} inactivation can dramatically increase the range of c_* and N leading to robust puff/sparks, Fig. 3.7A shows simulations of release sites composed of $N = 20, 30$ or 40 channels with fixed coupling strength ($c_* = 0.07 \mu\text{M}$) and slow, high-affinity Ca^{2+} inactivation ($K_{\text{rel}} = 1$, $k_{\text{rel}}^+ = 0.001$ as in Fig. 3.6C). Notice that as the number of channels (N) at the release site increases, an increasing fraction of channels are sequestered in the inactivated state during simulations leaving a relatively constant number of de-inactivated channels (\mathcal{O} or \mathcal{C}) to participate in puff/sparks. Consequently, the puff/sparks of Fig. 3.7A

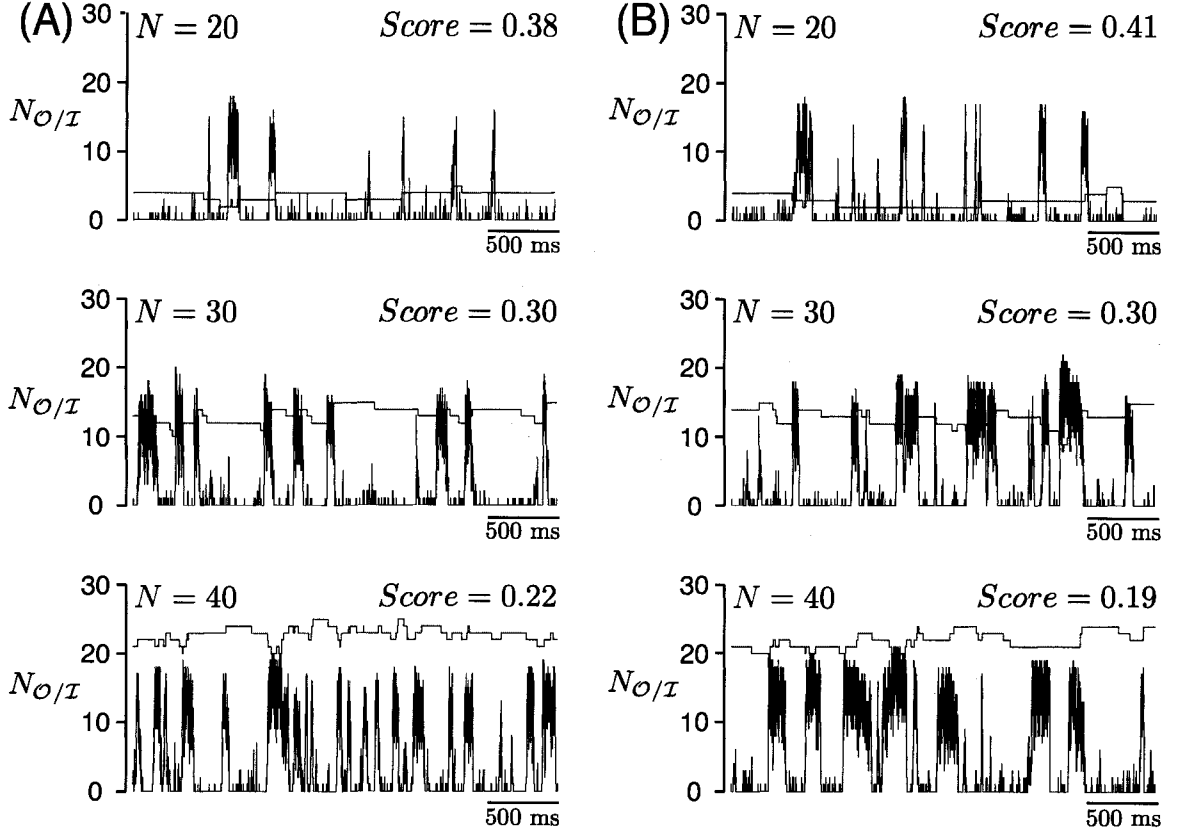


Figure 3.7: (A) Ca^{2+} release site simulations using $N = 20, 30,$ or 40 three-state channels with Ca^{2+} -dependent inactivation (Eq. 3.1). The number of open ($N_{\mathcal{O}}$, *black line*) and inactivated ($N_{\mathcal{I}}$, *red line*) channels are shown as a function of time. Parameters as in Fig. 3.2 except $c_* = 0.07 \mu\text{M}$, $K_{\text{rel}} = 1$ and $k_{\text{rel}}^+ = 0.001$ (B) Release site simulations similar to (A) except the single channel model used includes Ca^{2+} -independent (i.e., activity-dependent) inactivation (Eq. 3.13). Parameters as in (A) except $\hat{k}_b^+ = 0.0015 \text{ ms}^{-1}$ and $\hat{k}_b^- = 0.0005 \text{ ms}^{-1}$.

exhibit stereotyped amplitudes of $N_{\mathcal{O}} \approx 20$ regardless of the number of channels in the release site simulations (N). Interestingly, this stereotyped amplitude of puff/sparks is a decreasing function of c_* (not shown).

Figure 3.7B repeats the puff/spark simulation results of Fig. 3.7A using a single channel model that is identical to Eq. 3.1 except that the slow inactivation (the

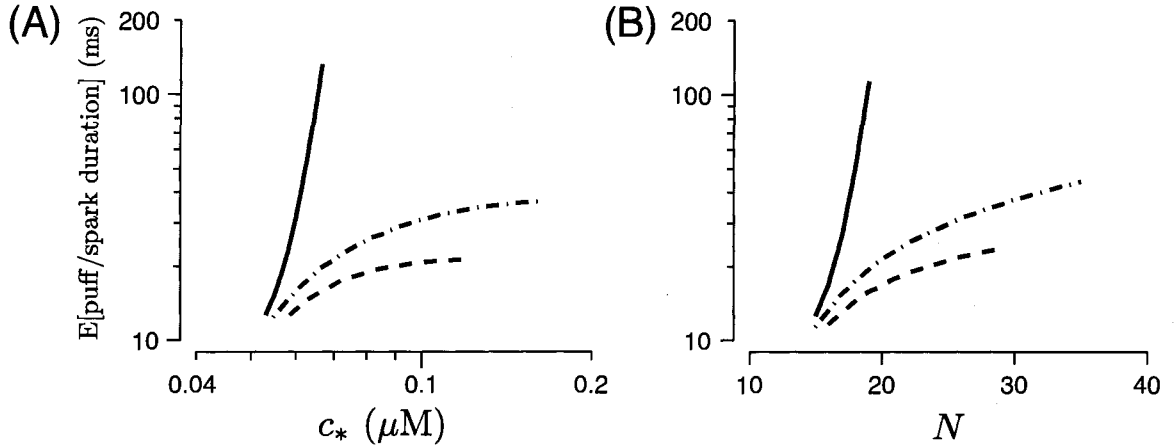
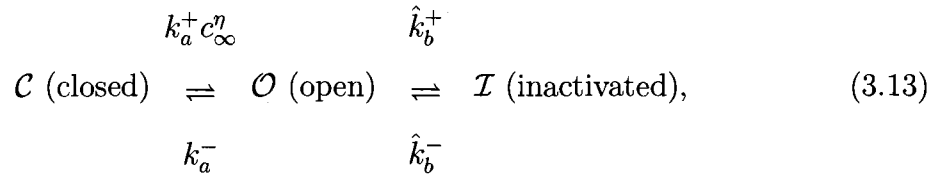


Figure 3.8: The mean duration of simulated puff/sparks plotted against (A) the Ca^{2+} coupling strength c_* and (B) the release site size N when Ca^{2+} inactivation is low affinity and moderately fast (*solid line*, $K_{\text{rel}} = 10, k_{\text{rel}}^+ = 0.01$), high affinity and moderately fast, (*dashed line*, $K_{\text{rel}} = 1, k_{\text{rel}}^+ = 0.01$), and high affinity and slow (*dashed-dotted line*, $K_{\text{rel}} = 1, k_{\text{rel}}^+ = 0.001$). $N = 20$ in (A) and $c_* = 0.7 \mu\text{M}$ in (B). Other parameters as in Fig. 3.2.

$\mathcal{O} \rightarrow \mathcal{I}$ transition) does not require Ca^{2+} binding, that is,



where \hat{k}_b^+ and \hat{k}_b^- are both transition rates with units of time^{-1} . Interestingly, the puff/sparks of Fig. 3.7B exhibit stereotyped amplitudes much like those of Fig. 3.7A, demonstrating that slow activity-dependent inactivation can also result in puff/sparks that are insensitive to variations of release site size (N).

3.4.6 Calcium inactivation and puff/spark duration

Using a variety of Ca^{2+} coupling strengths (c_*) and release site sizes (N), Fig. 3.8 shows how Ca^{2+} inactivation influences the mean duration of puff/sparks. In the context of the Markov chain model that is the focus of this paper, puff/spark duration is the random period of time between puff/spark initiation (when a release site makes a transition from $N_{\mathcal{O}} = 4 \rightarrow 5$ open channels) and termination (when all channels close via a $N_{\mathcal{O}} = 1 \rightarrow 0$ transition). Defining puff/spark initiation in this manner excludes small amplitude events (i.e., blips or quarks). The calculations are performed using matrix analytic formula that express the probability distribution (Eq. 4.9) and expected value (Eq. 4.10) of puff/spark duration as a function of the Q matrix for a Ca^{2+} release site model (see Section 4.4).

The *solid line* of Fig. 3.8A shows that when the affinity of Ca^{2+} inactivation is low ($K_{\text{rel}} = 10$) and the rate of Ca^{2+} inactivation is moderate ($k_{\text{rel}}^+ = 0.01$), the mean puff/spark duration of a 20-channel release site model is an increasing function of the coupling strength (c_*). Because the mean puff/spark duration is only calculated when $\text{Score} > 0.25$, the extent of the *solid line* indicates the range of coupling strengths that lead to robust puff/sparks. The *dashed line* of Fig. 3.8A shows that when the affinity of Ca^{2+} inactivation is high ($K_{\text{rel}} = 1$) and the rate of inactivation is moderate ($k_{\text{rel}}^+ = 0.01$), puff/spark duration is also an increasing function of c_* , but the rate of increase is significantly reduced compared to the low affinity case (cf. *solid line*). This reduced sensitivity of puff/spark duration to changes in the Ca^{2+} coupling strength (c_*) is also observed when Ca^{2+} inactivation is high affinity and the rate of inactivation is ten-fold slower ($k_{\text{rel}}^+ = 0.001$, *dashed-dotted line*).

Figure 3.8B shows that the mean puff/spark duration is also an increasing function of the number of channels at the release site (N). Similar to Fig. 3.8A, comparison

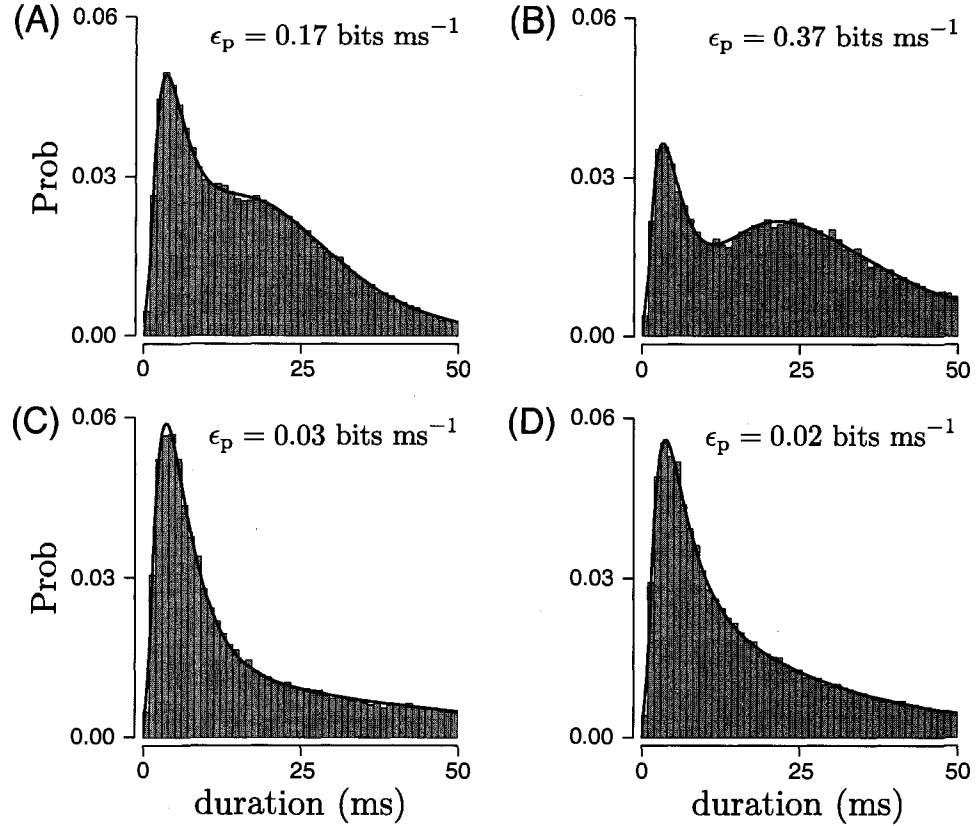


Figure 3.9: Probability distributions of puff/spark duration calculated using the matrix analytic formula in Section 4.4 (*solid lines*) and validated by Monte Carlo simulation (*gray histograms*) when Ca^{2+} inactivation is low affinity (C, $K_{\text{rel}} = 10$, $k_{\text{rel}}^+ = 0.01$, $c_* = 0.06 \mu\text{M}$) or high affinity (A, $K_{\text{rel}} = 1$, $k_{\text{rel}}^+ = 0.01$, $c_* = 0.075 \mu\text{M}$; B, $K_{\text{rel}} = 2$, $k_{\text{rel}}^+ = 0.01$, $c_* = 0.075 \mu\text{M}$; D, $K_{\text{rel}} = 1$, $k_{\text{rel}}^+ = 0.001$, $c_* = 0.075 \mu\text{M}$). Other parameters as in Fig. 3.2.

of the *solid* ($K_{\text{rel}} = 10$) and *broken* ($K_{\text{rel}} = 1$) *lines* shows that the sensitivity of puff/spark duration to changes in N is reduced when high-affinity Ca^{2+} inactivation is included in simulations, regardless of whether the rate of Ca^{2+} inactivation is moderate ($k_{\text{rel}}^+ = 0.01$, *dashed line*) or slow ($k_{\text{rel}}^+ = 0.001$, *dashed-dotted line*).

While Fig. 3.8 focused on how the mean puff/spark duration changes as a function of c_* and N , Fig. 3.9 shows how Ca^{2+} inactivation influences the shape of the probability distribution of puff/spark duration. The *solid lines* of Fig. 3.9 are calculated

using Eq. 4.9 in Chap. 4, and these results are validated by *gray histograms* estimated from Monte Carlo simulation.

Depending on model parameters, the probability distribution of puff/spark duration may be unimodal (Fig. 3.9C and D), bimodal (Fig. 3.9B), or ‘transitional,’ that is, a unimodal distribution that has more than two inflection points (Fig. 3.9A). Interestingly, the modalities of the puff/spark duration distributions shown in Fig. 3.9 are correlated with the entropy production rate (ϵ_p) of the corresponding puff/spark simulations. For instance, the transitional distribution of Fig. 3.9A corresponds to the time-irreversible puff/sparks of Fig. 3.3A that terminate due to the recruitment of inactivated channels during puff/spark events (high ϵ_p of 0.17 bits ms^{-1}). The bimodal distribution of Fig. 3.9B corresponds to another simulation with elevated entropy production rate and time-irreversible puff/sparks (not shown). On the other hand, the unimodal distributions of Fig. 3.9C and D correspond to the nearly time-reversible puff/sparks of Fig. 3.2A and Fig. 3.3B that terminate via stochastic attrition without the pulsatile recruitment of inactivated channels (low ϵ_p of 0.03 and 0.02 bits ms^{-1} , respectively).

To clarify the relationship between the shape of probability distributions of puff/spark duration and the entropy production rate, Fig. 3.10 repeats the parameter study of Fig. 3.5 while indicating whether the probability distribution of puff/spark duration is unimodal, bimodal, or transitional (see legend). When the rate of Ca^{2+} inactivation is ten-fold slower than Ca^{2+} activation ($k_{\text{rel}}^+ = 0.1$ in Fig. 3.10A), bimodal puff/spark duration distributions are not observed. On the other hand, when the rate of inactivation is 100-fold slower than activation ($k_{\text{rel}}^+ = 0.01$ in Fig. 3.5B), the vast majority of the (K_{rel,c_*}) -plane yielding robust puff/sparks ($\text{Score} > 0.25$) and an elevated entropy production rate ($\epsilon_p > 0.1$ bits ms^{-1}) results in bimodal probability distributions of puff/spark duration. Interestingly, the modality of puff/spark

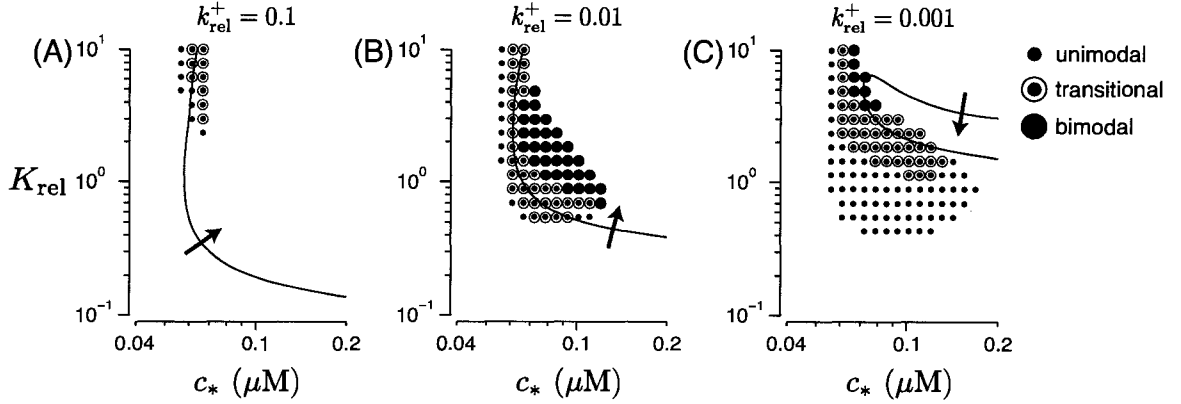


Figure 3.10: The shape of puff/spark duration probability distributions (unimodal, transitional, and bimodal as discussed in text) are plotted as a function of the Ca^{2+} coupling strength (c_*) and the relative dissociation constant of Ca^{2+} inactivation (K_{rel}) for several different values of the relative rate of Ca^{2+} inactivation (A, $k_{\text{rel}}^+ = 0.1$; B, $k_{\text{rel}}^+ = 0.01$; C, $k_{\text{rel}}^+ = 0.001$). *Solid lines* are isoclines with $\epsilon_p = 0.1$ bits ms^{-1} and *arrows* indicate the direction of increasing ϵ_p . Simulations involve 20 channels and other parameters as in Fig. 3.2.

duration distributions often changes from unimodal to transitional to bimodal with increasing Ca^{2+} coupling strength (c_*). When the rate of Ca^{2+} inactivation is 1000-fold slower than Ca^{2+} activation ($k_{\text{rel}}^+ = 0.001$ in Fig. 3.5C), the region with bimodal and transitional distributions becomes smaller, consistent with the contraction of the region with elevated ϵ_p .

The stacked histograms of Fig. 3.11 summarize the relationship between the the modality of puff/spark duration distributions and the entropy production rate (ϵ_p) of the corresponding puff/spark simulations. The histograms are constructed from a large number of 20-channel release site simulations where the relative dissociation constants of inactivation (K_{rel}), relative inactivation rates (k_{rel}^+), and coupling strengths (c_*) are independent random variables drawn from log-normal distributions spanning the ranges used in Fig. 3.10 (see legend). Note that the vast majority of unimodal distributions occur with a low entropy production rate ($\epsilon_p < 0.1$ bits ms^{-1}). Conversely,

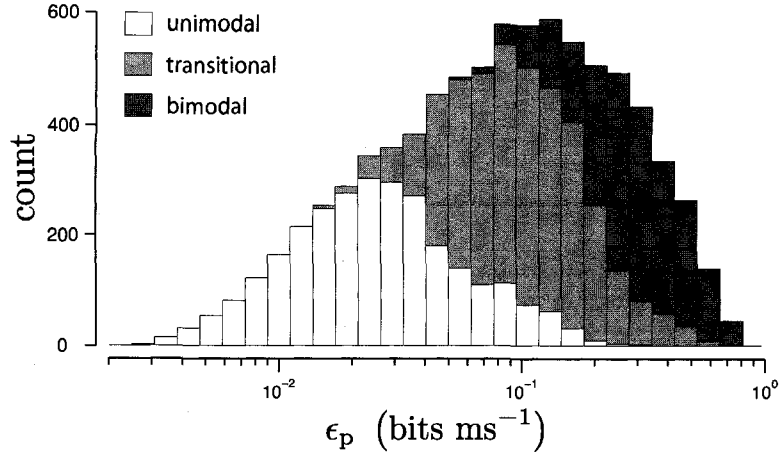


Figure 3.11: Stacked histograms show the relationship between the entropy production rate (ϵ_p) and the modality (unimodal, transitional, bimodal) of the probability distribution of puff/spark duration. The histograms are constructed from 50,000 release site simulations with 20 three-state channels, 9631 of which resulted in robust puff/sparks with $Score > 0.25$ (34% unimodal, 41% transitional, 25% bimodal). The relative dissociation constant of inactivation, relative inactivation rate, and coupling strength used in each simulation were independent random variables drawn from log-uniform distributions spanning the ranges shown in Fig. 3.10 ($0.1 \leq K_{rel} \leq 10$, $0.001 \leq k_{rel}^+ \leq 0.1$, $0.04 \leq c_* \leq 0.2 \mu\text{M}$). Other parameters as in Fig. 3.2.

the vast majority of bimodal distributions occur with an elevated entropy production rate ($\epsilon_p > 0.1$ bits ms^{-1}). While the modality of puff/spark duration distributions and entropy production rate are correlated in this manner, transitional distributions may result from both time-irreversible and nearly time-reversible puff/spark simulations (i.e., a wide range of entropy production rates).

3.5 Discussion

While there is a consensus that Ca^{2+} puffs and sparks arise due to the cooperative gating of RyRs or IP_3Rs clustered at Ca^{2+} release sites, the mechanisms that facilitate termination of these Ca^{2+} release events are not well understood. As dis-

cussed in the introduction, Ca^{2+} -dependent inactivation is one of several negative control mechanisms that may contribute to puff and spark termination. Other possibilities include Ca^{2+} -independent inactivation of channels (i.e., activity-dependent or ‘fateful’ inactivation), direct allosteric coupling promoting simultaneous closure of channels, depletion of luminal Ca^{2+} leading to cytosolic domain collapse, and stochastic attrition [Stern, 1992b, DeRemigio and Smith, 2005, Stern and Cheng, 2004, Fill, 2002, Sham et al., 1998, Groff and Smith, 2007a, Groff and Smith, 2007b]. Using minimal Ca^{2+} release site models composed of three-state channels that are both activated and inactivated by cytosolic Ca^{2+} , this paper clarifies how the dissociation constant and rate of Ca^{2+} inactivation may influence the stochastic dynamics of Ca^{2+} puffs and sparks.

3.5.1 Calcium inactivation and the sensitivity of puff/sparks to variations in the calcium coupling strength and the number of channels at the release

Previous studies of puff/spark dynamics using single channel models that do not include Ca^{2+} inactivation have shown that puff/spark events may terminate due to stochastic attrition even when there are many channels at the release site [Nguyen et al., 2005, DeRemigio and Smith, 2005] (but see [Stern, 1992b]). However, as the number of channels at release sites (N) increases, stochastic attrition becomes increasingly sensitive to variations in the Ca^{2+} coupling strength (c_*). A notable finding of this chapter is that high-affinity Ca^{2+} inactivation facilitates puff/spark termination and extends the range of N and c_* values that result in puff/sparks as long as the rate of Ca^{2+} inactivation is not excessively fast (Figs. 3.5 and 3.6). We also found that the mean duration of puff/sparks is less sensitive to variations in N and c_* when

high-affinity Ca^{2+} inactivation is included in simulations (Fig. 3.9). This decreased sensitivity to variations in N and c_* is consistent with previous studies demonstrating that puff/sparks are less sensitive to the spatial arrangement of channels at release sites when Ca^{2+} inactivation is included in the single channel model [DeRemigio et al., 2007, DeRemigio and Smith, 2007].

3.5.2 The rate of calcium inactivation and puff/spark termination

Another notable finding of this study is that high-affinity Ca^{2+} inactivation may contribute to puff/spark termination in two distinct manners depending on the rate of Ca^{2+} inactivation. Moderate rate Ca^{2+} inactivation often results in the pulsatile recruitment of inactivated channels during puff/spark events, and the increasing number of inactivated channels facilitates the termination of puff/sparks. When Ca^{2+} inactivation promotes puff/spark termination in this manner, the stochastic dynamics are time-irreversible as evidenced by elevated entropy production rates ($\epsilon_p > 0.1$ bits ms^{-1}) and puff/spark trajectories that are asymmetrical in time (Figs. 3.3A and 3.4A). On the other hand, slow Ca^{2+} inactivation results in a relatively constant number of inactivated channels during puff/spark simulations (Figs. 3.3B and 3.4B). This sequestering of channels in the inactivated state reduces the number of de-inactivated channels (\mathcal{O} and \mathcal{C}) that may participate in puff/sparks, thereby promoting puff/spark termination via spontaneous closure of open channels (i.e., stochastic attrition). When Ca^{2+} inactivation promotes puff/sparks in this manner, the stochastic dynamics are nearly time-reversible as evidenced by low entropy production rates ($\epsilon_p < 0.1$ bits ms^{-1}) and puff/sparks that are symmetric in time. In this case, the fraction of inactivated channels increases as the number of channels at the re-

lease site increases, resulting in puff/sparks of stereotyped amplitudes (Fig. 3.7A). A similar phenomenon was observed in Fig. 3.7B when inactivation occurs via a Ca^{2+} -independent mechanism (i.e., activity-dependent or fateful inactivation). Admittedly, the selection of 0.1 bits ms^{-1} as the threshold between low and high entropy production rate is somewhat arbitrary; however, this value can be motivated as a round number that evenly partitions the simulations of Fig. 3.11 into these two categories. See Section 3.5.5 for further discussion of the entropy production rate in Ca^{2+} release site models.

Note that the entropy production rate is not the only response measure that can distinguish between the two roles of Ca^{2+} inactivation discussed above. Another possibility we explored is the change in the fraction of refractory channels throughout the duration of puff/sparks. Using an extension of the matrix analytic formula of Section 4.4, we found that the mean value of this change is larger when the entropy production rate was high and obtained results similar to Fig. 3.6 (not shown).

While some studies have shown that the time constant of Ca^{2+} inactivation may be relatively similar to the duration of puffs and sparks (approximately 100 ms) [Parker et al., 1996b], others suggest Ca^{2+} -dependent or activity-dependent inactivation (and the related phenomenon of adaptation [Györke, 1999]) are much slower, occurring on a time scale of seconds to tens of seconds [Parker and Ivorra, 1990, Mak and Foskett, 1997, Vélez et al., 1997]. Importantly, our results demonstrate that Ca^{2+} inactivation can not be eliminated as a viable negative control mechanism simply on the basis of slow kinetics. On the contrary, slow inactivation mechanisms can effectively ‘tune’ release sites so that the population of channels that are de-inactivated at any given time are more likely to exhibit puff/sparks that terminate via stochastic attrition. Figure 3.12 illustrates this tuning of release sites. The expected number of de-inactivated channels during simulation involving 40 three-state channels and slow,

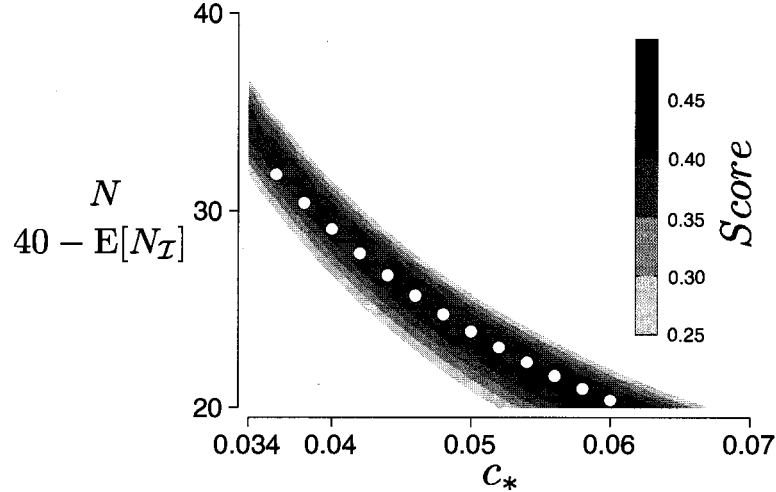


Figure 3.12: Using parameters as in Fig. 3.7A, *white circles* show the expected number of de-inactivated channels ($40 - E[N_I]$) during simulations involving 40 three-state channels and slow, high-affinity Ca^{2+} inactivation as a function of the Ca^{2+} coupling strength (c_*) used. Also shown is the Ca^{2+} puff/spark *Score* of simulations using a two state model that lacks inactivation ($K_{\text{rel}} = \infty$) as a function of the number of channels at release sites (N) and the Ca^{2+} coupling strength (c_*).

high-affinity Ca^{2+} inactivation (*white circles*, calculated using $40 - E[N_I]$) is plotted as a function of the Ca^{2+} coupling strength (c_*) used. All of these simulations exhibit stochastic Ca^{2+} excitability reminiscent of puffs and sparks. The *Score* of simulations involving a two-state single channel model that lacks inactivation is also shown, as a function of the number of channels at release sites (N) and c_* . Because puff/sparks of simulations involving two-state channels terminate exclusively via stochastic attrition, robust puff/sparks ($\text{Score} > 0.25$) are only observed over a range of N values for any fixed c_* . Importantly, the *white circles* occur within this region of N values demonstrating that, while not contributing to puff/spark termination via the recruitment of inactivated channels during puff/spark events, slow inactivation sequesters an appropriate number of channels in the inactivated state such that the remaining number of de-inactivated channels is within the range required to exhibit puff/sparks

that terminate via the spontaneous closure of all open channels.

Figure 3.12 and Figs. 3.5–3.8 demonstrate that Ca^{2+} inactivation with a time constant much longer than puff/spark duration can still promote stochastic Ca^{2+} excitability by decreasing the sensitivity of puff/sparks to the number of channels at the release site (N) and Ca^{2+} coupling strength (c_*). Indeed, because RyRs form clusters of up to 100 channels in ventricular cardiac myocytes [Franzini-Armstrong et al., 1999b], but only a small cohort of 15 or less RyRs participate in any given spark [Wang et al., 2004, Berridge, 2006, Soeller and Cannell, 2002], our simulation results suggest that these Ca^{2+} release sites may be less sensitive to release site density and single channel source amplitude than they otherwise would be in the absence of slow inactivation mechanisms.

3.5.3 Calcium inactivation and puff/spark duration distributions

We found that the probability distribution of puff/spark duration may be unimodal, transitional, or bimodal depending on model parameters (Figs. 3.8 and 3.10). Bimodal puff/spark duration distributions often occur when puff/sparks have elevated entropy production rate and terminate due to the pulsatile recruitment of inactivated channels (Figs. 3.10 and 3.11). Other studies have observed similar bimodal puff/spark duration distributions and postulated that the first (short time) mode corresponds to blips/quarks that terminate rapidly due to stochastic attrition, while the second (long time) mode results from puff/sparks that terminate more slowly due to Ca^{2+} inactivation [Stern et al., 1997, Parker and Yao, 1996, Wang et al., 2002]. While this interpretation is consistent with our simulation results, it is important to note that a unimodal puff/spark duration distribution does not rule out Ca^{2+} inactivation

as a puff/spark termination mechanism (Figs. 3.9 and 3.10).

3.5.4 Limitations of the model

While the assumption of mean-field coupling vastly simplifies release site simulations, the dynamics of Ca^{2+} release sites may sometimes depend on the spatial arrangement of intracellular channels. In previous studies, we have found that release sites with Ca^{2+} activation but no Ca^{2+} inactivation can be sensitive to the arrangement of channels even when the average channel density is unchanged [DeRemigio et al., 2007, DeRemigio and Smith, 2007]. However, these studies also demonstrate that release sites that include both Ca^{2+} activation and inactivation are not particularly sensitive to the exact position of channels, suggesting that the use of the mean-field approximation is not a major limitation of this study.

Another potential limitation of this study is the assumption of instantaneous coupling via local $[\text{Ca}^{2+}]$. When two-state Ca^{2+} activated channels are coupled via a time-dependent Ca^{2+} microdomain, the time constant for Ca^{2+} domain formation and collapse can have a profound effect on the dynamics of puffs and sparks [Mazzag et al., 2005, Huertas and Smith, 2007]. For example, slow domain formation can make it unlikely that blips and quarks will trigger puffs and sparks. On the other hand, slow domain collapse may prohibit the spontaneous termination of Ca^{2+} release events via stochastic attrition. An important question for future research is whether time-irreversible puff/sparks that terminate due to the pulsatile recruitment of inactivated channels and nearly time-reversible puff/sparks with a relatively constant number of inactivated channels are equally sensitive to the time constant for Ca^{2+} domain formation and collapse (which is here assumed to be very fast). This question is perhaps best addressed using a modeling formalism where Ca^{2+} -regulated channels

are mean-field coupled to a time-dependent cytosolic domain [Mazzag et al., 2005]. Dissecting the dynamics of fast and slow inactivation processes in release site models that include luminal depletion [Huertas and Smith, 2007] and allosteric coupling mediated by protein-protein interactions [Groff and Smith, 2007a, Groff and Smith, 2007b] are additional topics for further work.

3.5.5 Entropy production rate in calcium release site models

Note that the three-state single channel model that is the focus of this chapter (Eq. 3.1) does not include any cycles. Consequently, the steady-state probability distribution given by Eq. 3.5 that satisfies global balance (Eqs. 3.3–3.4) also satisfies detailed balance (Eq. 3.11) and the resulting stochastic dynamics of this single channel model are time-reversible. When single channel models of Ca^{2+} -regulated channels include cycles (e.g., the four-state model presented in [Nguyen et al., 2005]), parameters must be chosen to satisfy a thermodynamic constraint so that global balance implies detailed balance when all the Ca^{2+} binding sites of the model experience the same $[\text{Ca}^{2+}]$ [Hill, 1989, Keizer, 1987]. However, when domain $[\text{Ca}^{2+}]$ experience by open channels is elevated above background ($c_d > c_\infty$), the steady-state probability distribution for single channel models with cycles need not satisfy detailed balance [Hill, 1989, Keizer, 1987]. Indeed, when domain Ca^{2+} -mediated transitions are represented in state-transition diagrams with cycles, time-irreversibility of single channel gating is not unexpected, because it is a manifestation of the ER/cytosol concentration gradient. It is as though the Ca^{2+} -binding site of the channel is exposed alternately to the cytosolic and luminal ‘baths’ depending on whether the channel is closed or open [Hill, 1989]. And yet, as mentioned above, the stochastic gating of single channel models without cycles is time-reversible even when domain

Ca^{2+} -mediated inactivation is included.

Although the stochastic dynamics of the three-state single channel model that is the focus of this chapter is time-reversible, when two of these channels are coupled as in Eq. 3.6, the resulting Markov chain is time-irreversible. As discussed in [Hill, 1989], this can be demonstrated by comparing the product of the four transition rates encountered when moving clockwise versus counter-clockwise around the cycle that includes states $(1, 1, 0)$, $(1, 0, 1)$, $(0, 1, 1)$, $(0, 2, 0)$, and noting that they are not equal,

$$k_b^+ (c_\infty + c_d)^\eta \cdot k_a^+ c_\infty^\eta \cdot k_b^- \cdot 2k_a^- \neq k_a^+ (c_\infty + c_*)^\eta \cdot 2k_b^+ (c_\infty + c_* + c_d)^\eta \cdot k_a^- \cdot k_b^- . \quad (3.14)$$

When the rate constants are eliminated from this expression,

$$(c_\infty + c_d)^\eta c_\infty^\eta \neq (c_\infty + c_*)^\eta \cdot (c_\infty + c_* + c_d)^\eta , \quad (3.15)$$

one can see that it is the *interaction* between two coupled three-state channels ($c_* > 0$) that causes the stochastic dynamics to be time-irreversible, as opposed to the domain $[\text{Ca}^{2+}] (c_d)$ experienced by each channel.

Because the stochastic dynamics of two instantaneously coupled three-state channels are time-irreversible when $c_* > 0$, it is understood that the N channel release site models that are the focus of this chapter also have this property. This observation that the coupled gating of time-reversible single channel models mediated by increases in the local $[\text{Ca}^{2+}]$ can result in time-irreversible puff/sparks is consistent with prior computational work by several groups [Wang et al., 2002, Nguyen et al., 2005]. But note that our simulation results and Eqs. 3.14–3.15 demonstrate that this phenomenon can occur even when the single channel model includes no cycles.

3.6 Conclusions

This chapter clarifies how Ca^{2+} inactivation of IP_3Rs and RyRs influences the dynamics of Ca^{2+} puff/spark generation and termination. Importantly, the puff/spark statistics of this chapter (e.g., the Ca^{2+} puff/spark *Score* and probability distribution of puff/spark duration) are directly calculated from the infinitesimal generator matrices (Q -matrices) corresponding to release sites using matrix analytic formulas. While these direct calculations vastly simplify parameter studies of puff/spark statistics, they are only computationally feasible because the Markov chain models of Ca^{2+} release sites considered in this chapter assume that channels experience mean-field Ca^{2+} coupling. Consequently, release site models have a moderate number of configurations and the corresponding Q -matrices that can be held in memory. For example, the Q matrix for a release site composed of 20 mean-field coupled three-state channels is 231-by-231. In comparison, a Markov chain model for a release site composed of 20 spatially distinguishable three-state channels has over three billion unique configurations making direct calculation of puff/spark statistics beyond the capabilities of modern desktop computers. However, as we saw in Chap. 2, puff/spark statistics can always be estimated from Monte Carlo simulations when direct calculations are impractical. Chapter 4 details the matrix analytic formulas used to directly calculate puff/spark statistics from Q and an exact numerical method used to simulate the Ca^{2+} release site models that are the focus of this dissertation.

Chapter 4

Numerical methods for calcium release site modeling

4.1 Summary

The theoretical studies of Chap. 2 and Chap. 3 were carried out using the high level programming language of MATLAB[®] (The MathWorks, Inc., Natick, MA). This chapter details the numerical methods used in these studies, some of which are significant contributions to the theoretical study of Ca²⁺ puffs and sparks. For example, Section 4.2 presents a vectorized formulation of Gillespie's method applied to clusters of Ca²⁺ channels. This formulation significantly accelerates numerical simulations of release sites facilitating the estimation of puff/spark statistics from Monte Carlo simulations. In Section 4.4, matrix analytic formulas are derived to calculate puff/spark duration and inter-event interval distributions directly from the infinitesimal generator matrices of release sites. These formulas are required for the parameter studies of puff/spark dynamics presented in Chap. 3.

This chapter also presents a method for agglomerating release site configurations

based on the symmetries of model release site ultrastructures (Section 4.5). This method results in release site models with drastically fewer configurations, yet simulations of these contraction Markov processes have dynamics and statistics identical to corresponding full model simulations. While not utilized in the studies of Chap. 2 and Chap. 3, this method is included because it is a promising tool for future theoretical studies of Ca^{2+} puffs and sparks.

Using the notation of Chap. 2, Secs. 4.2 and 4.3 denote release site configurations as a vector $\mathbf{i} = (i_1, i_2, \dots, i_N)$ where i_n is the state of channel n . In contrast, a scalar i is used to denote release site configurations in Secs. 4.5 and 4.6.

4.2 Exact numerical simulation

The Ca^{2+} release site models presented in this manuscript are continuous-time Markov chains simulated using Gillespie's method, a numerical method with no intrinsic time step [Gillespie, 1976, Smith, 2002, Nguyen et al., 2005]. After choosing an initial release site configuration, \mathbf{i} , this method requires the nonzero rates q_{ij} for the allowed transitions $\mathbf{i} \rightarrow \mathbf{j}$ to determine the subsequent release site configuration. An exponentially distributed random variable τ with mean $1/\sum_{j \neq i} q_{ij}$ is then generated giving the dwell time in the current release site configuration \mathbf{i} . The destination configuration \mathbf{j} is selected by choosing a random variable Y uniformly distributed on a partitioned interval of length $\sum_{j \neq i} q_{ij}$ where the $\mathbf{i} \rightarrow \mathbf{j}$ transition occurs if Y falls on the partition associated with q_{ij} ($\mathbf{i} \neq \mathbf{j}$). The release site configuration as a function of time is produced by repeating these steps.

It remains to show how the q_{ij} are determined. When the infinitesimal generator matrix Q is sufficiently small to be held in memory, the required transition rates are the non-zero off-diagonal elements of the row corresponding to configuration \mathbf{i} .

When forming Q is impractical due to memory constraints, an efficient approach is to represent the release site configuration as the $N \times M$ matrix Σ where

$$\Sigma_{nm}(t) = \begin{cases} 1 & \text{if } i_n = m \\ 0 & \text{otherwise.} \end{cases} \quad (4.1)$$

By arranging the required transition rates in an $N \times M$ matrix $R = (r_{nm})$ where r_{nm} is the rate at which channel n makes an $i_n \rightarrow m$ transition, these rates can be determined by evaluating the matrix analytic expression,

$$R(t) = [\Sigma \hat{K}^-] \circ \hat{\Omega}^- + [\text{diag}(c_\infty \mathbf{e} + C^T \Sigma \mathbf{u})^\eta \Sigma \hat{K}^+] \circ \hat{\Omega}^+ \quad (4.2)$$

where the \circ operator denotes an element-by-element Hadamard product. In this expression, the $M \times M$ matrices \hat{K}^+ and \hat{K}^- are identical to K^+ and K^- (Eq. 2.3) but with zeros on the principal diagonals, C is the $N \times N$ Ca^{2+} coupling matrix (Eq. 2.7c), \mathbf{e} is a $N \times 1$ column vector of ones, and \mathbf{u} is a $M \times 1$ column vector where entries of 0 and 1 denote closed and open states in the single channel model. Note that the column vector $\Sigma \mathbf{u}$ indicates channels that are open in release site configuration \mathbf{i} , $c_\infty \mathbf{e} + C^T \Sigma \mathbf{u}$ is the $[\text{Ca}^{2+}]$ experienced by each channel, and left multiplying by the diagonal matrix $\text{diag}(c_\infty \mathbf{e} + C^T \Sigma \mathbf{u})^\eta$ scales the association rate constants (\hat{K}^+) by the appropriate $[\text{Ca}^{2+}]$.

The matrices $\hat{\Omega}^-$ and $\hat{\Omega}^+$ that account for allosteric coupling are formed from the $N \times M$ matrix

$$\Psi = (\psi_{nm}) = A \Sigma \mathcal{E} \quad (4.3)$$

where A is the $N \times N$ adjacency matrix (Eq. 2.10a), \mathcal{E} is the $M \times M$ allosteric energy matrix (Eq. 2.14), and ψ_{nm} is the allosteric interaction energy that channel

n would experience in release site configuration Σ provided it was in state m . The elements of the $N \times M$ matrix $\Omega = (\omega_{nm})$ where $\omega_{nm} = \psi_{nm} - \psi_{ni_n}$ give the change in allosteric energy that channel n would experience if it were to make an $i_n \rightarrow m$ transition. Finally, the elements of the matrices $\hat{\Omega}^\pm = (\hat{\omega}_{nm}^\pm)$ used in Eq. 4.2 are given by $\hat{\omega}_{nm}^\pm = \exp(-\nu^\pm \omega_{nm})$ where ν^+ and ν^- partition allosteric contributions between forward and reverse rates ($\nu^- = 1 - \nu^+$). In this manuscript $\nu^+ = 0$, $\hat{\Omega}^+$ is an $N \times M$ matrix of ones, and $\hat{\Omega}^- = (\hat{\omega}_{nm}^-)$ where $\hat{\omega}_{nm}^- = \exp(-\omega_{nm})$.

A MATLAB[®] subroutine that numerically simulates Markov chain models of Ca²⁺ release sites using the vectorized implementation of Gillespie's method formulated above is presented in Section 4.7.1.

4.3 Calculating the stationary probability distribution

A continuous-time Markov chain model of a Ca²⁺ release site such as that considered in this manuscript has a finite number of states and is irreducible. Consequently, the limiting probability distribution (as would be observed over an infinitely long simulation) does not depend on the initial condition. This limiting probability distribution is equal to the unique stationary distribution $\boldsymbol{\pi}$ satisfying global balance and conservation of probability [Stewart, 1994], that is,

$$\boldsymbol{\pi}Q = 0 \quad \text{subject to} \quad \boldsymbol{\pi}e = 1 \quad (4.4)$$

where Q is the infinitesimal generator matrix, $\boldsymbol{\pi}$ is a row vector, and e is a commensurate column vector of ones.

When Q is sufficiently small to be held in memory, Eq. 4.4 may be solved using

several direct approaches. For example, we may define the stochastic matrix $W = (w_{ij}) = I + Q/\lambda$ where I is an identity matrix and $\lambda > \max_i |q_{ii}|$ so that $w_{ij} \geq 0$. It follows from Eq. 4.4 and $W\mathbf{e} = 1$ that $\boldsymbol{\pi}W = \boldsymbol{\pi}$. Thus, $\boldsymbol{\pi}$ is found by calculating the eigenvector of W having a corresponding eigenvalue of 1.

An alternate approach is to define the auxiliary matrix Z and auxiliary column vector \mathbf{b} such that

$$Z = \begin{pmatrix} Q & \mathbf{e} \end{pmatrix} \quad \text{and} \quad \mathbf{b} = \begin{pmatrix} \mathbf{0} \\ 1 \end{pmatrix} \quad (4.5)$$

and solve the overdetermined linear system $\boldsymbol{\pi}Z = \mathbf{b}$ for $\boldsymbol{\pi}$. The solution is

$$\boldsymbol{\pi} = \mathbf{b}Z^T (ZZ^T)^{-1} \quad (4.6)$$

although in some situations, ZZ^T may be ill-conditioned and the pseudoinverse of Z given by $(ZZ^T)^{-1}$ may be difficult to calculate. The probability distribution of the number of open channels at the release site is constructed from $\boldsymbol{\pi}$ by collecting all elements corresponding to configurations with the same number of open channels. An example MATLAB[®] subroutine that numerically calculates $\boldsymbol{\pi}$ is presented in Section 4.7.2. This subroutine includes a user defined flag that indicates which of the two above methods is used.

When storage requirements for Q become excessive, $\boldsymbol{\pi}$ can not be calculated directly. Instead, we estimate $\boldsymbol{\pi}$ from Monte Carlo simulations using

$$\pi_i \approx \frac{1}{T} \int_0^T \mathbb{1}\{\mathbf{S}(t) = \mathbf{i}\} dt \quad (4.7)$$

where $\mathbb{1}$ is the indicator set function, $\mathbf{S}(t)$ is the configuration of the release site at

time t , and T is a sufficiently long observation period. While the T necessary for convergence of π may be excessive, we only require the probability distribution of the number of open channels to calculate spark statistics such as the *Score*. Because this distribution is a contraction of π , good estimates require a substantially shorter observation window (T).

4.4 Direct calculation of puff/spark statistics

4.4.1 Puff/spark duration

For the purposes of this manuscript, puff/spark duration is the interval beginning when a specified number (κ) of channels open ($N_{\mathcal{O}} = \kappa - 1 \rightarrow \kappa$) and ending when all channels close ($N_{\mathcal{O}} = 1 \rightarrow 0$). We chose κ to be one-fifth of the release site size in Chap. 2 and $\kappa = 5$ in Chap. 3 to exclude small amplitude puff/spark events. While the distribution of puff/spark durations may be estimated through Monte Carlo simulation, it can be more efficiently obtained by direct calculation using the Ca^{2+} release site generator matrix Q as described below. First, the state space of the Ca^{2+} release site model is partitioned into four aggregate classes \mathcal{O}_0 , \mathcal{O}_1 , \mathcal{O}_κ , and \mathcal{O}_* where the symbols \mathcal{O}_0 , \mathcal{O}_1 , and \mathcal{O}_κ denote the sets of all configurations with zero, one, or κ open channels, respectively, and \mathcal{O}_* denotes all other states. The generator matrix Q is then permuted into the following form

$$Q = \left(\begin{array}{c|ccc} Q_{00} & Q_{01} & Q_{0\kappa} & Q_{0*} \\ \hline Q_{10} & Q_{11} & Q_{1\kappa} & Q_{1*} \\ Q_{\kappa 0} & Q_{\kappa 1} & Q_{\kappa\kappa} & Q_{\kappa*} \\ Q_{*0} & Q_{*1} & Q_{*\kappa} & Q_{**} \end{array} \right) = \left(\begin{array}{c|c} Q_{00} & Q_{0\mathcal{B}} \\ \hline Q_{\mathcal{B}0} & Q_{\mathcal{B}\mathcal{B}} \end{array} \right) \quad (4.8)$$

where each partition contains rates for transitions between (or within) aggregate classes, the second equality defines the matrices Q_{0B} , Q_{B0} , and Q_{BB} , and the aggregate class \mathcal{O}_B includes all configurations with one or more open channels ($\mathcal{O}_B = \mathcal{O}_1 \cup \mathcal{O}_\kappa \cup \mathcal{O}_*$).

As defined above, puff/spark duration is a random variable X giving a sojourn time in \mathcal{O}_B that begins in \mathcal{O}_κ . It is well known that the probability distribution of X is [Ball and Geoffrey, 2000, Ball et al., 2000]

$$f_X(x) = -\phi_B e^{xQ_{BB}} Q_{BB} e_B > 0 \quad (4.9)$$

where e_B is a commensurate column vector of ones and ϕ_B is a commensurate row vector containing the probability of a sojourn starting in the various states of \mathcal{O}_B . The expectation of X (i.e., the mean puff/spark duration) is found by integrating Eq. 4.9,

$$E[X] = -\int_0^\infty x \phi_B e^{xQ_{BB}} Q_{BB} e_B dx = -\phi_B Q_{BB}^{-1} e_B > 0. \quad (4.10)$$

Because the initial state of a puff/spark is always in \mathcal{O}_κ , the elements of ϕ_B corresponding to states not in \mathcal{O}_κ are zero, that is

$$\phi_B = (\mathbf{0}_1 \ \phi_\kappa \ \mathbf{0}_*) \quad (4.11)$$

where $\mathbf{0}_1$ and $\mathbf{0}_*$ are row vectors of zeros with the same number of elements as \mathcal{O}_1 and \mathcal{O}_* , respectively.

It remains to be shown how ϕ_κ is determined. If there is only a single release site configuration with κ open channels, then $\phi_\kappa = 1$. However, in general there may be many configurations with $N_{\mathcal{O}} = \kappa$ and ϕ_κ is calculated as follows. We begin by noticing that since puff/spark termination is an $\mathcal{O}_1 \rightarrow \mathcal{O}_0$ transition, the initiation of

all puff/sparks is preceded by an $\mathcal{O}_0 \rightarrow \mathcal{O}_1$ transition. The steady-state probability flux from state of \mathcal{O}_0 to each state of \mathcal{O}_1 is given by the row vector

$$\boldsymbol{\alpha}_1 = \boldsymbol{\pi}_0 Q_{01} \quad (4.12)$$

where $\boldsymbol{\pi}_0$ is the portion of the stationary distribution corresponding to class \mathcal{O}_0 .

However, not all $\mathcal{O}_0 \rightarrow \mathcal{O}_1$ transitions indicate the beginning of puff/spark events because the Markov process may proceed to a state in \mathcal{O}_κ (signaling puff/spark initiation), or it may return to \mathcal{O}_0 having never entered \mathcal{O}_κ . The portion of the $\mathcal{O}_0 \rightarrow \mathcal{O}_1$ probability flux needed in Eq. 4.11 that actually results in puff/spark initiation is given by $\boldsymbol{\phi}_\kappa = \boldsymbol{\gamma}_\kappa / \boldsymbol{\gamma}_\kappa \mathbf{e}_\kappa$ where $\boldsymbol{\gamma}_\kappa \mathbf{e}_\kappa$ is an inner product (a scalar) that normalizes $\boldsymbol{\phi}_\kappa$, and $\boldsymbol{\gamma}_\kappa$ is the probability flux of puff/spark initiation that can be extracted from the vector-matrix product

$$(\boldsymbol{\gamma}_0 \ \boldsymbol{\gamma}_\kappa) = (\boldsymbol{\alpha}_1 \ \mathbf{0}_\star) \left[- \begin{pmatrix} Q_{11} & Q_{1\star} \\ Q_{\star 1} & Q_{\star\star} \end{pmatrix}^{-1} \begin{pmatrix} Q_{10} & Q_{1\kappa} \\ Q_{\star 0} & Q_{\star\kappa} \end{pmatrix} \right]. \quad (4.13)$$

In Eq. 4.13, the term in brackets is a stochastic matrix (a matrix with non-negative elements and rows that sum to one) giving the probability of first arriving in each configuration of $\mathcal{O}_0 \cup \mathcal{O}_\kappa$ given each possible initial configuration in $\mathcal{O}_1 \cup \mathcal{O}_\star$.

4.4.2 Inter-puff/spark interval

Inter-puff/spark interval is the period beginning when a puff/spark terminates ($N_{\mathcal{O}} = 1 \rightarrow 0$) and ending when a subsequent puff/spark begins ($N_{\mathcal{O}} = \kappa - 1 \rightarrow \kappa$). The distribution of inter-puff/spark intervals may also be calculated using Eq. 4.9 and requires only that the aggregate class $\mathcal{O}_{\mathcal{B}}$ be redefined to include all configurations

with less than κ or greater than κ open channels ($\mathcal{O}_B = \mathcal{O}_0 \cup \mathcal{O}_1 \cup \mathcal{O}_*$) and that Q be appropriately permuted to reflect this new \mathcal{O}_B . Because, inter-puff/spark interval is a random variable X giving a sojourn time in \mathcal{O}_B that begins in \mathcal{O}_0 , the row vector containing the probability of a sojourn starting in the various configurations of \mathcal{O}_B contains many zero elements and is given by

$$\phi_B = (\phi_0 \mathbf{0}_1 \mathbf{0}_*). \quad (4.14)$$

If there is only a single release site configuration with no open channels, then $\phi_0 = 1$. If there are many such configurations, the non-zero elements of the right hand side of Eq. 4.14 are given by $\phi_0 = \gamma_0/\gamma_0 \mathbf{e}_0$ where γ_0 is calculated using the vector-matrix product

$$\gamma_0 = (\mathbf{0}_1 \ \gamma_\kappa \ \mathbf{0}_*) \left[- \left(\begin{array}{ccc} Q_{11} & Q_{1\kappa} & Q_{1*} \\ Q_{\kappa 1} & Q_{\kappa\kappa} & Q_{\kappa*} \\ Q_{*1} & Q_{*\kappa} & Q_{**} \end{array} \right)^{-1} \left(\begin{array}{c} Q_{10} \\ Q_{\kappa 0} \\ Q_{*0} \end{array} \right) \right]. \quad (4.15)$$

The stochastic matrix in the brackets of Eq. 4.15 collects the probability of arriving in each configuration of \mathcal{O}_0 given each possible initial configuration in $\mathcal{O}_1 \cup \mathcal{O}_\kappa \cup \mathcal{O}_*$, and γ_κ is the probability flux of puff/spark initiation calculated in Section 4.4.1.

A MATLAB[®] subroutine that implements the above matrix analytic formulas to calculate the distribution and expectation of puff/spark duration and inter-puff/spark interval is presented in Section 4.7.3.

4.5 State space contraction using release site symmetries

Much of the complexity of a Markov chain model of a Ca^{2+} release site that includes a representation of the release site's ultrastructure (e.g., channels arranged in a square lattice or hexagonal lattice) is due to the accurate account of the pair-wise interactions of channels, summarized by the elements of the Ca^{2+} coupling matrix C and allosteric adjacency matrix A (see Chap. 2). The M^N -by- M^N infinitesimal generator matrix Q corresponding to a model release site composed of N spatially distinguishable M -state channels can sometimes be held in memory but is often prohibitively large to perform matrix calculations such as those described in Sections 4.3 and 4.4, even for moderately sized release sites. However, it is often possible to simplify calculations by performing an appropriate contraction of Q that agglomerates release site configurations based on the symmetries of the release site ultrastructure.

Perhaps the easiest way to motivate this state space contraction is to consider the twelve example configurations of a release site composed of seven two-state channels shown in Fig. 4.1. Notice that the spatial arrangement of the four open and the three closed channels is unique in each configuration. However, the hexagonal lattice on which channels are positioned has six-fold rotational symmetry and reflective symmetry about an appropriately selected axis. Thus, one may obtain any configuration shown by performing a series of rotations and/or reflections on any other configuration. Consequently, all twelve configurations belong to the same symmetry group and the corresponding elements of the Q -matrix may be agglomerated.

In general, the contracted Q -matrix is calculated using

$$\hat{Q} = S^T Q V \tag{4.16}$$

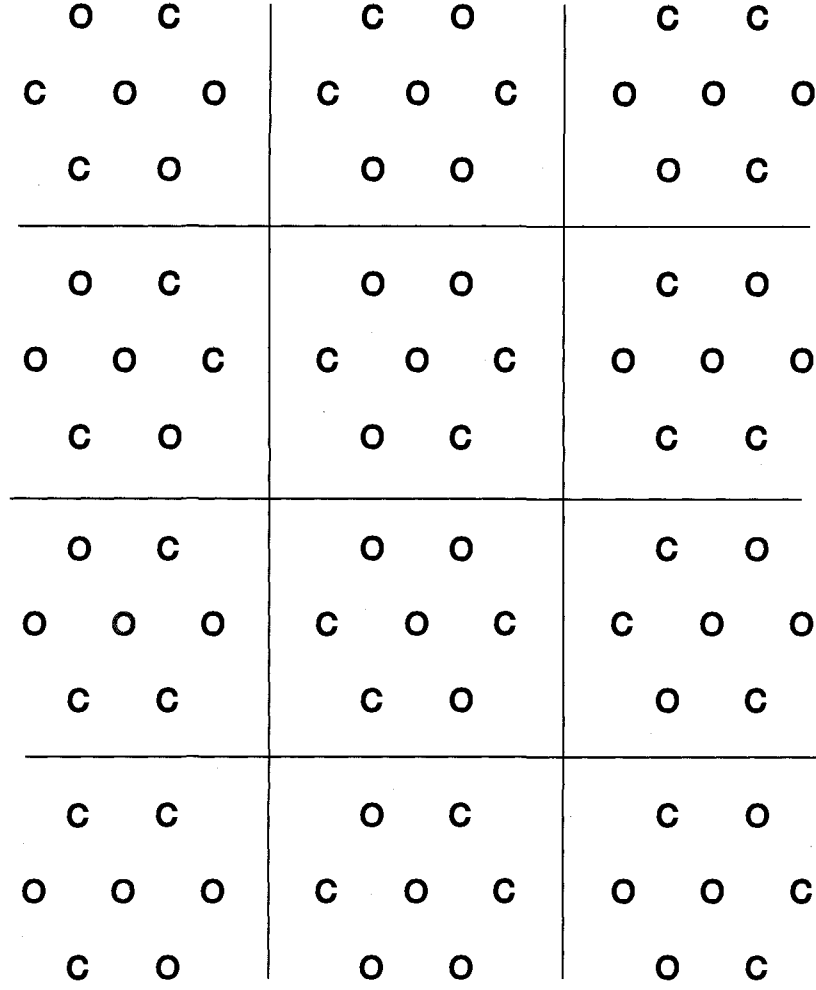


Figure 4.1: The twelve unique release site configurations shown involve seven two-state channels arranged on a hexagonal lattice and belong to a single symmetry group.

where the sparse M^N -by- B collector matrix V maps each of the M^N configurations of the full model to one of B unique symmetry groups such that

$$V = (v_{ij}) = \begin{cases} 1 & \text{if configuration } i \text{ belongs to symmetry group } j \\ 0 & \text{otherwise.} \end{cases} \quad (4.17)$$

The M^N -by- B distributor matrix S scales transition rates to account for combina-

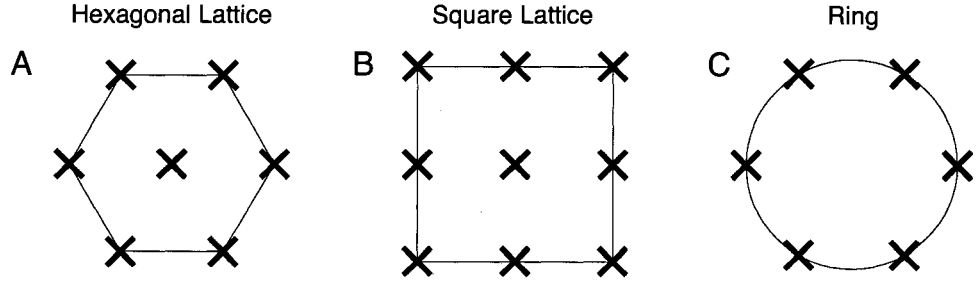


Figure 4.2: In release site models, channels (indicated by X s) are often arranged in a regular lattice with rotational and reflective symmetries such as (A) a hexagonal lattice, (B) a square lattice, or (C) a ring.

torics and is given by

$$S = (\mathbf{s}_1, \mathbf{s}_2, \dots, \mathbf{s}_B) \quad (4.18)$$

where $\mathbf{s}_j = \mathbf{v}_j / \mathbf{e}^T \mathbf{v}_j$, \mathbf{v}_j is the j th column of V , and \mathbf{e}^T is a commensurate row vector of ones. Section 4.7.4 presents a MATLAB[®] subroutine that efficiently maps release site configurations to symmetry groups and constructs V . Importantly, the contracted Markov process satisfies the strong lumpability condition such that $V\hat{Q} = QV$. This condition implies that all configurations in any lumped state have identical transition rates into all configurations of any destination lumped state. In other words, simulating the full Markov process and viewing the results through V is identical to simulation \hat{Q} .

Table 4.1 illustrates that the size of \hat{Q} ($B \times B$) depends on the arrangement and number of channels at a release site (N) and the number of states of the single channel model (M). The three ultrastructures considered are channels arranged on a hexagonal lattice, a square lattice, and a ring as illustrated in Figs. 4.2A, B, and C, respectively. Notice that the percent reduction of the state space after performing the contraction ($1 - B/M^N$) increases with N and M . On average, the percent reduction is least for square lattices because such release sites only have 4-fold rotational sym-

Ultrastructure	N	M	M^N	B	% contraction $1-B/M^N$	wall-time (s) $\pi Q=0$	wall-time (s) $\pi \hat{Q}=0$
Hexagonal Lattice	7	2	128	26	0.80	0.05	0.03
	7	3	2187	276	0.87	0.74	0.23
	7	4	16384	1720	0.90	5.87	0.56
	19	2	524288	45336	0.91	395.65	25.52
Square Lattice	9	2	512	102	0.80	0.10	0.06
	9	3	19683	2862	0.85	10.93	1.21
	9	4	262144	34960	0.87	195.65	18.96
	16	2	65536	8548	0.87	19.47	2.04
Ring	10	2	1024	78	0.92	0.14	0.06
	10	3	59049	3210	0.95	38.04	1.38
	10	4	1048576	53764	0.95	1077.49	42.10
	20	2	1048576	27012	0.97	697.12	10.04

Table 4.1: The number of configurations of example release site models (M^N) and corresponding contracted models (B) formulated using release site symmetries to agglomerate states. Wall-times displayed are for solving $\pi Q = 0$ for the stationary distribution π subject to $\pi e = 1$ where e is a commensurate column vector of ones. The stationary distribution π is the eigenvector of the stochastic matrix $W = (w_{ij}) = I + Q/\lambda$ ($\lambda > \max_i |q_{ii}|$) having a corresponding eigenvalue of one (see Section 4.3) and is calculated using MATLAB[®] and an implementation of the Arnoldi algorithm [Stewart, 1994]. Calculations are performed on a MacBook Pro with 2.33 Ghz Intel Core 2 Duo with 2 GB of RAM. In each case, the state-transition diagram of the single channel model assumes sequential Ca^{2+} binding and the final state is open. Forward rates are given by $1.5(c_\infty + N_{\mathcal{O}}c_*) \text{ ms}^{-1}$ where $N_{\mathcal{O}}$ is the number of open channels at the release site and $c_\infty = c_* = 0.05 \mu\text{M}$. The reverse rates are 0.5 ms^{-1} .

metry, and greatest for rings which have N -fold rotational symmetry. The wall-times shown in Table 4.1 are for calculating the stationary distributions of Q and \hat{Q} as described in the table caption, and illustrate the computational advantage of using \hat{Q} .

4.6 A stochastic automata network descriptor for calcium release site models that include allosteric interactions

An ongoing area of research is the development of memory efficient techniques to calculate the stationary distribution of Markov chain models of Ca^{2+} puffs and sparks. Importantly, such methods do not require the infinitesimal generator matrix Q but only the matrix-vector product Qx where x is a commensurate column vector. Because Markov chain models of Ca^{2+} release sites derived from stochastic models of single IP_3R and RyR gating are stochastic automata networks (SANs), these numerical methods take advantage of the highly structured SAN descriptor representation of Q . Previous work established the SAN descriptor applicable to a cluster of Ca^{2+} -regulated Ca^{2+} channels instantaneously coupled via local Ca^{2+} [Nguyen et al., 2005]. Although this formulation is not used in Chap. 2 or Chap. 3, here we extend the SAN descriptor to include inter-protein allosteric interactions.

Recall that the infinitesimal generator matrix of an M -state Ca^{2+} -regulated Ca^{2+} channel may be written as [Nguyen et al., 2005]

$$Q^{(1)} = K_-^{(1)} + \text{diag}(c_\infty \mathbf{e}^{(1)} + c_d \mathbf{u}^{(1)})^\eta K_+^{(1)}, \quad (4.19)$$

where the $M \times M$ matrices $K_+^{(1)}$ and $K_-^{(1)}$ hold the association and dissociation rate constants of the single channel model, respectively, c_∞ is the background $[\text{Ca}^{2+}]$, c_d is the domain $[\text{Ca}^{2+}]$, η is the cooperativity of Ca^{2+} binding, \mathbf{e} is a $N \times 1$ column vector of ones, and \mathbf{u} is a $M \times 1$ column vector where entries of 0 and 1 denote closed and open states in the single channel model. Following [Nguyen et al., 2005], the

M^N -by- M^N infinitesimal generator matrix corresponding to a release site composed of N M -state channels experiencing instantaneous coupling via changes in the local $[\text{Ca}^{2+}]$ can be compactly written as a stochastic automata network (SAN) descriptor

$$Q^{(N)} = Q_-^{(N)} + Q_+^{(N)} \quad (4.20)$$

where $Q_-^{(N)}$ is

$$Q_-^{(N)} = \sum_{n=1}^N I^{(N-n)} \otimes K_-^{(1)} \otimes I^{(n-1)} \quad (4.21)$$

and \otimes denotes the Kronecker product while $I^{(n)}$ denotes an identity matrix of size M^n . The elements of $Q_+^{(N)}$ are functions of the N -by- N Ca^{2+} coupling matrix C ,

$$Q_+^{(N)} = \sum_{n=1}^N \text{diag} (c_\infty \mathbf{e}^{(N)} + \Gamma_{*n})^\eta \left(I^{(N-n)} \otimes K_+^{(1)} \otimes I^{(n-1)} \right), \quad (4.22)$$

where $\mathbf{e}^{(n)}$ is a M^n -by-1 column vector of ones, Γ_{*n} is the n th column of the M^N -by- N matrix

$$\Gamma = (\gamma_{in}) = UC \quad (4.23)$$

and γ_{in} gives the increase in the local $[\text{Ca}^{2+}]$ above c_∞ experienced by channel n when the release site is in configuration i . The M^N -by- N matrix U in Eq. 4.23 is defined as

$$U = (u_{in}) = \begin{cases} 1 & \text{if channel } n \text{ is open in release site configuration } i \\ 0 & \text{otherwise} \end{cases} \quad (4.24)$$

and may be constructed column-by-column using

$$U_{*n} = \mathbf{e}^{(N-n)} \otimes \mathbf{u}^{(1)} \otimes \mathbf{e}^{(n-1)}. \quad (4.25)$$

The SAN descriptor is extended to include inter-protein physical coupling using the methodology of Chap. 2 where transition rates are modified by state-dependent allosteric interaction energies. This extension only requires that the matrix of association ($Q_+^{(N)}$) and dissociation rates ($Q_-^{(N)}$) be left and right-hand multiplied by diagonal matrices. Using $\tilde{Q}_\pm^{(N)}$ to denote the unmodified transition rate matrices of Eqs. 4.21 and 4.22, the modified transition rate matrices are given by

$$Q_\pm^{(N)} = \text{diag}(\omega_\pm) \tilde{Q}_\pm^{(N)} \text{diag}(\hat{\omega}_\pm). \quad (4.26)$$

The elements of the M^N -by-1 vectors ω_+ , ω_- , $\hat{\omega}_+$, and $\hat{\omega}_-$ are given by $\omega_{\pm,i} = \exp(\nu_\pm \psi_i)$ and $\hat{\omega}_{\pm,i} = 1/\omega_{\pm,i}$ where ν_+ and ν_- partitions allosteric contributions between association and dissociation rates ($\nu_- = 1 - \nu_+$), and ψ_i is an element of the M^N -by-1 vector ψ ,

$$\psi = \sum_{\substack{n,n'=1 \\ n < n'}}^N \sum_{m=1}^M a_{nn'} \mathbf{e}^{(N-n')} \otimes \mathcal{E}_{*m} \otimes \mathbf{e}^{(n'-n-1)} \otimes \lambda_m \otimes \mathbf{e}^{(n-1)}, \quad (4.27)$$

giving the total allosteric interaction energy at the release site in each configuration. In Eq. 4.27, $a_{nn'}$ is an element of the allosteric adjacency matrix A , \mathcal{E}_{*m} is the m th column of the allosteric energy matrix \mathcal{E} (see Chap. 2), and λ_m is an M -by-1 vector of all zeros except for an element of 1 in the m th row. The outer sum is over all unique pairs of channels at the release site and the inner sum is over all M states in the single channel model.

4.7 Example MATLAB[®] subroutines

4.7.1 Subroutine to numerically simulate Markov chain models of calcium release sites

```
function [time,nOpen,state] = ...
    ...vectorizedGillespie(Kp,Km,u,C,E,A,eta,nup,totalStates,initS)

% Function to numerically simulate a Markov chain model of a calcium
% release site using a vectorized implementation of Gillespie's method

% INPUT ARGUMENTS

% Kp - matrix of single channel association constants
% Km - matrix of single channel dissociation constants
% u - vector where elements of 1 indicate open states
% C - calcium coupling matrix
% E - allosteric energy matrix
% A - allosteric adjacency matrix
% cainf - background calcium concentration
% eta - cooperativity of calcium binding
% nup - allosteric partitioning coefficient, nup = 0 assuming rates of
% calcium association is rate limited and num = 1-nup;
% totalStates - total number of configuration changes to calculate
% initS - initial state matrix

% OUTPUT ARGUMENTS

% time - vector of times
% nOpen - vector of number of open channels
% state - totalStates-by-N matrix where column j of row i is the state
% of channel j in release site configuration i

[N,N] = size(C);
[M,M] = size(E);

% ensure diagonals of Kp and Km are zero and matrices are sparse
I = eye(size(Kp));
Kp = Kp.*not(I); Kp = sparse(Kp);
Km = Km.*not(I); Km = sparse(Km);
u = u(:); % col vec
```



```

u = sparse(u);
A = sparse(A);
E = sparse(E);

rand('state',sum(100*clock));

% initialize data vectors
time = zeros(totalStates,1)
state = zeros(totalStates,N);
nOpen = zeros(totalStates,1);

timeNow = 0;
time(1,1) = timeNow;

[stateNow, blah] = find(initS'); % find state of each channel as a vector
state(1,:) = stateNow(:)';

nOpen(1,1) = sum(initS*u);

i = 1
while i < totalStates
    i = i+1; % while loop indexing

    opench = (S*U)'; % vector indicating open channels at the release site

    Psi = A*SNow*E; % matrix of possible allosteric interaction energies
    % where element n,m is the energy experienced by channel n provided it
    % is in state m.

    num = 1-nup;
    O = Psi - (Psi.*S)*ones(M,M);
    OmHat = exp(-num*O);
    OpHat = exp(-nup*O);

    openCh = S*u; % vector of open channels

    R = (S*Km).*OmHat + ((diag(cainf + C'*openCh).^eta)*S*Kp).*OpHat;
    R = reshape(R,[1 N*M]);

    sumR = sum(R);
    tau = -log(rand(1))/sumR; % negative sign because sumR is postive
    timeNow = timeNow+tau;

    % update the state matrix
    j = min(find(sumR*rand(1)<cumsum(R))); % which transition took place

```

```

    [ch_index,state_to] = ind2sub([N M],j); % which channel changed state
    state_from = find(S(ch_index,:));
    S(ch_index,state_from)=0;
    S(ch_index,state_to)=1;

    time(ii,1) = timeNow;
    nOpen(ii,1) = sum(openCh);

    % find current state as a vector
    [stateNow, blah] = find(S');
    state(ii,:) = stateNow(:)';

end

return

```

4.7.2 Subroutine to calculate the stationary distribution of an infinitesimal generator matrix

```

function [piVect] = stationaryDistribution(Q,flag)

% Function to calculate the stationary distribution of Q

% INPUT ARGUMENTS
% Q - infinitesimal generator matrix
% flag - specify whether to use the eigenvalue or least squares
% method

% OUTPUT ARGUMENTS
% piVect - the stationary distribution

Q = sparse(Q);

switch flag

    case 'eigenvalue'

        lambda = 1.01*max(abs(diag(Q)));
        W = speye(size(Q))+Q/lambda;
        opts.disp = 0;
        % returns the eigenvector corresponding to the largest eigenvalue

```

```

    [v,d] = eigs(@matrixvectorprod, M^N, 1, 'LR', opts);
    piVect = v/sum(v);
    piVect = piVect(:);

    case 'leastquares'

        [N,N]=size(Q);
        b = sparse(N+1,1,1,N+1,1);
        Z = [Q ones(N,1)];

        piVect = b*Z'*inv(Z*Z')

    otherwise

        disp('Method Unknown'); break;

end

return

```

4.7.3 Subroutine to directly calculate puff/spark statistics

```

function [EPD,EIPI,VPD,VIPI,PDDist,IPIDist] = ...
    ...matrixAnalyticPuffStats(Q,piVect,nOpen,kappa,x)

% Function to calculate the distribution, expectation, and variance of
% puff/spark duration and inter-puff/spark interval directly from the
% infinitesimal generator

% INPUT ARGUMENTS

% Q - infinitesimal generator matrix
% piVect - stationary distribution of Q
% nOpen - vector containing the number of open channels in each
% configuration of Q
% kappa - number of open channels at puff start
% x - vector of times at which to calculate the values of the puff/spark
% duration and inter-puff/spark interval distributions

% OUTPUT ARGUMENTS

% EPD - expected puff/spark duration

```

```

% EIPI - expected inter-puff/spark interval
% VPD - variance of puff/spark duration
% VIPI - variance of inter-puff/spark interval
% PDDist - distribution of puff/spark duration
% IPIDist - distribution of inter-puff/spark interval

% Find the indexes of the elements of each aggregate class
O0 = find(nOpen==0);
O1 = find(nOpen==1);
Ok = find(nOpen==kappa);
Os = find(nOpen~=0 & nOpen~=1 & nOpen~=kappa);

% Find the number of elements in each aggregate class
N0 = length(O0);
N1 = length(O1);
Nk = length(Ok);
Ns = length(Os);

% Define commensurate row vectors of zeros
Z0 = zeros(1,N0);
Z1 = zeros(1,N1);
Zk = zeros(1,Nk);
Zs = zeros(1,Ns);

% Permute the generator matrix
newNOpen = [O0; O1; Ok; Os];

Qnew = Q(:,newNOpen); % rearrange columns
Qnew = Qnew(newNOpen,:); % rearrange rows

a = [1 N0+1 N0+N1+1 N0+N1+Nk+1];
b = [N0 N0+N1 N0+N1+Nk N0+N1+Nk+Ns];

Q00 = Qnew(a(1):b(1),a(1):b(1));
Q01 = Qnew(a(1):b(1),a(2):b(2));
Q0k = Qnew(a(1):b(1),a(3):b(3));
Q0s = Qnew(a(1):b(1),a(4):b(4));

Q10 = Qnew(a(2):b(2),a(1):b(1));
Q11 = Qnew(a(2):b(2),a(2):b(2));
Q1k = Qnew(a(2):b(2),a(3):b(3));
Q1s = Qnew(a(2):b(2),a(4):b(4));

Qk0 = Qnew(a(3):b(3),a(1):b(1));
Qk1 = Qnew(a(3):b(3),a(2):b(2));

```

```

Qkk = Qnew(a(3):b(3),a(3):b(3));
Qks = Qnew(a(3):b(3),a(4):b(4));

Qs0 = Qnew(a(4):b(4),a(1):b(1));
Qs1 = Qnew(a(4):b(4),a(2):b(2));
Qsk = Qnew(a(4):b(4),a(3):b(3));
Qss = Qnew(a(4):b(4),a(4):b(4));

% calculate puff/spark duration distribution, expectation, and variance
a01 = piVect(00)*Q01;

g0gk = - [a01 Zs]*inv([Q11 Q1s; Qs1 Qss])*[Q10 Q1k; Qs0 Qsk];
g0 = g0gk(1:NO);
gk = g0gk(NO+1:NO+Nk);

phik = gk/sum(gk);
phiPD = [Z1 phik Zs];

QBB = [Q11 Q1k Q1s; Qk1 Qkk Qks; Qs1 Qsk Qss];
invQBB = inv(QBB);

NB = N1+Nk+Ns;
unos = ones(NB,1);

EPD = -(phiPD*invQBB*unos);
VPD = phiPD*(-invQBB)*(2*eye(NB) - unos*phiPD)*(-invQBB)*unos;

t = QBB*unos;
PDDist = zeros(size(x));
for ii = 1:length(x)
    xnow = x(ii);
    PDDist(ii) = - phiPD * (expm(xnow*QBB)) * t;
end

% calculate inter-puff/spark interval distribution, expectation, and
% variance
g0 = [Z1 gk Zs]*(-invQBB*[Q10; Qk0; Qs0]);

phi0 = g0/sum(g0);
phiIPI = [phi0 Z1 Zs];

QBB = [Q00 Q01 Q0s; Q10 Q11 Q1s; Qs0 Qs1 Qss];
invQBB = inv(QBB);

NB = NO+N1+Ns;

```

```

unos = ones(NB,1);

EIPI = -(phiINI*invQBB*unos);
VIPI = phiIPI*(-invQBB)*(2*eye(NB) - unos*phiIPI)*(-invQBB)*unos;

t = QBB*unos;
IPIDist = zeros(size(x));
for ii = 1:length(x)
    xnow = x(ii);
    IPIDist(ii) = - phiPD * (expm(xnow*QBB)) * t;
end

return

```

4.7.4 Subroutine to map release site configurations to symmetry groups

```

function [B,V,nOpen] = mapstatespace(M,N,nRotSym,nRefSym,iOpen,rot,ref)

% Function to map each of the configuration as a release site model to an
% unique symmetry group using the symmetries of the release site's
% ultrastructure

% INPUT ARGUMENTS

% M - number of states in the single channel model
% N - number of channels at the release site
% nRotSym - degrees of rotational symmetry, e.g., nRotSym=6 for a hexagonal
% lattice
% nRefSym - degrees of reflective symmetry, usually 1;
% iOpen - index of open state

% rot - vector of indeces used to perform a rotation of the release site
% configuration
% ref - vector of indeces used to perform a reflection of the releaes site
% configuration

% Consider the following example:

% Number channels of a haxagonal release site with N=7 as follows:

```

```

%   4 5
%   1 2 3
%   6 7

% and represent an example configuration

%   1 0
%   0 1 1
%   0 0

% where M=2, 0 is closed, and 1 is open as a vector of length N,

% stateNow = [0 0 0 1 1 1 0]

% where stateNow(N-n+1) is the state of channel n.

% The configuration that results after performing a reflection about the
% diagonal through channel 4, 2, and 7 is

%   1 0
%   0 1 0
%   1 0

% stateNext = [0 1 0 1 0 1 0]

% and is arrived at using

% stateNext = stateNow(ref)

% where ref = N - [7 3 1 4 6 2 5] + 1 = [1 5 7 4 2 6 3];

% Similarly, the configuration that result after performing a clockwise
% rotation or 360/nRotSym degrees is given by

%   0 1
%   0 1 0
%   0 1

% stateNext = [1 0 1 0 0 1 0]

% and is arrived at using

% stateNext = stateNow(rot)

% where rot = N - [3 7 4 1 5 2 6] + 1 = [5 1 4 7 3 6 2];

```

```

% OUTPUT ARGUMENTS

% B - number of unique symmetry groups
% V - M^N by B matrix where element i,j = 1 if configuration i belongs to
% symmetry group j
% nOpen - an B by 1 vector where element i is the number of open channels
% in symmetry group i

nStates = M^N;

% allocate space for parsing vectors
sMap = zeros(nStates,1); % all zeros to start - used to keep track of
% states parsed and the state mapping

nOpen = zeros(nStates,1); % all zeros to start - used to keep track of how
% many channels are open in each unique symmetry group

% states are represented in two formats, a base ten number 0 to M^N-1 and a
% base M vector
baseToDecVect = M.^([N-1:-1:0]'); % base M to decimal conversion vector

B = 0; % indexes the unique states as they occur
for stateNow = 0:nStates-1 %

    if sMap(stateNow+1,1) == 0 % current state is a new 'unique' state

        % generate state (base M) representation as a vector
        baseMStateNow = zeros(1,N);
        remainder = stateNow;
        for kk = N:-1:2
            baseMStateNow(1,N+1-kk) = floor(remainder/(M^(kk-1)));
            remainder = mod(remainder,M^(kk-1));
        end
        baseMStateNow(1,N) = remainder;

        B = B+1;
        nOpen(B,1) = length(find(baseMStateNow==iOpen));

        % perform rotations and reflections and map appropriate states to
        % the current unique symmetry group
        for ii = 1:nRefSym
            if ii == 2
                baseMStateNow = baseMStateNow(ref); % reflect;
            end
        end
    end
end

```



```

        for jj = 1:nRotSym
            baseMStateNow = baseMStateNow(rot); % rotate;
            decBaseStateNow = baseMStateNow*baseToDecVect;
            sMap(decBaseStateNow+1,1) = B;
        end
    end
end
end

nOpen = nOpen(1:B,1); % truncate nOpen
sMap = sMap(1:B,1); % truncate sMap

% form V
V = sparse(M^N,B);
for ii = 1:length(sMap)
    V(ii,smap(ii)) = 1;
end

return

```

4.8 Conclusion

The numerical methods above were formulated for the theoretical studies of Chaps. 2 and 3 that use a minimal two-state and a three-state single channel model, respectively. However, these methods can be employed to study more complicated Markov chain models of Ca^{2+} release sites composed of single channel models with any number of states. Similarly, the matrix analytic formulas that express puff/spark duration and inter-puff/spark interval as a function of the Q -matrix (Section 4.4) were formulated to study clusters of Ca^{2+} channels that experience mean-field Ca^{2+} coupling. However, these formulas can also be used to directly calculate puff/spark statistics even when the release site model includes an accurate account of channel positions. The applicability of the numerical methods presented in this chapter to Ca^{2+} release site models other than those of Chaps. 2 and 3 will facilitate future studies of puffs and sparks such as those suggested in the following chapter.

Chapter 5

Epilogue

5.1 Summary of results

This dissertation advances our understanding of the biophysics connecting the microscopic parameters of IP₃R and RyR gating with the emergent phenomena of Ca²⁺ puffs and sparks by clarifying 1) how nearest-neighbor allosteric coupling and Ca²⁺ coupling simultaneously contribute to puff and spark dynamics and 2) how Ca²⁺ inactivation of IP₃Rs and RyRs affects the dynamics of puff/spark generation and termination. For example, the results of Chap. 2 show that when release site models include Ca²⁺ coupling and synchronizing nearest-neighbor allosteric interactions that stabilize closed-closed and/or open-open channel pairs, puff/sparks are always enhanced for some values of the Ca²⁺ coupling strength. Importantly, the range of Ca²⁺ coupling strengths that result in puff/sparks depends on the strength of stabilizing closed-closed and/or open-open allosteric interactions.

Chapter 2 also demonstrates that qualitatively different changes in spark statistics are observed when allosteric interactions that stabilize closed channel pairs, open channel pairs, or both in a balanced fashion are randomly removed from simulations.

It may be possible to combine these simulation results with results of an experimental protocol that involves the gradual washout of the FK-binding proteins necessary for inter-protein allosteric coupling in order to clarify the microscopic parameters of physical coupling *in vivo*. Another interesting result of our simulated washout experiments is that spark statistics are largely insensitive to variations in allosteric connectivity as long as the average allosteric connectivity of the release site remains unchanged.

The results of Chap. 3 demonstrate that high-affinity Ca^{2+} inactivation often facilitates puff/spark termination and, consequently, reduces the sensitivity of stochastic Ca^{2+} excitability to variations of the number of channels at release sites and to variation of the Ca^{2+} coupling strength as long as the rate of Ca^{2+} inactivation is not excessively fast. Interestingly, Ca^{2+} inactivation may be a viable negative control mechanism even if the kinetics of inactivation are much slower than the duration of puffs and sparks. In fact, we found that slow inactivation mechanisms often promote nearly time-reversible puff/sparks by ‘tuning’ release sites so that, at any given time, the number of de-inactivated channels is appropriate to generate robust puff/spark events that terminate without the additional recruitment of inactivated channels.

Chapter 4 presents several numerical methods that facilitated the theoretical studies of Markov chain models of puffs and sparks that are the focus of this dissertation. For example, the vectorized formulation of Gillespie’s method applied to clusters of Ca^{2+} channels coupled via local Ca^{2+} and allosteric interactions (Section 4.2) significantly accelerates the numerical simulation of release sites. The matrix analytic formulas derived to calculate puff/spark duration and inter-event interval distributions directly from infinitesimal generator matrices (Section 4.4) are valuable tools for parameter studies of puff/spark dynamics. Finally, the method for agglomerating release site configurations based on the symmetries of release site ultrastructures may

help researchers cope with the state space explosion that often limits the analysis of Markov chain models of Ca^{2+} release sites [DeRemigio et al., 2008].

5.2 Direction of future work

5.2.1 Markov chain models of calcium channel gating

While this dissertation advances the theory of stochastic Ca^{2+} excitability, much work remains to clarify the biophysics of puff and spark dynamics. For example, the results of this manuscript assume that Ca^{2+} release sites are composed of homogeneous clusters of channels, that is, individual channels are modeled using identical state-transition diagrams. However, multiple IP_3R and RyR isoforms with different functional properties—that is, varying single channel gating dynamics—are often co-expressed in cells [Miyakawa et al., 1999, Fill and Copello, 2002]. Thus, release sites may be composed of heterogeneous collections of channels. Theoretical models may help clarify the functional consequences of this heterogeneity.

Another limitation of the studies of Ca^{2+} puffs and sparks presented in this dissertation is that the single channel models used do not explicitly include transitions representing the binding of co-agonists, such as the binding of IP_3 to IP_3Rs and cyclic ADP-ribose to RyRs [Berridge, 1993a, Berridge, 1998]. Instead, it is assumed that channels gate under the influence of a constant or saturating concentration of such co-agonists. While such an assumption may be valid when the production of co-agonist is slow compared to the gating of channels, it is not when changes in the co-agonist concentrations occur on the same time scale of puffs and sparks. Future theoretical studies of puffs and sparks may need to include an accurate account of co-agonist binding. Such an account will be necessary in order to incorporate release site models

into models of signal transduction pathways that include the hydrolysis of IP₃R and RyR co-agonists via G-protein coupled cascades [Berridge, 1993a, Berridge, 1998].

The results of this manuscript also assumes that the kinetics of single channel gating obey the law of mass action. That is, Ca²⁺-dependent transition rates are expressed as functions of the [Ca²⁺]. However, this formulation may not be valid when the [Ca²⁺] is low and the stochastic motion of individual Ca²⁺ ions is relevant. In the low [Ca²⁺] limit, it may be necessary to model intracellular Ca²⁺ as individual ions undergoing Brownian motion instead of using continuous functions of space and time. Such a modeling approach may especially be important for studying the stochastic gating of RyRs in cardiac ventricular myocytes where clusters of channels occur in small regions of the cytosol located between the plasma and SR membranes. The volume of these so-called diadic spaces may only be a few tens of atto liters (atto = 10⁻¹⁹) [Koh et al., 2006] and, thus, it is likely that only one or two free Ca²⁺ ions are present in each diadic space at resting Ca²⁺ concentrations [Koh et al., 2006].

An interesting study would compare the dynamics of Ca²⁺ channel gating when the Ca²⁺ microdomain is modeled using continuous differential equations to the dynamics when the local Ca²⁺ profile is modeled as discrete Ca²⁺ ions undergoing Brownian motion. Because as much as 90% of Ca²⁺ in the diadic space is bound to mobile and immobile buffers, an extension of this work could investigate the effects of Ca²⁺ buffering on channel gating when Ca²⁺ is modeled discretely. The rapid binding and unbinding of Ca²⁺ to buffers may be functionally similar to the limit where the diffusion of Ca²⁺ is much faster than channel gating. Thus the Ca²⁺ profile in the presence of buffers may be well approximated by continuous functions even when the concentration of free Ca²⁺ is low.

5.2.2 Calcium release via the polycystic 2 ion channel

Recently, it has come to light that IP₃Rs and RyRs are not the only Ca²⁺ channels responsible for mediating Ca²⁺ release from the ER/SR. The polycystic 2 (PC2) ion channel protein, also known as the TRPP2 (transient receptor potential polycystic 2) channel, is known to be localized on the ER and SR membrane of many types of cells including kidney, heart, and brain cells [Anyatonwu and Ehrlich, 2004, Bootman et al., 2002, Anyatonwu et al., 2007]. Like many RyRs and IP₃Rs isoforms, PC2 is activated at low cytosolic Ca²⁺ concentrations and inactivated at higher Ca²⁺ concentrations [Anyatonwu and Ehrlich, 2004, Bootman et al., 2002]. While much experimental work remains to clarify the dynamics of PC2 gating and the distribution of PC2 on ER/SR membranes, it is at least plausible that these channels colocalize with IP₃Rs and RyRs at Ca²⁺ release sites. Polycystic 2 has already been shown to coimmunoprecipitate with type 2 RyRs in mouse heart and inhibit RyR channel activity in the presence of Ca²⁺ [Anyatonwu et al., 2007]. Furthermore, the amplitude of RyR release decreases and the duration increases in the absence of PC2 [Anyatonwu et al., 2007]. These results indicate that future models of localized Ca²⁺ release may need to account for PC2 channels. More importantly, the emergence of PC2 as an agent of intracellular Ca²⁺ release reminds us that the state of the art is constantly changing and much work remains to elucidate the theory of localized Ca²⁺ release.

5.3 Local calcium release and studies of global calcium signals

In addition to advancing our understanding of localized Ca²⁺ release, the studies of this dissertation are important because models of global Ca²⁺ release may ulti-

mately depend on an accurate account of local Ca^{2+} signaling events such as puffs and sparks. Models of global Ca^{2+} signaling that ignore local signaling often fail to reproduce salient features of Ca^{2+} release. For example, models such as the De Young-Keizer model of Ca^{2+} oscillations neglect spatial aspects of the Ca^{2+} profile and instead, assume “continuously-stirred” single cytosolic and ER Ca^{2+} pools [De Young and Keizer, 1992]. When this common pool approach is used in models of cardiac excitation-contraction (EC) coupling, the phenomenon of high gain release—where a small influx of Ca^{2+} via L-type channels recruits a much larger release of Ca^{2+} from the SR via RyRs—is readily observed. However, such models are unable to robustly reproduce the phenomenon of graded Ca^{2+} release in which the amplitude of the Ca^{2+} signal is a function of the amount of ‘trigger’ Ca^{2+} that enters via L-type channels [Stern, 1992b, Hilgemann and Noble, 1987]. In contrast to common pool models, models of whole cell EC coupling that include a representation of individual Ca^{2+} release sites are able to reproduce both gain and graded release of Ca^{2+} [Stern, 1992b, Williams et al., 2007, Rice et al., 1999, Sobie et al., 2002, Greenstein and Winslow, 2002].

The example of EC coupling suggests that many global Ca^{2+} signals can only be successfully modeled when theorists consider how these global signals emerge from the underlying local Ca^{2+} signaling events. In fact, local variations of Ca^{2+} signals may ultimately prove to be the functionally significant component of many global Ca^{2+} release events. This seems especially plausible in the arena of neuronal information processing. For example, Purkinje neurons of the cerebellum have arborous dendrites that integrate synaptic inputs from thousands of afferent axons. Many of these synapses occur on small protruding sections of the dendritic membrane referred to as dendritic spines. Because they contain a projection of the ER membrane on which IP_3Rs are expressed, input specific Ca^{2+} microdomains may be established

within the relatively isolated cytosol of dendritic spines [Sharp et al., 1993]. In fact, localized Ca^{2+} release within dendritic spines may allow spines to function as coincidence detectors. Recall that IP_3 Rs are activated when both Ca^{2+} and IP_3 are present. Calcium may enter spines when the entire dendritic membrane is depolarized by axons referred to as climbing fibers. However, IP_3 is hydrolyzed only when spine-specific parallel fibers are recruited [Sharp et al., 1993, Berridge, 1998].

Hopefully, the examples given above illustrate that future realistic models of global Ca^{2+} release will often need to include an accurate account of the localized Ca^{2+} release events from which they emerge. Thus, the theoretical models of local Ca^{2+} release presented in this manuscript are essential. Not only do they help to clarify the biophysics connecting microscopic parameters of channel gating to Ca^{2+} puff and spark dynamics, they also establish a foundation on which whole cell models of Ca^{2+} release can be built.

Afterword

The work discussed in this dissertation has resulted in several presentations at international conferences and the submission of two articles for publication in peer reviewed journals. The first article, titled “Ryanodine receptor allosteric coupling and the dynamics of calcium sparks”, was submitted to *Biophysical Journal* and is primarily based on the results of Chap. 2. The second article, titled “Calcium-dependent inactivation and the dynamics of calcium puffs and sparks”, was submitted to *The Journal of Theoretical Biology* and is based on the work of Chap. 3. Both manuscripts are currently under review.

My research has also contributed to an article recently submitted to the journal *Mathematical Medicine and Biology* by lead author Hilary DeRemigio titled “Calcium release site ultrastructure and the dynamics of puffs and sparks.” My primary contribution to this work was the formulation of a vectorized algorithm used to numerically simulate Ca^{2+} release sites. The simulation algorithm is similar to that of Section 4.2, but does not include a representation of nearest neighbor allosteric coupling. I also contributed by writing code to facilitate numerical estimation of puff/spark statistics from Monte Carlo simulations.

During my first two years at William & Mary, I also contributed to computational studies of the thalamic visual pathways. These studies are not discussed in this dissertation, but they are significant contributions and deserve to be mentioned. Briefly,

visual information from the retina passes through the visual thalamus (lateral geniculate nucleus, dLGN) on its way to cortex. While it was thought until recently that the dLGN was essentially a passive relay for this information, it is now apparent that the dLGN acts as a state-dependent gateway, controlling the flow of visual information from the periphery to the cortex [McCormick and Bal, 1997]. The filter properties of this gateway are modulated by inputs from a host of non-retinal sources such as the thalamic reticular nucleus (perigeniculate nucleus, PGN), the brain stem, and layer six of visual cortex [McCormick and Bal, 1997, Cudeiro and Sillito, 2006]. Importantly, the principle neurons of the dLGN, thalamocortical relay neurons, express the low voltage activated Ca^{2+} current (T-type Ca^{2+} current) responsible for bursts of action potentials [Destexhe and Sejnowski, 2003]. Thus, inhibitory input to the thalamocortical relay neurons may significantly alter the information content of visual information as it passes through the thalamus [McCormick and Bal, 1997, Cudeiro and Sillito, 2006].

Using ordinary differential equation models of the relevant neural network and spectral analysis techniques, we studied the effects of feedback inhibition from reticular neurons of the PGN on the transmission of retinal drive through the dLGN. We found that that the filter properties of the dLGN/PGN are dependent on the temporal and spatial frequency of retinal drive in addition to the level of potassium leak conductance (a correlate in our model to level of arousal). This work resulted in two publications. The first titled “The effect of feedback inhibition on throughput properties of the dorsal lateral geniculate nucleus” appeared in *Neurocomputing* in 2005 [Huertas et al., 2005a]. The second titled “feedback inhibition and throughput properties of an integrate-and-fire-or-burst network model of retinogeniculate transmission” appeared in *The Journal of Computational Neuroscience* in 2006 [Huertas et al., 2005b]. Numerous presentations at international conferences also resulted from

this work.

I have also used information theoretical techniques such as stimulus reconstruction and mutual information to study the throughput properties of a model dLGN network that includes interneuron feed-forward inhibition [Cox and Sherman, 2000, Cox et al., 2003, Govindaiah and Cox, 2004]. While this work has not resulted in a publication, results of these studies have been presented in abstract form as “The effect of interneuron feed-forward inhibition on linear stimulus reconstruction” at the Society for Neuroscience and Computational Neuroscience annual meetings in 2005.

Bibliography

- [Allbritton et al., 1992] Allbritton, N. L., Meyer, T., and Stryer, L. (1992). Range of messenger action of calcium ion and inositol 1,4,5-trisphosphate. *Science*, 258(5089):1812–5.
- [Anyatonwu and Ehrlich, 2004] Anyatonwu, G. I. and Ehrlich, B. E. (2004). Calcium signaling and polycystin-2. *Biochem. Biophys. Res. Commun.*, 322(4):1364–73.
- [Anyatonwu et al., 2007] Anyatonwu, G. I., Estrada, M., Tian, X., Somlo, S., and Ehrlich, B. E. (2007). Regulation of ryanodine receptor-dependent calcium signaling by polycystin-2. *Proc. Natl. Acad. Sci. U.S.A.*, 104(15):6454–9.
- [Augustine et al., 1985] Augustine, G. J., Charlton, M. P., and Smith, S. J. (1985). Calcium entry into voltage-clamped presynaptic terminals of squid. *J. Physiol. (Lond.)*, 367:143–62.
- [Augustine et al., 2003] Augustine, G. J., Santamaria, F., and Tanaka, K. (2003). Local calcium signaling in neurons. *Neuron*, 40(2):331–46.
- [Ball and Geoffrey, 2000] Ball, F. and Geoffrey, Y. (2000). Superposition of Spatially Interacting Aggregated Continuous Time Markov Chains. *Methodology of Computing in Applied Probability*, 2(1):93–116.

- [Ball et al., 2000] Ball, F. G., Milne, R. K., and Yeo, G. F. (2000). Stochastic models for systems of interacting ion channels. *IMA journal of mathematics applied in medicine and biology*, 17(3):263–93.
- [Berridge, 1993a] Berridge, M. J. (1993a). Cell signalling. A tale of two messengers. *Nature*, 365(6445):388–9.
- [Berridge, 1993b] Berridge, M. J. (1993b). Inositol trisphosphate and calcium signalling. *Nature*, 361(6410):315–25.
- [Berridge, 1997] Berridge, M. J. (1997). Elementary and global aspects of calcium signalling. *J. Physiol. (Lond.)*, 499 (Pt 2):291–306.
- [Berridge, 1998] Berridge, M. J. (1998). Neuronal calcium signaling. *Neuron*, 21(1):13–26.
- [Berridge, 2005] Berridge, M. J. (2005). Unlocking the secrets of cell signaling. *Annu. Rev. Physiol.*, 67:1–21.
- [Berridge, 2006] Berridge, M. J. (2006). Calcium microdomains: organization and function. *Cell Calcium*, 40(5-6):405–12.
- [Berridge et al., 1998] Berridge, M. J., Bootman, M. D., and Lipp, P. (1998). Calcium—a life and death signal. *Nature*, 395(6703):645–8.
- [Berridge et al., 2003] Berridge, M. J., Bootman, M. D., and Roderick, H. L. (2003). Calcium signalling: dynamics, homeostasis and remodelling. *Nat. Rev. Mol. Cell Biol.*, 4(7):517–29.
- [Bers, 2002] Bers, D. M. (2002). Cardiac excitation-contraction coupling. *Nature*, 415(6868):198–205.

- [Bers and Guo, 2005] Bers, D. M. and Guo, T. (2005). Calcium signaling in cardiac ventricular myocytes. *Ann. N. Y. Acad. Sci.*, 1047:86–98.
- [Bezprozvanny, 2005] Bezprozvanny, I. (2005). The inositol 1,4,5-trisphosphate receptors. *Cell Calcium*, 38(3-4):261–72.
- [Bezprozvanny and Ehrlich, 1994] Bezprozvanny, I. and Ehrlich, B. E. (1994). Inositol (1,4,5)-trisphosphate (InsP₃)-gated Ca channels from cerebellum: conduction properties for divalent cations and regulation by intraluminal calcium. *J. Gen. Physiol.*, 104(5):821–56.
- [Bezprozvanny et al., 1991] Bezprozvanny, I., Watras, J., and Ehrlich, B. E. (1991). Bell-shaped calcium-response curves of Ins(1,4,5)P₃- and calcium-gated channels from endoplasmic reticulum of cerebellum. *Nature*, 351(6329):751–4.
- [Biden et al., 1984] Biden, T. J., Prentki, M., Irvine, R. F., Berridge, M. J., and Wollheim, C. B. (1984). Inositol 1,4,5-trisphosphate mobilizes intracellular Ca²⁺ from permeabilized insulin-secreting cells. *Biochem. J.*, 223(2):467–73.
- [Bootman et al., 2002] Bootman, M. D., Berridge, M. J., and Roderick, H. L. (2002). Calcium signalling: more messengers, more channels, more complexity. *Curr. Biol.*, 12(16):R563–5.
- [Bootman et al., 2001a] Bootman, M. D., Collins, T. J., Peppiatt, C. M., Prothero, L. S., MacKenzie, L., Smet, P. D., Travers, M., Tovey, S. C., Seo, J. T., Berridge, M. J., Ciccolini, F., and Lipp, P. (2001a). Calcium signalling—an overview. *Semin Cell Dev Biol*, 12(1):3–10.
- [Bootman et al., 2001b] Bootman, M. D., Lipp, P., and Berridge, M. J. (2001b). The organisation and functions of local Ca²⁺ signals. *J Cell Sci*, 114(Pt 12):2213–22.

- [Cannell et al., 1995] Cannell, M. B., Cheng, H., and Lederer, W. J. (1995). The control of calcium release in heart muscle. *Science*, 268(5213):1045–9.
- [Cheng et al., 1996] Cheng, H., Lederer, M. R., Lederer, W. J., and Cannell, M. B. (1996). Calcium sparks and $[Ca^{2+}]_i$ waves in cardiac myocytes. *Am. J. Physiol.*, 270(1 Pt 1):C148–59.
- [Cheng et al., 1993] Cheng, H., Lederer, W. J., and Cannell, M. B. (1993). Calcium sparks: elementary events underlying excitation-contraction coupling in heart muscle. *Science*, 262(5134):740–4.
- [Colquhoun and Hawkes, 1995] Colquhoun, D. and Hawkes, A. (1995). A Q-matrix cookbook: how to write only one program to calculate the single-channel and macroscopic predictions for any kinetic mechanism. In Sakmann, B. and Neher, E., editors, *Single-Channel Recording*, pages 589–633. Plenum Press, New York.
- [Connor and Ahmed, 1984] Connor, J. A. and Ahmed, Z. (1984). Diffusion of ions and indicator dyes in neural cytoplasm. *Cell Mol Neurobiol*, 4(1):53–66.
- [Cox et al., 2003] Cox, C. L., Reichova, I., and Sherman, S. M. (2003). Functional synaptic contacts by intranuclear axon collaterals of thalamic relay neurons. *J Neurosci*, 23(20):7642–6.
- [Cox and Sherman, 2000] Cox, C. L. and Sherman, S. M. (2000). Control of dendritic outputs of inhibitory interneurons in the lateral geniculate nucleus. *Neuron*, 27(3):597–610.
- [Crowder et al., 2007] Crowder, E. A., Saha, M. S., Pace, R. W., Zhang, H., Prestwich, G. D., and Del Negro, C. A. (2007). Phosphatidylinositol 4,5-bisphosphate

- regulates inspiratory burst activity in the neonatal mouse preBötzinger complex. *J. Physiol. (Lond.)*, 582(Pt 3):1047–58.
- [Cudeiro and Sillito, 2006] Cudeiro, J. and Sillito, A. M. (2006). Looking back: corticothalamic feedback and early visual processing. *Trends Neurosci*, 29(6):298–306.
- [De Young and Keizer, 1992] De Young, G. W. and Keizer, J. (1992). A single-pool inositol 1,4,5-trisphosphate-receptor-based model for agonist-stimulated oscillations in Ca^{2+} concentration. *Proc. Natl. Acad. Sci. U.S.A.*, 89(20):9895–9.
- [Del Negro et al., 2005] Del Negro, C. A., Morgado-Valle, C., Hayes, J. A., Mackay, D. D., Pace, R. W., Crowder, E. A., and Feldman, J. L. (2005). Sodium and calcium current-mediated pacemaker neurons and respiratory rhythm generation. *J Neurosci*, 25(2):446–53.
- [DeRemigio et al., 2007] DeRemigio, H., Groff, J., and Smith, G. (2007). The spatial organization of calcium release sites and the dynamics of puffs and sparks. In *Biophysical Society Annual Meeting Abstracts, Program No. 1211*, Baltimore, MD.
- [DeRemigio et al., 2008] DeRemigio, H., Kemper, P., LaMar, M., and Smith, G. (2008). Markov chain models of coupled intracellular calcium channels: Kronecker structured representations and benchmark stationary distribution calculations. *2008 Proceedings of the Pacific Symposium on Biocomputing (in press)*.
- [DeRemigio and Smith, 2007] DeRemigio, H. and Smith, G. (2007). Calcium release site ultrastructure and the dynamics of puffs and sparks. *Math. Med. and Biol. (in press)*.

- [DeRemigio and Smith, 2005] DeRemigio, H. and Smith, G. D. (2005). The dynamics of stochastic attrition viewed as an absorption time on a terminating Markov chain. *Cell Calcium*, 38(2):73–86.
- [Destexhe and Sejnowski, 2003] Destexhe, A. and Sejnowski, T. J. (2003). Interactions between membrane conductances underlying thalamocortical slow-wave oscillations. *Physiol. Rev.*, 83(4):1401–53.
- [Diambra and Guisoni, 2005] Diambra, L. and Guisoni, N. (2005). Modeling stochastic Ca^{2+} release from a cluster of IP_3 -sensitive receptors. *Cell Calcium*, 37(4):321–32.
- [Duke and Bray, 1999] Duke, T. A. and Bray, D. (1999). Heightened sensitivity of a lattice of membrane receptors. *Proc. Natl. Acad. Sci. U.S.A.*, 96(18):10104–8.
- [Duke et al., 2001] Duke, T. A., Novère, N. L., and Bray, D. (2001). Conformational spread in a ring of proteins: a stochastic approach to allostery. *J Mol Biol*, 308(3):541–53.
- [Fabiato, 1985] Fabiato, A. (1985). Time and calcium dependence of activation and inactivation of calcium-induced release of calcium from the sarcoplasmic reticulum of a skinned canine cardiac Purkinje cell. *J. Gen. Physiol.*, 85(2):247–89.
- [Falke et al., 1994] Falke, J. J., Drake, S. K., Hazard, A. L., and Peersen, O. B. (1994). Molecular tuning of ion binding to calcium signaling proteins. *Q Rev Biophys*, 27(3):219–90.
- [Fernández-Chacón et al., 2001] Fernández-Chacón, R., Königstorfer, A., Gerber, S. H., García, J., Matos, M. F., Stevens, C. F., Brose, N., Rizo, J., Rosenmund,

- C., and Südhof, T. C. (2001). Synaptotagmin I functions as a calcium regulator of release probability. *Nature*, 410(6824):41–9.
- [Fill, 2002] Fill, M. (2002). Mechanisms that turn-off intracellular calcium release channels. *Front. Biosci.*, 8:d46–54.
- [Fill and Copello, 2002] Fill, M. and Copello, J. A. (2002). Ryanodine receptor calcium release channels. *Physiol. Rev.*, 82(4):893–922.
- [Foskett et al., 2007] Foskett, J. K., White, C., Cheung, K.-H., and Mak, D.-O. D. (2007). Inositol trisphosphate receptor Ca^{2+} release channels. *Physiol. Rev.*, 87(2):593–658.
- [Fraiman and Dawson, 2004] Fraiman, D. and Dawson, S. P. (2004). A model of IP_3 receptor with a luminal calcium binding site: stochastic simulations and analysis. *Cell Calcium*, 35(5):403–13.
- [Franzini-Armstrong et al., 1999a] Franzini-Armstrong, C., Protasi, F., and Ramesh, V. (1999a). Comparative ultrastructure of Ca^{2+} release units in skeletal and cardiac muscle. *Ann. N. Y. Acad. Sci.*, 853:20–30.
- [Franzini-Armstrong et al., 1999b] Franzini-Armstrong, C., Protasi, F., and Ramesh, V. (1999b). Shape, size, and distribution of Ca^{2+} release units and couplons in skeletal and cardiac muscles. *Biophys. J.*, 77(3):1528–39.
- [Gabso et al., 1997] Gabso, M., Neher, E., and Spira, M. E. (1997). Low mobility of the Ca^{2+} buffers in axons of cultured *Aplysia* neurons. *Neuron*, 18(3):473–81.
- [Gillespie, 1976] Gillespie, D. T. (1976). A general method for numerically simulating the stochastic time evolution of coupled chemical reactions. *Journal of Computational Physics*, 22:403–34.

- [Gómez et al., 2004] Gómez, A. M., Schuster, I., Fauconnier, J., Prestle, J., Hasenfuss, G., and Richard, S. (2004). FKBP12.6 overexpression decreases Ca^{2+} spark amplitude but enhances $[\text{Ca}^{2+}]_i$ transient in rat cardiac myocytes. *Am J Physiol Heart Circ Physiol*, 287(5):H1987–93.
- [Govindaiah and Cox, 2004] Govindaiah and Cox, C. L. (2004). Synaptic activation of metabotropic glutamate receptors regulates dendritic outputs of thalamic interneurons. *Neuron*, 41(4):611–23.
- [Greenstein and Winslow, 2002] Greenstein, J. L. and Winslow, R. L. (2002). An integrative model of the cardiac ventricular myocyte incorporating local control of Ca^{2+} release. *Biophys. J.*, 83(6):2918–45.
- [Groff and Smith, 2007a] Groff, J. and Smith, G. (2007a). A computational investigation of the effects of allosteric coupling between ryanodine receptors on the dynamics of calcium sparks. In *Biophysical Society Annual Meeting Abstracts, Program No. 1209*, Baltimore, MD.
- [Groff and Smith, 2007b] Groff, J. and Smith, G. (2007b). Ryanodine receptor allosteric coupling and the dynamics of calcium sparks. *Biophys. J. (in press)*.
- [Györke and Györke, 1998] Györke, I. and Györke, S. (1998). Regulation of the cardiac ryanodine receptor channel by luminal Ca^{2+} involves luminal Ca^{2+} sensing sites. *Biophys. J.*, 75(6):2801–10.
- [Györke, 1999] Györke, S. (1999). Ca^{2+} spark termination: inactivation and adaptation may be manifestations of the same mechanism. *J. Gen. Physiol.*, 114(1):163–6.

- [Györke and Fill, 1993] Györke, S. and Fill, M. (1993). Ryanodine receptor adaptation: control mechanism of Ca^{2+} -induced Ca^{2+} release in heart. *Science*, 260(5109):807–9.
- [Hagar et al., 1998] Hagar, R. E., Burgstahler, A. D., Nathanson, M. H., and Ehrlich, B. E. (1998). Type III InsP_3 receptor channel stays open in the presence of increased calcium. *Nature*, 396(6706):81–4.
- [Hilgemann and Noble, 1987] Hilgemann, D. W. and Noble, D. (1987). Excitation-contraction coupling and extracellular calcium transients in rabbit atrium: reconstruction of basic cellular mechanisms. *Proc R Soc Lond, B, Biol Sci*, 230(1259):163–205.
- [Hill, 1989] Hill (1989). *Free Energy Transduction in Biology and Biochemical Cycle Kinetics*. Springer-Verlag.
- [Hille, 2001] Hille, B. (2001). *Ionic Channels of Excitable Membranes, 3rd edition*. Sinauer Associates, Sunderland, MA.
- [Hinch, 2004] Hinch, R. (2004). A mathematical analysis of the generation and termination of calcium sparks. *Biophys. J.*, 86(3):1293–307.
- [Huertas et al., 2005a] Huertas, M., Groff, J., and Smith, G. (2005a). The effect of feedback inhibition on throughput properties of the dorsal lateral geniculate nucleus. *Neurocomputing*, 65-66:499–505.
- [Huertas et al., 2005b] Huertas, M. A., Groff, J. R., and Smith, G. D. (2005b). Feedback inhibition and throughput properties of an integrate-and-fire-or-burst network model of retinogeniculate transmission. *Journal of computational neuroscience*, 19(2):147–80.

- [Huertas and Smith, 2007] Huertas, M. A. and Smith, G. D. (2007). The dynamics of luminal depletion and the stochastic gating of Ca^{2+} -activated Ca^{2+} channels and release sites. *J Theor Biol*, 246(2):332–54.
- [Ji et al., 2004] Ji, G., Feldman, M. E., Greene, K. S., Sorrentino, V., Xin, H.-B., and Kotlikoff, M. I. (2004). RYR2 proteins contribute to the formation of Ca^{2+} sparks in smooth muscle. *J. Gen. Physiol.*, 123(4):377–86.
- [Jiang et al., 2004] Jiang, D., Qian, M., and Qian, M. (2004). *Mathematical Theory of Nonequilibrium Steady States*. Springer, Berlin.
- [Keizer, 1987] Keizer, J. (1987). *Statistical Thermodynamics of Nonequilibrium Processes*. Springer Verlag, Berlin.
- [Keizer and Levine, 1996] Keizer, J. and Levine, L. (1996). Ryanodine receptor adaptation and Ca^{2+} -induced Ca^{2+} release-dependent Ca^{2+} oscillations. *Biophys. J.*, 71(6):3477–87.
- [Kettlun et al., 2003] Kettlun, C., González, A., Ríos, E., and Fill, M. (2003). Unitary Ca^{2+} current through mammalian cardiac and amphibian skeletal muscle ryanodine receptor Channels under near-physiological ionic conditions. *J. Gen. Physiol.*, 122(4):407–17.
- [Kirichok et al., 2004] Kirichok, Y., Krapivinsky, G., and Clapham, D. E. (2004). The mitochondrial calcium uniporter is a highly selective ion channel. *Nature*, 427(6972):360–4.
- [Koh et al., 2006] Koh, X., Srinivasan, B., Ching, H. S., and Levchenko, A. (2006). A 3D Monte Carlo analysis of the role of dyadic space geometry in spark generation. *Biophys. J.*, 90(6):1999–2014.

- [Lai et al., 1989] Lai, F. A., Misra, M., Xu, L., Smith, H. A., and Meissner, G. (1989). The ryanodine receptor-Ca²⁺ release channel complex of skeletal muscle sarcoplasmic reticulum. Evidence for a cooperatively coupled, negatively charged homotrimer. *J. Biol. Chem.*, 264(28):16776–85.
- [Lehnart et al., 2004a] Lehnart, S. E., Wehrens, X. H. T., Kushnir, A., and Marks, A. R. (2004a). Cardiac ryanodine receptor function and regulation in heart disease. *Ann. N. Y. Acad. Sci.*, 1015:144–59.
- [Lehnart et al., 2004b] Lehnart, S. E., Wehrens, X. H. T., and Marks, A. R. (2004b). Calstabin deficiency, ryanodine receptors, and sudden cardiac death. *Biochem. Biophys. Res. Commun.*, 322(4):1267–79.
- [Lipp and Niggli, 1998] Lipp, P. and Niggli, E. (1998). Fundamental calcium release events revealed by two-photon excitation photolysis of caged calcium in Guinea-pig cardiac myocytes. *J. Physiol. (Lond.)*, 508 (Pt 3):801–9.
- [Lukyanenko et al., 1998] Lukyanenko, V., Wiesner, T. F., and Gyorke, S. (1998). Termination of Ca²⁺ release during Ca²⁺ sparks in rat ventricular myocytes. *J. Physiol. (Lond.)*, 507 (Pt 3):667–77.
- [Mak and Foskett, 1997] Mak, D. O. and Foskett, J. K. (1997). Single-channel kinetics, inactivation, and spatial distribution of inositol trisphosphate (IP₃) receptors in *Xenopus* oocyte nucleus. *J. Gen. Physiol.*, 109(5):571–87.
- [Marchant and Parker, 2000] Marchant, J. S. and Parker, I. (2000). Functional interactions in Ca²⁺ signaling over different time and distance scales. *J. Gen. Physiol.*, 116(5):691–6.

- [Marchant and Taylor, 1998] Marchant, J. S. and Taylor, C. W. (1998). Rapid activation and partial inactivation of inositol trisphosphate receptors by inositol trisphosphate. *Biochemistry*, 37(33):11524–33.
- [Marx et al., 2001] Marx, S. O., Gaburjakova, J., Gaburjakova, M., Henrikson, C., Ondrias, K., and Marks, A. R. (2001). Coupled gating between cardiac calcium release channels (ryanodine receptors). *Circ. Res.*, 88(11):1151–8.
- [Marx et al., 1998] Marx, S. O., Ondrias, K., and Marks, A. R. (1998). Coupled gating between individual skeletal muscle Ca^{2+} release channels (ryanodine receptors). *Science*, 281(5378):818–21.
- [Marx et al., 2000] Marx, S. O., Reiken, S., Hisamatsu, Y., Jayaraman, T., Burkhoff, D., Rosemblyt, N., and Marks, A. R. (2000). PKA phosphorylation dissociates FKBP12.6 from the calcium release channel (ryanodine receptor): defective regulation in failing hearts. *Cell*, 101(4):365–76.
- [Mazzag et al., 2005] Mazzag, B., Tignanelli, C. J., and Smith, G. D. (2005). The effect of residual Ca^{2+} on the stochastic gating of Ca^{2+} -regulated Ca^{2+} channel models. *J Theor Biol*, 235(1):121–50.
- [McCall et al., 1996] McCall, E., Li, L., Satoh, H., Shannon, T. R., Blatter, L. A., and Bers, D. M. (1996). Effects of FK-506 on contraction and Ca^{2+} transients in rat cardiac myocytes. *Circ Res*, 79(6):1110–21.
- [McCormick and Bal, 1997] McCormick, D. A. and Bal, T. (1997). Sleep and arousal: thalamocortical mechanisms. *Annu Rev Neurosci*, 20:185–215.

- [Mejía-Alvarez et al., 1999] Mejía-Alvarez, R., Kettlun, C., Ríos, E., Stern, M., and Fill, M. (1999). Unitary Ca^{2+} current through cardiac ryanodine receptor channels under quasi-physiological ionic conditions. *J. Gen. Physiol.*, 113(2):177–86.
- [Miyakawa et al., 1999] Miyakawa, T., Maeda, A., Yamazawa, T., Hirose, K., Kurosaki, T., and Iino, M. (1999). Encoding of Ca^{2+} signals by differential expression of IP_3 receptor subtypes. *EMBO J.*, 18(5):1303–8.
- [Moraru et al., 1999] Moraru, I. I., Kaftan, E. J., Ehrlich, B. E., and Watras, J. (1999). Regulation of type 1 inositol 1,4,5-trisphosphate-gated calcium channels by InsP_3 and calcium: Simulation of single channel kinetics based on ligand binding and electrophysiological analysis. *J. Gen. Physiol.*, 113(6):837–49.
- [Murayama and Ogawa, 1996] Murayama, T. and Ogawa, Y. (1996). Properties of Ryr3 ryanodine receptor isoform in mammalian brain. *J. Biol. Chem.*, 271(9):5079–84.
- [Naraghi and Neher, 1997] Naraghi, M. and Neher, E. (1997). Linearized buffered Ca^{2+} diffusion in microdomains and its implications for calculation of $[\text{Ca}^{2+}]$ at the mouth of a calcium channel. *J. Neurosci.*, 17(18):6961–73.
- [Neher, 1986] Neher, E. (1986). Concentration profiles of intracellular calcium in the presence of diffusible chelator. *Experimental Brain Research, Series 14*.
- [Neher, 1998] Neher, E. (1998). Usefulness and limitations of linear approximations to the understanding of Ca^{++} signals. *Cell Calcium*, 24(5-6):345–57.
- [Neher and Almers, 1986a] Neher, E. and Almers, W. (1986a). Fast calcium transients in rat peritoneal mast cells are not sufficient to trigger exocytosis. *EMBO J.*, 5(1):51–3.

- [Neher and Almers, 1986b] Neher, E. and Almers, W. (1986b). Patch pipettes used for loading small cells with fluorescent indicator dyes. *Adv Exp Med Biol*, 211:1–5.
- [Neher and Augustine, 1992] Neher, E. and Augustine, G. J. (1992). Calcium gradients and buffers in bovine chromaffin cells. *J. Physiol. (Lond.)*, 450:273–301.
- [Nguyen et al., 2005] Nguyen, V., Mathias, R., and Smith, G. D. (2005). A stochastic automata network descriptor for Markov chain models of instantaneously coupled intracellular Ca^{2+} channels. *Bull. Math. Biol.*, 67(3):393–432.
- [Nicola, 1998] Nicola, V. (1998). Lumping in markov reward processes. Technical report, RC14719, IBM Thomas Watson Research Centre, P.O. Box 704, Yorktown Heights, NY 10598.
- [Niggli, 1999] Niggli, E. (1999). Localized intracellular calcium signaling in muscle: calcium sparks and calcium quarks. *Annu. Rev. Physiol.*, 61:311–35.
- [Niggli and Shirokova, 2007] Niggli, E. and Shirokova, N. (2007). A guide to sparkology: the taxonomy of elementary cellular Ca^{2+} signaling events. *Cell Calcium*, 42(4-5):379–87.
- [Norris, 1997] Norris, J. (1997). *Markov chains*. Cambridge University Press, Cambridge.
- [Pace et al., 2007] Pace, R. W., Mackay, D. D., Feldman, J. L., and Del Negro, C. A. (2007). Role of persistent sodium current in mouse preBötzing Complex neurons and respiratory rhythm generation. *J. Physiol. (Lond.)*, 580(Pt. 2):485–96.
- [Parker et al., 1996a] Parker, I., Choi, J., and Yao, Y. (1996a). Elementary events of InsP_3 -induced Ca^{2+} liberation in *Xenopus* oocytes: hot spots, puffs and blips. *Cell Calcium*, 20(2):105–21.

- [Parker and Ivorra, 1990] Parker, I. and Ivorra, I. (1990). Inhibition by Ca^{2+} of inositol trisphosphate-mediated Ca^{2+} liberation: a possible mechanism for oscillatory release of Ca^{2+} . *Proc. Natl. Acad. Sci. U.S.A.*, 87(1):260–4.
- [Parker and Yao, 1996] Parker, I. and Yao, Y. (1996). Ca^{2+} transients associated with openings of inositol trisphosphate-gated channels in *Xenopus* oocytes. *J. Physiol. (Lond.)*, 491 (Pt 3):663–8.
- [Parker et al., 1996b] Parker, I., Yao, Y., and Ilyin, V. (1996b). Fast kinetics of calcium liberation induced in *Xenopus* oocytes by photoreleased inositol trisphosphate. *Biophys. J.*, 70(1):222–37.
- [Payne et al., 1986] Payne, R., Corson, D. W., Fein, A., and Berridge, M. J. (1986). Excitation and adaptation of *Limulus* ventral photoreceptors by inositol 1,4,5 triphosphate result from a rise in intracellular calcium. *J. Gen. Physiol.*, 88(1):127–42.
- [Radermacher et al., 1994] Radermacher, M., Rao, V., Grassucci, R., Frank, J., Timerman, A. P., Fleischer, S., and Wagenknecht, T. (1994). Cryo-electron microscopy and three-dimensional reconstruction of the calcium release channel/ryanodine receptor from skeletal muscle. *J Cell Biol*, 127(2):411–23.
- [Rengifo et al., 2002] Rengifo, J., Rosales, R., González, A., Cheng, H., Stern, M. D., and Ríos, E. (2002). Intracellular Ca^{2+} release as irreversible Markov process. *Biophys. J.*, 83(5):2511–21.
- [Rice et al., 1999] Rice, J. J., Jafri, M. S., and Winslow, R. L. (1999). Modeling gain and gradedness of Ca^{2+} release in the functional unit of the cardiac diadic space. *Biophys. J.*, 77(4):1871–84.

- [Ríos and Stern, 1997] Ríos, E. and Stern, M. D. (1997). Calcium in close quarters: microdomain feedback in excitation-contraction coupling and other cell biological phenomena. *Annual review of biophysics and biomolecular structure*, 26:47–82.
- [Sala and Hernández-Cruz, 1990] Sala, F. and Hernández-Cruz, A. (1990). Calcium diffusion modeling in a spherical neuron. Relevance of buffering properties. *Biophys. J.*, 57(2):313–24.
- [Saris and Carafoli, 2005] Saris, N.-E. L. and Carafoli, E. (2005). A historical review of cellular calcium handling, with emphasis on mitochondria. *Biochemistry Mosc*, 70(2):187–94.
- [Schiefer et al., 1995] Schiefer, A., Meissner, G., and Isenberg, G. (1995). Ca^{2+} activation and Ca^{2+} inactivation of canine reconstituted cardiac sarcoplasmic reticulum Ca^{2+} -release channels. *J. Physiol. (Lond.)*, 489 (Pt 2):337–48.
- [Serysheva, 2005] Serysheva, I. I. (2005). Structural insights into excitation-contraction coupling by electron cryomicroscopy. *Biochemistry Mosc*, 69(11):1226–32.
- [Sham et al., 1998] Sham, J. S., Song, L. S., Chen, Y., Deng, L. H., Stern, M. D., Lakatta, E. G., and Cheng, H. (1998). Termination of Ca^{2+} release by a local inactivation of ryanodine receptors in cardiac myocytes. *Proc. Natl. Acad. Sci. U.S.A.*, 95(25):15096–101.
- [Sharp et al., 1993] Sharp, A. H., McPherson, P. S., Dawson, T. M., Aoki, C., Campbell, K. P., and Snyder, S. H. (1993). Differential immunohistochemical localization of inositol 1,4,5-trisphosphate- and ryanodine-sensitive Ca^{2+} release channels in rat brain. *J. Neurosci.*, 13(7):3051–63.

- [Shuai and Jung, 2002a] Shuai, J. W. and Jung, P. (2002a). Optimal intracellular calcium signaling. *Phys Rev Lett*, 88(6):068102.
- [Shuai and Jung, 2002b] Shuai, J.-W. and Jung, P. (2002b). Stochastic properties of Ca^{2+} release of inositol 1,4,5-trisphosphate receptor clusters. *Biophys. J.*, 83(1):87–97.
- [Sitsapesan and Williams, 1994] Sitsapesan, R. and Williams, A. J. (1994). Gating of the native and purified cardiac SR Ca^{2+} -release channel with monovalent cations as permeant species. *Biophys. J.*, 67(4):1484–94.
- [Smith, 2002] Smith, G. (2002). Modeling the stochastic gating of ion channels. In Fall, C., Marland, E., Wagner, J., and Tyson, J., editors, *Computational Cell Biology*, pages 291–325. Springer-Verlag.
- [Smith, 1996] Smith, G. D. (1996). Analytical steady-state solution to the rapid buffering approximation near an open Ca^{2+} channel. *Biophys. J.*, 71(6):3064–72.
- [Smith et al., 2001] Smith, G. D., Dai, L., Mura, R. M., and Sherman, A. (2001). Asymptotic analysis of buffered calcium diffusion near a point source. *Journal of Applied Mathematics*, 61(5):1816–1838.
- [Sneyd et al., 2004] Sneyd, J., Falcke, M., Dufour, J.-F., and Fox, C. (2004). A comparison of three models of the inositol trisphosphate receptor. *Prog Biophys Mol Biol*, 85(2-3):121–40.
- [Sobie et al., 2002] Sobie, E. A., Dilly, K. W., dos Santos Cruz, J., Lederer, W. J., and Jafri, M. S. (2002). Termination of cardiac Ca^{2+} sparks: an investigative mathematical model of calcium-induced calcium release. *Biophys. J.*, 83(1):59–78.

- [Soeller and Cannell, 2002] Soeller, C. and Cannell, M. B. (2002). Estimation of the sarcoplasmic reticulum Ca^{2+} release flux underlying Ca^{2+} sparks. *Biophys. J.*, 82(5):2396–414.
- [Stern, 1992a] Stern, M. D. (1992a). Buffering of calcium in the vicinity of a channel pore. *Cell Calcium*, 13(3):183–92.
- [Stern, 1992b] Stern, M. D. (1992b). Theory of excitation-contraction coupling in cardiac muscle. *Biophys. J.*, 63(2):497–517.
- [Stern and Cheng, 2004] Stern, M. D. and Cheng, H. (2004). Putting out the fire: what terminates calcium-induced calcium release in cardiac muscle? *Cell Calcium*, 35(6):591–601.
- [Stern et al., 1997] Stern, M. D., Pizarro, G., and Ríos, E. (1997). Local control model of excitation-contraction coupling in skeletal muscle. *J. Gen. Physiol.*, 110(4):415–40.
- [Stern et al., 1999] Stern, M. D., Song, L. S., Cheng, H., Sham, J. S., Yang, H. T., Boheler, K. R., and Ríos, E. (1999). Local control models of cardiac excitation-contraction coupling. A possible role for allosteric interactions between ryanodine receptors. *J. Gen. Physiol.*, 113(3):469–89.
- [Stewart, 1994] Stewart, W. (1994). *Introduction to the Numerical Solution of Markov Chains*. Princeton University Press, Princeton.
- [Streb et al., 1983] Streb, H., Irvine, R. F., Berridge, M. J., and Schulz, I. (1983). Release of Ca^{2+} from a nonmitochondrial intracellular store in pancreatic acinar cells by inositol-1,4,5-trisphosphate. *Nature*, 306(5938):67–9.

- [Sun et al., 1998] Sun, X. P., Callamaras, N., Marchant, J. S., and Parker, I. (1998). A continuum of InsP₃-mediated elementary Ca²⁺ signalling events in *Xenopus* oocytes. *J. Physiol. (Lond.)*, 509 (Pt 1):67–80.
- [Swillens et al., 1998] Swillens, S., Champeil, P., Combettes, L., and Dupont, G. (1998). Stochastic simulation of a single inositol 1,4,5-trisphosphate-sensitive Ca²⁺ channel reveals repetitive openings during 'blip-like' Ca²⁺ transients. *Cell Calcium*, 23(5):291–302.
- [Swillens et al., 1999] Swillens, S., Dupont, G., Combettes, L., and Champeil, P. (1999). From calcium blips to calcium puffs: theoretical analysis of the requirements for interchannel communication. *Proc. Natl. Acad. Sci. U.S.A.*, 96(24):13750–5.
- [Timerman et al., 1993] Timerman, A. P., Ogunbumni, E., Freund, E., Wiederrecht, G., Marks, A. R., and Fleischer, S. (1993). The calcium release channel of sarcoplasmic reticulum is modulated by FK-506-binding protein. Dissociation and reconstitution of FKBP-12 to the calcium release channel of skeletal muscle sarcoplasmic reticulum. *J. Biol. Chem.*, 268(31):22992–9.
- [Tsien, 1980] Tsien, R. Y. (1980). New calcium indicators and buffers with high selectivity against magnesium and protons: design, synthesis, and properties of prototype structures. *Biochemistry*, 19(11):2396–404.
- [Van Acker et al., 2004] Van Acker, K., Bultynck, G., Rossi, D., Sorrentino, V., Boens, N., Missiaen, L., Smedt, H. D., Parys, J. B., and Callewaert, G. (2004). The 12 kDa FK506-binding protein, FKBP12, modulates the Ca²⁺-flux properties of the type-3 ryanodine receptor. *J Cell Sci*, 117(Pt 7):1129–37.

- [Vélez et al., 1997] Vélez, P., Györke, S., Escobar, A. L., Vergara, J., and Fill, M. (1997). Adaptation of single cardiac ryanodine receptor channels. *Biophys. J.*, 72(2 Pt 1):691–7.
- [Wagner and Keizer, 1994] Wagner, J. and Keizer, J. (1994). Effects of rapid buffers on Ca^{2+} diffusion and Ca^{2+} oscillations. *Biophys. J.*, 67(1):447–56.
- [Wang et al., 2002] Wang, S.-Q., Song, L.-S., Xu, L., Meissner, G., Lakatta, E. G., Ríos, E., Stern, M. D., and Cheng, H. (2002). Thermodynamically irreversible gating of ryanodine receptors in situ revealed by stereotyped duration of release in Ca^{2+} sparks. *Biophys. J.*, 83(1):242–51.
- [Wang et al., 2004] Wang, S.-Q., Stern, M. D., Ríos, E., and Cheng, H. (2004). The quantal nature of Ca^{2+} sparks and in situ operation of the ryanodine receptor array in cardiac cells. *Proc. Natl. Acad. Sci. U.S.A.*, 101(11):3979–84.
- [Wang et al., 2003] Wang, Y.-X., Zheng, Y.-M., Mei, Q.-B., Wang, Q.-S., Collier, M. L., Fleischer, S., Xin, H.-B., and Kotlikoff, M. I. (2003). FKBP12.6 and cADPR regulation of Ca^{2+} release in smooth muscle cells. *Am. J. Physiol., Cell Physiol.*, 286(3):C538–46.
- [Watras et al., 1991] Watras, J., Bezprozvanny, I., and Ehrlich, B. E. (1991). Inositol 1,4,5-trisphosphate-gated channels in cerebellum: presence of multiple conductance states. *J. Neurosci.*, 11(10):3239–45.
- [Wehrens et al., 2003] Wehrens, X. H. T., Lehnart, S. E., Huang, F., Vest, J. A., Reiken, S. R., Mohler, P. J., Sun, J., Guatimosim, S., Song, L. S., Rosemblyt, N., D’Armiento, J. M., Napolitano, C., Memmi, M., Priori, S. G., Lederer, W. J., and Marks, A. R. (2003). FKBP12.6 deficiency and defective calcium release channel

- (ryanodine receptor) function linked to exercise-induced sudden cardiac death. *Cell*, 113(7):829–40.
- [Wehrens et al., 2004] Wehrens, X. H. T., Lehnart, S. E., Reiken, S. R., Deng, S.-X., Vest, J. A., Cervantes, D., Coromilas, J., Landry, D. W., and Marks, A. R. (2004). Protection from cardiac arrhythmia through ryanodine receptor-stabilizing protein calstabin2. *Science*, 304(5668):292–6.
- [Williams et al., 1985] Williams, D. A., Fogarty, K. E., Tsien, R. Y., and Fay, F. S. (1985). Calcium gradients in single smooth muscle cells revealed by the digital imaging microscope using Fura-2. *Nature*, 318(6046):558–61.
- [Williams et al., 2007] Williams, G. S. B., Huertas, M. A., Sobie, E. A., Jafri, M. S., and Smith, G. D. (2007). A probability density approach to modeling local control of calcium-induced calcium release in cardiac myocytes. *Biophys. J.*, 92(7):2311–28.
- [Xiao et al., 1997] Xiao, R. P., Valdivia, H. H., Bogdanov, K., Valdivia, C., Lakatta, E. G., and Cheng, H. (1997). The immunophilin FK506-binding protein modulates Ca^{2+} release channel closure in rat heart. *J. Physiol. (Lond.)*, 500 (Pt 2):343–54.
- [Xin et al., 2002] Xin, H.-B., Senbonmatsu, T., Cheng, D.-S., Wang, Y.-X., Copello, J. A., Ji, G.-J., Collier, M. L., Deng, K.-Y., Jeyakumar, L. H., Magnuson, M. A., Inagami, T., Kotlikoff, M. I., and Fleischer, S. (2002). Oestrogen protects FKBP12.6 null mice from cardiac hypertrophy. *Nature*, 416(6878):334–8.
- [Yao et al., 1995] Yao, Y., Choi, J., and Parker, I. (1995). Quantal puffs of intracellular Ca^{2+} evoked by inositol trisphosphate in *Xenopus* oocytes. *J. Physiol. (Lond.)*, 482 (Pt 3):533–53.

- [Yin et al., 2005a] Yin, C.-C., Blayney, L. M., and Lai, F. A. (2005a). Physical coupling between ryanodine receptor-calcium release channels. *J Mol Biol*, 349(3):538–46.
- [Yin et al., 2005b] Yin, C.-C., Han, H., Wei, R., and Lai, F. A. (2005b). Two-dimensional crystallization of the ryanodine receptor Ca^{2+} release channel on lipid membranes. *J Struct Biol*, 149(2):219–24.
- [Yoshihara et al., 2005] Yoshihara, S., Satoh, H., Saotome, M., Katoh, H., Terada, H., Watanabe, H., and Hayashi, H. (2005). Modification of sarcoplasmic reticulum (SR) Ca^{2+} release by FK506 induces defective excitation-contraction coupling only when SR Ca^{2+} recycling is disturbed. *Can J Physiol Pharmacol*, 83(4):357–66.
- [Yuste et al., 2000] Yuste, R., Majewska, A., and Holthoff, K. (2000). From form to function: calcium compartmentalization in dendritic spines. *Nat Neurosci*, 3(7):653–9.

Vita

Jeffrey Ryan Groff was born February 17, 1979 in Lancaster, Pennsylvania. He graduated from Hempfield High School in June of 1997. In the fall of 1997 he began classes at McDaniel College (f. Western Maryland College) where he received a Bachelor of Arts in Physics in May 2001. From January until September 2002, he was a laboratory technician at Wyeth Pharmaceuticals in Marietta, Pennsylvania, employed in the production of influenza virus vaccine. He began graduate studies of computational biology in The Department of Applied Science at The College of William & Mary in January 2003. He received his Master of Science in Applied Science in January 2005 and continued his studies of computational biology in pursuit of a Doctorate of Philosophy.